Integer and fractional Chern insulators in two-dimensional van der Waals heterostructures

Jiaqi Cai

A dissertation
submitted in partial fulfillment of the
requirements for the degree of

Doctor of Philosophy

University of Washington

2024

Reading Committee:

Xiaodong Xu, Chair

David Cobden

Di Xiao

Program Authorized to Offer Degree:
Department of Physics

University of Washington

Abstract

Integer and fractional Chern insulators in two-dimensional van der Waals heterostructures

Jiaqi Cai

Chair of the Supervisory Committee:
Xiaodong Xu
Department of Physics

New developments in van der Waals materials and fabrication techniques bring new opportunities for investigating emergent quantum phases of matter in two dimensions. Chern insulator is a notable example, characterized by the Chern number C. The Chern insulator is remarked as the lattice version of quantum Hall effect, and has vanishing longitudinal resistance and quantized Hall resistance of h/Ce^2, where h is the Planck constant and e is the electron charge. This thesis investigates novel Chern insulators enriched by magnetism, pseudospin degrees of freedom, and translational symmetry. The discovery is enabled by new materials that incorporate intrinsic magnetism into topological insulators, or new control knobs such as the twist angle between layers that can lead to strong interaction and spontaneous magnetism. The interplay between topology and the above ingredients deepens our understanding of the topological phase of matter and also seeks device applications. Another family of novel Chern insulators, the fractional Chern insulator, is a strongly correlated phase that has fractionally charged excitations, anyons. It is characterized by a non-integer rational many-body Chern number ($C \in \mathbf{Q}/\mathbf{Z}$). This lattice analogy of fractional quantum Hall states can exist at elevated temperatures and in zero magnetic field and could facilitate anyonic research into a more experimentally accessible regime. This state of matter, and the associated fractional quantum anomalous Hall effect, is discovered in the twisted molybdenum ditelluride ($MoTe_2$) moiré superlattice and will be another central topic of this thesis.

TABLE OF CONTENTS

LIST OF FIGURES

ACKNOWLEDGMENTS

Firstly, I extend my deepest gratitude to my advisor, Xiaodong Xu, for navigating me through the jungle of science over the past five years. Xiaodong's passion, optimism, patience, creativity, and commitment to scientific rigor have been significant in my growth. One notable quality I appreciated is the pursuit of efficiency, from optimizing experimental tests to employing concise yet precise language in our publications. During my graduate school search, we had a ten-minutes Skype call and the moment he heard I had a band structure calculation for twisted double bilayer graphene, that was the night we started to collaborate. His sharp scientific insight and ability to discern the most viable research paths have been a constant source of inspiration, driving us toward scientific achievements.

I also wish to express my appreciation to David Cobden, Jiun-Haw Chu, and Matthew Yankowitz, in particular for their trust in me as a collaborator and for allowing me the privilege to lead efforts with many shared equipments. Their contributions have helped build one of the most collaborative environments for condensed matter experiment, where all lab members support each other and thrive on shared ideas and innovative solutions. I learnt a lot from them.

My thanks also go to Di Xiao, Ting Cao, and Wang Yao for their theoretical support, which has been a cornerstone of confidence in my work. Discussing my experiments with them has always been enriching, thanks to their sharp insights into the physics underlying our data. Their group members, Chong Wang, Xiaowei Zhang, Xiaoyu Liu (UW), and Huiyuan Zheng (HKU) have been very helpful and worked out details with me.

I am particularly grateful for the collaboration with Cuizu Chang and his lab members, whose expertise in the quantum anomalous Hall effect has been invaluable. My projects could not have been realized without the high-quality crystals provided by Dr. Kenji Watanabe, Dr. Takashi Taniguchi, and Dr. Jiaqiang Yan. Their contributions have been crucial

to the success of my research.

I am lucky to work in a supportive lab. Upon joining the lab, Zaiyao Fei, Zhong Lin, Dmitry Ovchinnikov, and I quickly became a cohesive team on projects focusing on $MnBi_2Te_4$. They have been invaluable mentors, equipping me with essential experimental skills. I am grateful to Xi Wang and Yingqi Wang for their inspirational experimental prowess. Learning from Nathan Wilson has deepened my understanding of instrumentation, while interactions with Bevin Huang, Kyle Hwangbo, John Cenker, and Geoffrey Diederich have broadened my knowledge in optics. Tiancheng Song and Minhao He deserve special mention for their unwavering support in both my personal and professional life. Tiancheng told me how to acquire high-quality data by keeping improving setups. Minhao has made the best graphene devices I have ever seen, and I am lucky to be shared with numerous tricks for fabrication. Notably, many previous member found their own paths in academia or industry, but we are continuing to support each others.

I must acknowledge Eric Anderson, Jordan Fonseca, Jiayi Zhu, Yinong Zhang, Heonjoon Park, William Holtzmann, Courtney Baier, Jack Barlow, Mai Nguyen, Sinabu Pumulo, Dhan Bautista, Essance Ray, Julian Stewart, Yuzhou Zhao, Chaowei Hu, Jiang Yao, and Weijie Li. My journey would not have been possible without them. Special thanks to Eric and Heonjoon for the countless late nights we spent working together. Will's expertise in optics and instrumentation has been particularly astounding. Together, these individuals have made Xu lab not just a place for scientific endeavor but a vibrant community and a second home.

UW condensed matter community is vibrant, collaborative and friendly. I thank Wenjin Zhao, Paul Nguyen, Arnab Manna, Elliott Runburg, Eric Lester and Luca Delgado in Cobden lab, Zhaoyu Liu, Qianni Jiang, Paul Malinowski, Yue Shi, Elliott Rosenberg, Jonathan DeStefano in Chu lab, Xuetao Ma, Dacen Water, Chun-Chih Tseng, Ellis Thompson, Zhiming Zhang, Florie Mesple, Manish Kumar in Yankowitz lab, and Laurel Anderson and Chadwick Evans in Barnard lab. Zhaoyu Liu and Chaowei Hu deserved special thanks for their steady hand and saving my samples with magic silver paste.

I would like to express my gratitude to those who provided invaluable discussions on experimental techniques and theoretical or phenomenological understanding, which greatly assisted me in getting started. My sincere thanks go to Pengjie Wang (UIUC) for his expertise in setting up the dilution fridge and David Graf (NHMFL) for his host in national high magnetic field lab and impressive silver paste. I am also grateful to Paul Malinowski and Eric Anderson for hosting the UW condensed matter journal club (now the TIQM journal club) and to the participants of my own journal club. Additionally, I appreciate the inspiring discussions and friendships with Yinghai Wu (HUST) on FQH physics and the Jain sequence, Gaopei Pan (Würzburg) on QMC simulations, Qicheng Tang (Georgia Tech) on CFT understanding, Qihao Guo (Purdue) on microwaves, Junkai Dong (Harvard) on CFL, Jixiang Yang (MIT) on THz, and Tonghang Han (MIT) on pentalayer graphene. I am also thankful to many others who have supported and inspired me throughout this journey.

Lastly, words cannot express my gradtitude to my wife, Jingxi and other family members, for their love and support during challenging times and as a source of joy in moments of triumph.

DEDICATION

To my family

Chapter 1

INTRODUCTION

1.1 Integer quantum Hall effect and topology

The discovery of the quantum Hall effect (QHE) has opened a new avenue in condensed matter physics, known as topological condensed matter physics. Before the observation of QHE, the cornerstone of condensed matter physics was the Landau symmetry-breaking paradigm. Landau [1] developed a theory that uses an order parameter to model different phases. Ginzburg and Landau [2] found that symmetry could distinguish different phases in a second-order phase transition, with the order parameter being the tensor field invariant under these symmetry group elements. Nambu and Goldstone[3, 4] discovered that gapless excitations—photon-like low-energy modes such as phonons and magnons—are the conjugate fields that attempt to recover the broken symmetry. This symmetry-breaking machinery was completed by another milestone: the application of the renormalization group in condensed matter systems by Fisher, Wilson, and others[5, 6].

The symmetry-breaking paradigm has been very successful in explaining various condensed matter phenomena, such as the transition from gas to liquid/solid[7], magnetism[8], superfluidity[9], aspects of superconductivity[2], and the Kondo problem[5, 6]. It is, therefore, not difficult to understand why the QHE was such a surprise, given the success of Landau theories that, however, fail to elucidate the QHE.

Integer QHE was observed in a two dimensional electron gas under low temperature and strong magnetic field by Klaus von Klitzing (1980, [10]). Here, the longitudinal resistance R_{xx} is vanishingly small, and the Hall resistance R_{xy} remains exact quantized.

$$R_{xx} \simeq 0, R_{xy} = \frac{h}{e^2 \nu} \tag{1.1}$$

where h is the Planck constant, e is the electron charge, and $\nu \in \mathrm{Z}$ is an integer. This phenomenally resembles a perfect conductor, with the ballistic electron channel on one side

of the sample. Converting from resistance to conductance, we have:

$$\sigma_{xx} \simeq 0, \sigma_{xy} = \nu \frac{e^2}{h} \tag{1.2}$$

This state is found to be gapped, and follow thermal activation behavior of small-gap system, the Arrhenius equation $\sigma_{xx} \simeq \sigma_0 e^{-\frac{\Delta}{2k_B T}}$ where Δ is the thermal activation gap, k_B is the Boltzman constant and T is the temperature. In the limit of $\sigma_{xy} \gg \sigma_{xx}$ we have $\rho_x x \simeq \frac{\sigma_{xx}}{\sigma_{xy}^2} = R_0 e^{-\frac{\Delta}{2k_B T}}$ and $= R_{xy} \simeq 1/\sigma_{xy} - \frac{\sigma_{xx}^2}{\sigma_{xy}^4}$ for resistivity. This conductance tensor suggests a perfect insulator. To reconcile these observations, the simplest explanation is the presence of dissipationless edge conducting channels, while the bulk of the two-dimensional materials remains insulating. However, the emergence of such edge gapless modes remains a mystery within the framework of Landau symmetry breaking. In standard Landau symmetry breaking setup, an infinitely large or thermodynamic-limit system was considered to only be characterized by order parameter. However, in quantum Hall effect, the appearance of edge modes does not accommodate such a usual description.

What quantity characterizes integer QHE? Apparently, the observable, Hall conductance σ_{xy} in finite size geometry, can distinguish different quantum Hall states. Thouless *et al*[11]. proposed that such a phenomenon can be general in a solid state system setting without considering the details of the band. By using Kubo formula, they prove that in a gapped system, the Hall conductance is (**TKNN formula**):

$$\sigma_{xy} = \frac{ie^2}{h} \sum_n \int d^2k \left[\left(\frac{\partial u_{nk}}{\partial k_x} \frac{\partial u_{nk}}{\partial k_y} - \frac{\partial u_{nk}}{\partial k_y} \frac{\partial u_{nk}}{\partial k_x} \right) \right] \tag{1.3}$$

where u_{nk} is the nth Bloch wave function, and $k = (k_x, k_y)$ is the Bloch electron's wavevectors. It is a surprise and beyond Landau symmetry breaking that this formula, that relates to the wave function rather than any symmetry, gives an integer. It was quickly realized that this TKNN formula is the first realization of well-known topological Chern invariant[12]. In a more modern way of expression[13], this Chern number is:

$$\sigma_{xy} = \frac{e^2}{h} \times C, \qquad C = \int \mathcal{B} \tag{1.4}$$

where $\mathcal{B}$ is a curvature 2-form defined in an appropriate defined single particle Hilbert space.

Info 1.1: Geometry in quantum mechanics

To understand topology in quantum mechanics, the first thing is to understand geometry. Considering a parameter space denoted by $\vec{s}$ and a Hamiltonian defined as a function of $\vec{s}$. For condensed matter, we can also consider for example Bloch wave vector $\vec{s}_i = k_i \mod \pi$ and standard Bloch Hamiltonian $H(k)$. The distance of two wavefunction is:

$$\|\psi(s+ds)-\psi(s)\|^2 = \langle \psi(s+ds)-\psi(s) \mid \psi(s+ds)-\psi(s)\rangle = \langle \partial_i\psi \mid \partial_j\psi\rangle\, ds_i ds_j + O\left(ds^2\right) \quad (1.5)$$

We can define $\langle \partial_i\psi \mid \partial_j\psi\rangle \equiv K_{i,j}$ where $\partial_i \equiv \frac{\partial}{\partial s_i}$. Now, the imaginary part and real part of K give:

$$K_{i,j} = \gamma_{i,j} + i\mathcal{B}_{i,j}, \quad \gamma_{i,j} = \gamma_{j,i}, \quad \mathcal{B}_{i,j} = -\mathcal{B}_{j,i} \quad (1.6)$$

Apparently, $\mathcal{B} = \mathcal{B}_{i,j} ds_i \wedge ds_j$ is a closed 2-form because i) $d\mathcal{B} = 0$, and ii) There exists an 1-form $\beta = \beta_j ds_j$ and $\beta_j = -i\langle \psi(s) \mid \partial_j\psi(s)\rangle$ so that $\mathcal{B} = d\beta$. Additionally, for a natural gauge transformation, $\psi \to e^{i\alpha(s)}\psi$, we have $\beta \to \beta + d\alpha$ and thus $\mathcal{B} = d\beta \to \mathcal{B}$ is invariant. This observable two-form is called **Berry curvature** [13, 14].

For the $\gamma_{i,j}$ part, one can verify it is not gauge invariant. However, a slightly modified quantity $g_{i,j} = \gamma_{i,j} - \beta_i\beta_j$ is indeed gauge-invariant. This quantity is called Fubini-Study metric, which has deep connection to localization (σ_{xx}) [15, 16, 17, 18] and superfluid weight[19, 20].

Berry curvature can give the definition of Chern number as shown above, by simply contracting parameter the and the metric can give **Euler character** through standard Riemannian machinery[21]. We will repeatedly see the Chern number is very useful in condensed matter system.

It is interesting to think about the measurability of Chern number and Fubini-Study metric[22], i.e., physical geometric quantities. A tight binding model to describe ideal non-interacting condensed matter system is host by lattice with on-site Wannier orbital $|r_i\rangle$, hopping amplitude $\{t_i\}$ (from i-site to others), on-site potential $\{V_i\}$ that are both periodic Z_n, and has some internal degree of freedom described by a Lie group G. Bloch theorem maps a n-dimensional system to a zero dimensional system with an additional Riemannian structure. However, there are different choices of this Riemannian structure. For example, one can show that redefinition of real space basis $|r_i\rangle$, which won't affect the spectrum, does affect the reciprocal space Berry curvature but does not affect Chern number of a gapped phase. In this sense, Fubini-Study metric is not an observable in this specific setup. Chern number is always

an observable. The measurability of geometry quantity in a real condensed matter system with probes, coupling to bosonic field, and disorder is an interesting direction to explore in theory. The measurability of geometric quantities is also of interest in relativistic systems, e.g., those described by non-Abelian gauge theories[23]. It is interesting to understand the related conclusions from lattice gauge theory for condensed matter physicists[23].

In 1988, Haldane [24] elucidated a profound connection between the emergence of dissipationless edge modes in QHE, and the parity anomaly observed in quantum electrodynamics[25] and quantum chromodynamics[26, 27]. He proposed a lattice model with spinless fermions arranged in a honeycomb lattice featuring nearest neighbor hopping and complex next-nearest neighbor hopping—this is known as the **Haldane model**[24]. The Haldane model breaks time-reversal symmetry (due to the condition of spinless fermions) but uniquely does so without any Peierls phase in the lattice, thereby in the absence of a magnetic field. Consequently, the quantum anomalous Hall effect (QAHE) can be realized if such a realization of the Haldane model is achievable. This model affirms that topology is central to understanding QHE, demonstrating that QHE can occur in a general setting of band electrons in solid states. The class of lattice models with a topological band gap characterized by the Chern number is also referred to as a **Chern insulator**.

Although the Haldane model advanced the theoretical understanding of the QHE, its experimental realization remained elusive for over two decades. A breakthrough came with further developments in topological band theory, notably through the three-dimensional topological insulator (3DTI)[28, 29] modelled by the (3D) Bernevig-Hughes-Zhang (BHZ) model[30, 31]. In contrast to the Haldane model, the BHZ model facilitates surface states with Dirac fermions protected by time-reversal symmetry. Ultimately, QAHE was experimentally realized by magnetically doping a 3DTI epitaxy-grown thin film. For a comprehensive history of the realization of QAHE, an overview is provided in Ref. [32, 33].

1.2 Fractional quantum Hall effect and anyon

Not long after the discovery of the integer Quantum Hall Effect (QHE), additional surprising plateaus at fractional fillings—known as the fractional QHE (FQHE)—were observed by

Tsui et al.[34]. Compared to the integer QHE, for FQHE we have:

$$R_{xx} \simeq 0, \qquad R_{xy} = \frac{h}{e^2\nu}, \qquad \nu \in \mathrm{Q}\backslash\mathrm{Z} \tag{1.7}$$

Given that the Chern number is an integer for an electron's band, it appears that the existing topological band theory cannot explain FQHE. It turns out, the Coulomb interaction within a Landau level with quenched kinetic energy is key to FQHE. This interaction lifts the degeneracy in Landau levels and opens many-body gaps. Despite the apparent simplicity of its many-particle Hamiltonian, FQHE is theoretically challenging to study:

$$H = \sum_{m<n} \frac{1}{|\mathbf{r}_m - \mathbf{r}_n|} \tag{1.8}$$

where the Hilbert space is projected into the lowest Landau level, and ϵ is the dielectric constant. The theoretical challenge arises from the massive degeneracy of the lowest Landau level: for the: for the $\nu = 1/3$ filling and 10^8 electron problem, the degeneracy is $\binom{3\times10^8}{10^8} > 10^{10^7}$.

Laughlin developed a general gauge argument for the integer QHE [35] and quickly extended this argument to the FQHE [36], recognizing that it necessitated the existence of fractionally charged excitations. This idea, originally proposed by Leinaas,Myrheim and developed by Wilczek [37, 38] in a different context, suggests the existence such fractionally charged excitations. Given the robustness of gauge arguments in the theoretical understanding of quantum systems[39, 40], anyons are an inevitable consequence[41]. Laughlin then proposed an ansatz for the FQH state, known as the Laughlin wavefunction. The original wavefunction in particular explains the states for $\nu = 1/q$, where q is an odd number, such as $1/3$ with $e/3$-charged anyons. Haldane and Halperin have developed a theory of hierarchy states for $\nu = p/q$ that new filling states can be constructed from quasiparticle condensation in its own Laughlin groundstate[41, 42].

Info 1.2: Orders in FQHE

As a side note to connect to Landau paradigm, I want to explain why FQHE is considered as an ordered state. In Landau paradigm, there are two obvious phenomenological classes of symmetry breaking phases. One type includes crystal order, charge density waves, and ferromagnetism. The hallmark of this type of phase transition is density modulation, which can lead to observable order parameter such as density modulation $\delta\rho$ for crystal order or magnetization M for magnetism. The other includes superfluid, Bose-Einstein condensate, and superconductivity (without considering charge part), whose hallmarks are phase coherence and observable Josephson effect. Sometimes two order can coexist and there is no strict distinct between them in this case.

Yang discovered the mathematical description of such classification, the notion of off-diagonal long-range order (ODLRO). The phase coherence is characterized by a nonzero value of the off-diagonal terms of the real-space density matrix $\rho(r, r') = \langle\psi^*(r)\psi(r')\rangle$ in the long-distance limit: $\lim_{|r-r'|\to\infty} \rho(r, r') \neq 0$.

At first glance, FQHE has no such long-range order. We can consider Laughlin's wave function at filling number $\nu = 1/m$, $\psi(z_1, ..., z_n) = \Pi_{j<k}(z_j - z_k)^m e^{-\frac{1}{4}\Sigma_l |z_l|^2}$. We have the single-particle density matrix $\rho_{z,z'} \simeq e^{-1/4(z-z')^2/l_B}$ that decays exponentially, where $l_B = \sqrt{\frac{\hbar c}{eB}}$ is the magnetic length. However, Girvin and MacDonald found that the composite boson with m fluxes attached to a single electron indeed has ODLRO. We can consider a singular gauge field for Peierls substitution, $\psi_{cb} = \exp\{[-im\Sigma_{i<j} \operatorname{Im}\ln(z_i - z_j)]\} \times \psi$, and obtain a single-particle density matrix of the form: $\tilde{\rho}_{z,z'} \simeq |z - z'|^{-2\nu}$, which has an algebraic decay that signals quasi-ODLRO of the composite boson in this picture. In such a picture, we can construct a Landau-Ginzburg-Chern-Simons theory with broken symmetry and a nonlocal order parameter to capture many aspects of FQH [43, 44].

The hidden ODLRO in the composite boson, as well as the need for a nonlocal order parameter to describe FQHE, suggests that the order of FQHE is different from Landau orders. We now know that FQHE has rich contents, especially characterized by topological orders. For more in this direction, see [45, 46, 47].

Surprisingly, experiments [48, 49, 50, 51, 52] also observed FQHE at even denominators for $\nu = p/q$, such as the $\nu = 5/2$ state or the $\nu = 1/2$ state in wide GaAs quantum wells. The theoretical understanding of these additional fillings led to the establishment of non-Abelian

anyons as quasiparticle excitations for certain states, such as the Moore-Read Pfaffian and Read-Rezayi parafermion states.

Recently, the statistical phase of Abelian anyons has been observed in interferometry measurements [53, 54]. The wavefunction of non-Abelian anyons has also been simulated by quantum simulation experiments in superconducting circuits or trapped ions [55, 56].

Despite the success of using the concept of anyons to understand FQHE, a new platform that offers more experimental tunability and robustness is urgently needed. Theorists have proposed another paradigm—high-temperature FQHE at zero magnetic field without Landau level formation, i.e., the fractional quantum anomalous Hall effect (FQAHE) [57, 58, 59, 60, 61, 62]. This effect relies on partially filling a topologically nontrivial Chern band with interacting electrons. The new phase of matter hosting the FQAHE, coined the fractional Chern insulator (FCI), was firmly established as a concept around 2011 by several theoretical groups. Although the initial theoretical work did not consider specific material systems [57, 58, 59, 60, 61], they pointed out the key element necessary for the experimental realization of FCI—engineering a flat Chern band. There have since been extensive proposals of candidate materials [62]. The search and observation of FCIs are another central topic of this thesis.

Info 1.3: Braid group and anyons

The FQHE brings the fractionalized quasiparticle, anyon, into active research. In three dimensions and higher, there are only two classes of elementary particles, fermions and bosons. They are characterized by exchange statistics $\psi(\mathbf{r}_1, \mathbf{r}_2) = e^{i\theta}\psi(\mathbf{r}_2, \mathbf{r}_1)$, with $\theta = 0$ for bosons and $\theta = \pi$ for fermions. Mathematically, the classification group of exchange statistics is the fundamental group of two-particle configuration space [38, 63] $\mathcal{A}_2^d = (\mathrm{R}^{d\cdot 2} - (0,0))/S_2$, where R^d is the space for Cartesian coordinates in d-dimensions, the quotient of $(0,0)$ reflects considering only nontrivial space $\mathbf{r}_1 \neq \mathbf{r}_2$, and S_2 reflects that the observables for two identical particle wavefunctions are invariant for $\mathbf{r}_1 \Leftrightarrow \mathbf{r}_2$. We have:

$$\pi_1\left(A_2^d\right) = \begin{cases} S_2 & \text{for } d \geq 3 \\ B_2, & \text{for } d = 2 \end{cases} \tag{1.9}$$

where S_2 for $d \geq 3$ represents that only bosons and fermions can exist in three dimensions and higher, as seen by the trivial one-dimensional representation $+, -$. For higher dimensions, it can also be proved that the representation can be treated as a statistical part that only has fermionic and bosonic statistics with a spin part with non-Abelian spin group representation. The braid group B_2 has one-dimensional Abelian representations, corresponding to Abelian anyons with arbitrary θ. More interesting cases are the non-Abelian representations of B_2, which are non-Abelian anyons. These have a multifold-degenerate ground state Hilbert space that can be harnessed for fault-tolerant quantum computation.

1.3 Van der Waals two-dimensional materials

QHE was initially discovered in semiconductor quantum well systems where semiconductors with different bandgaps and carrier densities were interfaced to produce a sharp potential trap that confines electrons into a two-dimensional plane. These embedded two-dimensional electron gases (2DEGs) were one of the main stages for investigating fascinating electronic properties and device physics.

An alternative way to trap electrons is to use layered compounds and, ideally, monolayers of atomic materials. This group of materials, two-dimensional (2D) materials such as graphene, was isolated by Geim and Novoselov using mechanical exfoliation [64, 65].

Graphene, as the first monolayer 2D material, has a simple band structure in long wavelengths: two-dimensional Dirac fermions with spin and valley degrees of freedom [65, 66]. This special degeneracy, together with the nontrivial Berry phase surrounding the Dirac point, gives rise to unusual quantum Hall sequences, such as $\nu = \pm 2, \pm 6, \pm 10, ...$ at low magnetic field Landau level fillings. The $\Delta\nu = 4$ comes from spin and valley degeneracy. At high fields, the magnetic field together with interactions can break the degeneracy [67]. Unconventional FQHE states have also been found in bilayer graphene [50, 51, 52]. To date, graphene is still revising the QHE physics.

Compared to the quantum well system, electrons in 2D materials can be accessed on the surface and tailored with different properties. The trapping potential comes from the atomic lattice, enriching electronic properties. To date, the 2D materials family has grown to cover many fascinating phases, such as superconductors [68], magnets [69, 70], and topological insulators [71, 72]. In Chapter 2, we will encounter an intrinsic magnetic topological insulator, $MnBi_2Te_4$, and investigate how magnetism interplays with its topological nature.

Many opportunities also emerge as these two-dimensional materials with diverse properties can be stacked via so-called dry transfer techniques. A polymer can be used to pick up 2D materials layer by layer, and in between the layers, the interface can be atomically clean and pristine. This can give rise to interface effects and designer new phases. One example is that atomically thin dielectrics, such as hexagonal boron nitride, can be integrated as ultra-clean substrates, and multi-layer graphite can be used as gate electrodes [73, 74]. The reduced disorder in the substrate has greatly advanced mobility and homogeneity.

To show another example, a twist angle between homobilayers made with bilayer of the same 2D material or heterobilayer consist different 2D mateirals with similar lattice constant[75, 76, 77], can lead to moiré pattern that has much longer wavelength $\sim$ 10 nm than the intrinsic atomic lattice $\sim$ few Å. The carrier density of 2D materials can be tuned by electrostatic gating at the order of $\sim 10^{13}$ cm^{-2}, but changing the band filling requires $\sim 10^{16}$ cm^{-2}. The longer moiré pattern will introduce umklapp-like scattering and forms moiré miniband that only require $\sim 10^{12}$ cm^{-2} to change it band filling. The topology and bandwidth are also shown to be twist-angle controllable. These flexibility makes two-dimensional materials a fascinating platform to investigate emerging topological phases.

In Chapter 3, we will investigate how this moiré pattern in multilayer graphene can enrich the Chern insulator phases. In Chapter 4, we will investigate the observation of zero magnetic field fractional Chern insulators that exhibit quantum anomalous Hall effect, thanks to the moiré flat Chern band.

Summary 1: Quantum Hall effect, Chern insulators and anyons

- The observation of QHE has opened a new paradigm to understand condensed matter phases using the concept of topology.
- The observation of FQHE has facilitated the anyon research.
- (F)CIs are zero-field lattice version of (fractional) quantum Hall states.
- Two-dimensional materials are advancing the quantum Hall physics and give new oppotunities due to their unique tunability.

1.4 Outline of the thesis

Chapter 2 is based on series work of intrinsic magnetic topological insulator $MnBi_2Te_4$[78, 79, 80], in which we will reveal how magnetism can interplay with Chern insulator and leads to functional devices.

Chapter 3 is based on a series of works on twisted multilayer moiré superlattices [81, 82, 83]. This is a tunable strongly correlated system with topological bands. We have observed Chern insulators with Chern numbers $\pm 3, \pm 2, \pm 1$ emerging from moiré miniband filling numbers $\nu = \pm 1, \pm 2, \pm 3$. They are spin-valley symmetry breaking Chern insulators, with a magnetic field that breaks time reversal symmetry $\mathcal{T}$ or mirror-time reversal combined symmetry $\mathcal{C}_2\mathcal{T}$. We have also seen translational symmetry breaking Chern insulators at fractional fillings such as one-third or one-half filling of a single band.

Chapter 4 is based on a series of works on twisted $MoTe_2$ moiré superlattices [84, 85, 86]. Compared to the graphene system, transition metal dichalcogenides have strong spin-orbit coupling. This simplifies moiré physics and hosts the seminal Chern insulator model: the

Haldane model. We have observed, for the first time, fractional quantum anomalous Hall effect in this system.

Chapter 2

CHERN INSULATORS IN INTRINSIC MAGNETIC TOPOLOGICAL INSULATOR $MnBi_2Te_4$

An intuitive way to understand a Chern insulator is as the marriage of magnetic order and topology [87]. A Chern insulator can be achieved by introducing magnetism in a thin film topological insulator [88]. Experimentally, this strategy has led to the realization of the quantum anomalous Hall effect in magnetically doped topological insulators (M-doped TI), in which a ferromagnetic order is combined with a topological band [89]. The hallmark of such a phase is the quantized Hall resistance and nearly vanishing longitudinal resistance in the absence of any magnetic field. The ferromagnetic nature of M-doped TI also gives rise to a hysteresis loop and various interplays between magnetic texture [90, 91] and the topology of this system [92].

Another natural realization is a magnetic topological insulator with intrinsic magnetic order. The $MnBi_2Te_4$ and related material family MnBi2nTe3n + 1 emerge as a fascinating system to explore this opportunity [93, 94, 95, 96, 97, 98]. Because of its van der Waals nature, the crystal can be exfoliated down to very thin layers. The atomically thin layer of $MnBi_2Te_4$ has magnetic phases upon applying a magnetic field and becomes gate-tunable. Electrical control and magnetic control will be central to this chapter.

Figure 2.1 show the structure and atomic force microscope characterization of $MnBi_2Te_4$. $MnBi_2Te_4$ is a layered van der Waals compound that consists of Te-Bi-Te-Mn-Te-Bi-Te septuple layers (SL) stacked along the crystallographic c-axis(Fig. 2.1 **a**). At zero magnetic field, it hosts an A-type antiferromagnetic (AFM) ground state: each SL of $MnBi_2Te_4$ individually exhibits ferromagnetism with out-of-plane magnetization, while the adjacent SLs couple anti-ferromagnetically, as shown in Fig. 2.1 **a**. By applying an external magnetic field perpendicular to the SLs, the magnetic state evolves from AFM to canted AFM (cAFM) and then to FM as shown in Fig. 2.1 **b**.

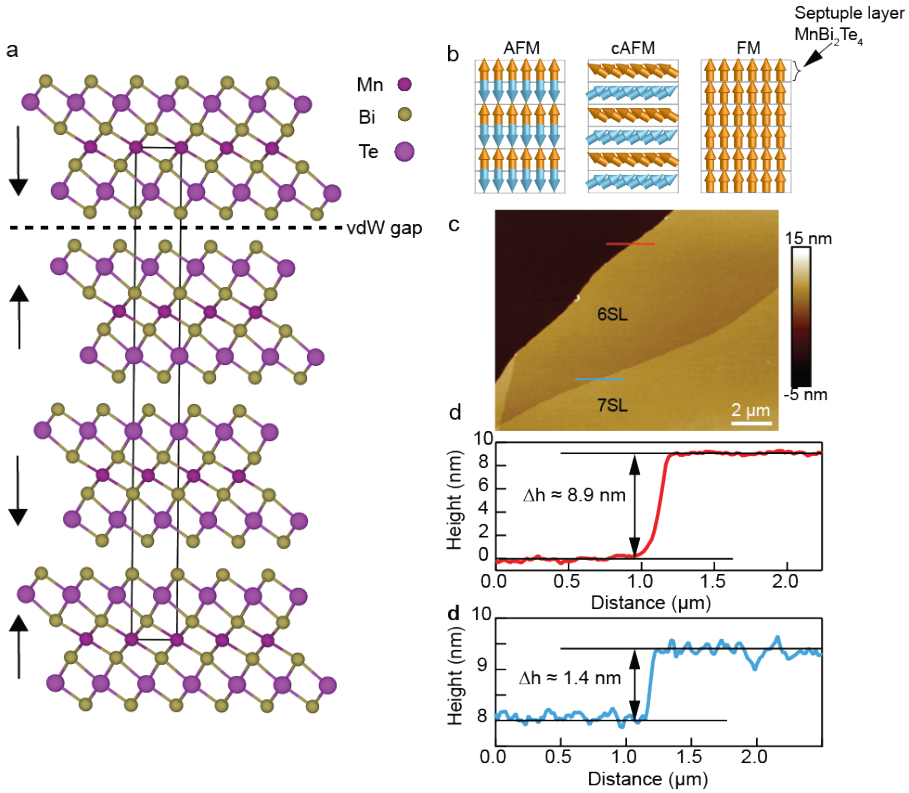

Figure 2.1: Structure and atomic force microscope characterization of $MnBi_2Te_4$ thin film **a**, crystal structure of $MnBi_2Te_4$. **b**, the ground state antiferromagnetic(AFM) layered, finite field canted-AFM (cAFM) and ferromagnetic(FM) spin configuration. **c**, atomic force microscope image of thin film $MnBi_2Te_4$. **d**, thickness of a 6-septuple layer(SL) sample, and the height difference between 6SL and 7SL sample.

Info 2.1: Rationally degisner Chern insulator

1. Magnetic topological insulator(MTI) can be realized by magnetically doping 3D topological insulator thin film. The ferromagnetic will open a gap for surface Dirac cone of 3D topological insulator that has non-zero Chern number. This routine has been successful and demonstrated magnetic topological insulator. An interesting way to improve the homogeneity of MTI is to instead use magnetic proximity effect to induce magnetic order into a topological insulator[87, 89, 88].

2. In theory, Haldane Chern insulator can be realized in honeycomb lattice[24], introduce spin-orbital coupling and ferromagnetic order. Such routine has been tried in various system, e.g., magnetically proximitized graphene[99, 100]. In experiment, the routine is experimentally challenging due to complex interplay among magnetic orders, charge transfer, interface disorder and strain[101, 102, 103].

3. Chern insulator can also be presented in any lattice system. One requirement is that the system needs to be spinless and highly controllable. Early studies have been shown Haldane Chern insulator and chiral dynamics for photonic[104] and phononic[105] artificial crystals. Recently, moiré superlattice also provides such a routine [106, 107], but the ferromagnetic order realizes on spontaneous time-reversal symmetry breaking from electron interaction. Many of them are actually Mott insulators or charge transfer insulators, deviating from the original band insulator picture proposed by Haldane[108].

2.1 Canted anti-ferromagnetic Chern insulator

The Chern insulator state has recently been demonstrated in mechanically exfoliated $MnBi_2Te_4$ devices at both zero (5SL) and high magnetic fields (6-10SL). Here, we demonstrate that functions as a Chern insulator in the cAFM state as shown in Fig. 2.2 and present a method for controlling the edge conduction via an electric field. Our methodology integrates polar reflective magnetic circular dichroism (RMCD) measurements (See Appendix) to ascertain the magnetic states with magneto-transport measurements to investigate the topological properties. To differentiate the effects of electric-field application from those of carrier doping, we constructed devices equipped with dual gates(Fig. 2.2 **a-b**). Devices featuring a single gate were also deployed to perform combined transport and RMCD measurements.

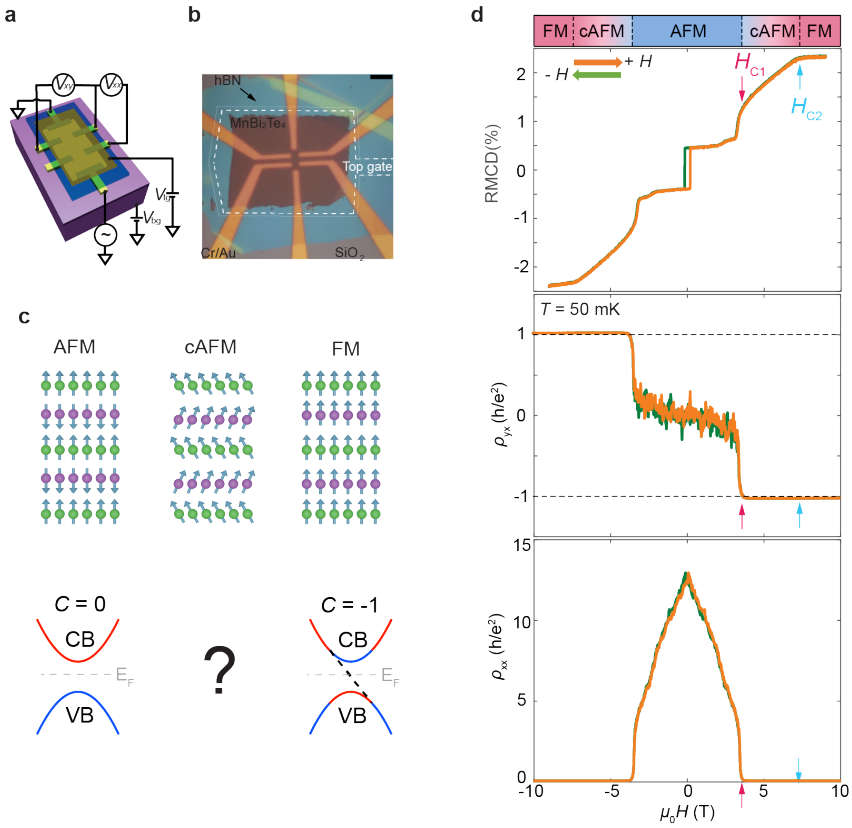

Figure 2.2: Observation of the canted-antiferromagnetic (cAFM) Chern insulator state.**a**, device structure and transport measurement of ρ_{xx} and ρ_{xy}. **b**, device optical image. **c**, magnetic field dependent spin configuration and associated simplified band structure. **d**, top panel, reflective circular dichroism (RMCD) signal taken at a temperature of 2 K at $V_{\mathrm{bg}} = 0V$. Middle panel, ρ_{yx}, and bottom panel, ρ_{xx} measurements as a function of magnetic field ($\mu_0 H$) at optimal gate voltage $V_{\mathrm{bg}} = 53$V. RMCD data are acquired at $T = 2$ K while transport data at $T = 50$ mK. Green and orange traces correspond to magnetic field sweeping down and up, respectively. The red arrow denotes the spin flop field H_{C1} and the light blue arrow indicates the critical field H_{C2} for reaching the field-induced ferromagnetic states. The slight offset of the spin-flop fields between RMCD and transport measurements are due to the different gate voltage and temperature of the measurements. ρ_{yx} is antisymmetrized against $\mu_0 H$ while ρ_{xx} is symmetrized.

Figure 2.2 **d** shows the magnetic field dependence of the RMCD signal of a 7-SL $MnBi_2Te_4$ device.A narrow hysteresis can be seen near zero magnetic field due to uncompensated magnetization in odd layer-number devices. By increasing the magnetic field, the sample enters the cAFM state at the spin-flop field $\mu_0 H \approx 3.8$T, manifested by the sudden jump of the RMCD signal and ρ_{xx}, ρ_{yx}. We note that as soon as the spin-flop transition occurs, the Hall resistivity ρ_{yx} quantizes to about $-h/e^2$ (middle panel), and the longitudinal resistivity ρ_{xx} drops from $\approx 100k\Omega$ to near zero (bottom panel). This indicates the formation of a $C = 1$ state accompanying the spin-flop transition. As the magnetic field further increases, the canted spins rotate towards the out-of-plane direction and eventually become fully polarized at $\mu_0 H \approx 7.2$T with saturated RMCD signal (up panel).

The cAFM Chern insulator is further supported by exploring the topological phase diagram in dual-gated devices over a broad range of magnetic field. Figure 2.3 **a** is a 2D color map of ρ_{yx} in a 7 SL dual-gated $MnBi_2Te_4$ device as a function of both $\mu_0 H$ and gate-induced carrier density n_G at electric field $D/\epsilon_0 = -0.2$V/nm. Here n_G partly compensates for the residual carrier density in the sample and tunes the Fermi level. The electric field D/ϵ_0 is defined to be positive when it points from top to bottom gates. At low field and low carrier density, due to the very high resistivity of the trivial insulator state, the ρ_{yx} shows an overload feature. This magnetic trivial insulator ground state in 7SL device is repeatedly observed and inconsistent with predicted quantum anomalous Hall insulator, which remains outstanding. Very recently, it was found that introducing extra capping layer can help to maintain the quantum anomalous Hall state[109]. Notably, in the range of $n_G = 1.0 \sim 2.0 \times 10^{12}\text{cm}^{-2}$, a sharp phase boundary of the $C = 1$ state is observed near the spin-flop field $\mu_0 H_{C1} \approx 3.6$T. This further demonstrates that the formation of $C = 1$ state is coupled to the cAFM order. We note that the observation of cAFM Chern insulator has been observed in a wide range of devices from 4 and 6-8 SLs devices. This intimate relationship between the topological and magnetic phase transitions in $MnBi_2Te_4$ can be understood as follows. Due to the easy-axis anisotropy, the transition from the AFM to the cAFM state is a first-order phase transition: at the spin-flop field, the magnetization in each SL suddenly rotates into the cAFM state with a finite canting angle. The abrupt change of the magnetic state is accompanied by the formation of the Chern insulator gap, hence a

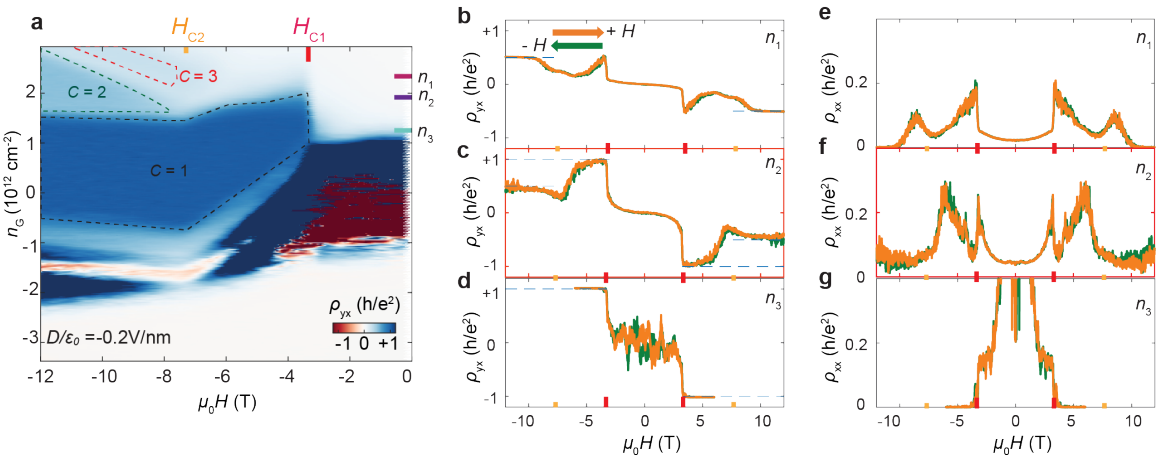

Figure 2.3: Observation of Chern insulator to orbital quantum Hall states phase transition. **a**, unsymmetrized ρ_{yx} as a function of magnetic field $\mu_0 H$ and gate induced carrier density n_G at fixed electric field $D/\epsilon_0 = -0.2\text{V/nm}$. Black, green and red dashed lines enclose $C = 1, 2, 3$ quantum Hall states, respectively. The dashed lines are contours defined by $\rho_{yx} = (0.97, 0.47, 0.30)h/e^2$. Carrier densities n_{1-3} and critical magnetic fields $\mu_0 H_{C1}$ and $\mu_0 H_{C2}$ are marked on the axis. $(n_1, n_2, n_3) = (2.23, 1.87, 1.29) \times 10^{12}\text{cm}^{-2}$. Note that for $|\mu_0 H| < |\mu_0 H_{C1}|$ and n_G in the range of $-1 \sim 1 \times 10^{12}\text{cm}^{-2}$, since the sample is very insulating (i.e. $\rho_{xx} > 1\text{G}\Omega$), the excitation current flowing through the sample is not stable and thus ρ_{yx} shows a fluctuating signal with positive and negative values. **b-d,** anti-symmetrized ρ_{yx} as a function of $\mu_0 H$, under different carrier density n_{1-3}, and **e-g**, the corresponding symmetrized ρ_{xx}. Orange and green curves correspond to magnetic fields sweep up and down, respectively.

change in the Chern number. Further increase of the magnetic field results in a continuous rotation of the canted spins, which is expected to cause an adiabatic change in the size of the Chern insulator gap until the system enters the FM state. This understanding also naturally fills the gap between our observation of cAFM Chern insulator and previously observed FM Chern insulator. As the bandgap in cAFM and FM state are adiabatically changed, the stability of Chern number ensures a cAFM Chern insulator state as long as the band gap are not closed by external disorder or temperature factor.

When $\mu_0 H$ is above $|\mu_0 H_{C2}| \approx 7.4$T, the sample enters the magnetic field induced FM state. A rich topological phase diagram is uncovered, in which the topological states with corresponding Chern numbers are identified based on $\rho_{yx} \approx h/Ce^2$ and nearly vanishing . In addition to the $C = 1, C = 2$ and 3 states, characterized by $\rho_{yx} \approx h/Ce^2$, appear at higher n_G. Unlike the $C = 1$ phase, the contours of $C = 2$ and 3 phases are linearly dependent on magnetic field $\mu_0 H$ (Fig. 2.3 **a**). This implies that the $C = 2$ and 3 states are a result of the Landau level (LL) formation coexisting with edge state from band topology. For the $C = 1$ phase, there is only a single region present in the phase diagram. So, the $C = 1$ Chern insulator state in the cAFM is adiabatically connected to the same state in the field-induced FM phase.

Figures 2.3**b-g** plot the $\mu_0 H$ dependence of ρ_{yx} and ρ_{yx} at three selected n_G. For heavy electron doping $n_1 \approx 2.23\times10^{12}\text{cm}^{-2}$, $\rho_{yx} \approx 0$ and $\rho_{xx} \approx 0.005h/e^2$ near zero magnetic field. As $|\mu_0 H|$ increases, we see a kink-like feature, namely a sudden increase of both ρ_{yx} and ρ_{xx} related to the AFM to cAFM transition at HC1 (Figs. 2.3**b** and **e**). For $|\mu_0 H| > 10$T, ρ_{yx} approaches $0.5h/e^2$, indicating a $C = 2$ Chern insulator state. For $n_2 \approx 1.87 \times 10^{12}\text{cm}^{-2}$, upon entering the cAFM phase at $|\mu_0 H| \approx 3.6$T, the sample first goes into the $C = 1$ state with $\rho_{yx} \approx h/e^2$ and $\rho_{xx} = 0.05h/e^2$. At a higher magnetic field $|\mu_0 H| \approx 10$T, it then switches into the $C = 2$ state with $\rho_{yx} \approx 0.5h/e^2$ and $\rho_{xx} = 0.05h/e^2$ (Figs. 2.3**c**& **f**). This phase transition from the $C = 1$ state into a higher Chern number $C = 2$ state as $|\mu_0 H|$ increases at a fixed carrier density is unusual. Increasing $|\mu_0 H|$ increases the degeneracy of LLs. Therefore, if the quantization is caused by the formation of LLs, then the quantum Hall plateau should always change from higher to lower Chern numbers as the magnetic field increases at a fixed carrier density. The opposite observation here further supports

our interpretation that the $C = 1$ state observed in the cAFM phase is a Chern insulator originating from the intrinsic nontrivial band structure, while the $C = 2$ state in the FM state is the quantum Hall state due to the formation of LLs. For $n_3 \approx 1.43 \times 10^{12}\text{cm}^{-2}$, close to the charge neutral point, the transport data shows an abrupt formation of a $C = 1$ Chern insulator at spin-flop field H_{C1}, consistent with our discussions above (Figs. 2.3**d** and **g**). The sharp transition exists over a finite doping range, implying that a finite magnetic exchange gap opens suddenly with the spin-flop transition from the AFM to the cAFM phase. This further validates the conclusion that the electronic structure is coupled to the magnetic order.

2.2 Chern insulator devices

The intrinsic van der Waals magnetic topological insulators have more tuning knobs and can be used to demonstrate potentially useful electronics harnessing dispationless edge conduction.

2.2.1 Topological current divider

The layered nature of $MnBi_2Te_4$ gives rise to another control knob in addition to electrostatic gating. First, we demonstrate a topological current divider (TCD) based on layer domain device. Fig. 2.4 illustrates the ideas and characterization of such as a TCD. Full data and discussion can be found in [80].

The technical goal is to realize a device, within which two domains have different Chern number. This is achieved by mechanically exfoliating $MnBi_2Te_4$ and searching domain flakes. With such an approach, the device is fabricated with different domain as shown in Fig. 2.4 a-b, where the two domains are labelled as Domain-I and Domain-II.

Transport measurement at temperature $T = 50$ mK was used to validate the edge state equilibration. In the measurement shown in Fig. 2.4 c-e, the division of current injected at contact 1 between contacts 8 and 9 as a function of V_{bg} and $\mu_0 H$. The black dashed line outlines the region where $C_I = 1$, $C_{II} = 2$ and the device works as a $1:1$ chiral edge current divider. The white dashed line outlines the region with $C_I = C_{II} = 1$, where there is no edge state along the boundary and the current is not divided but is all conveyed to contact

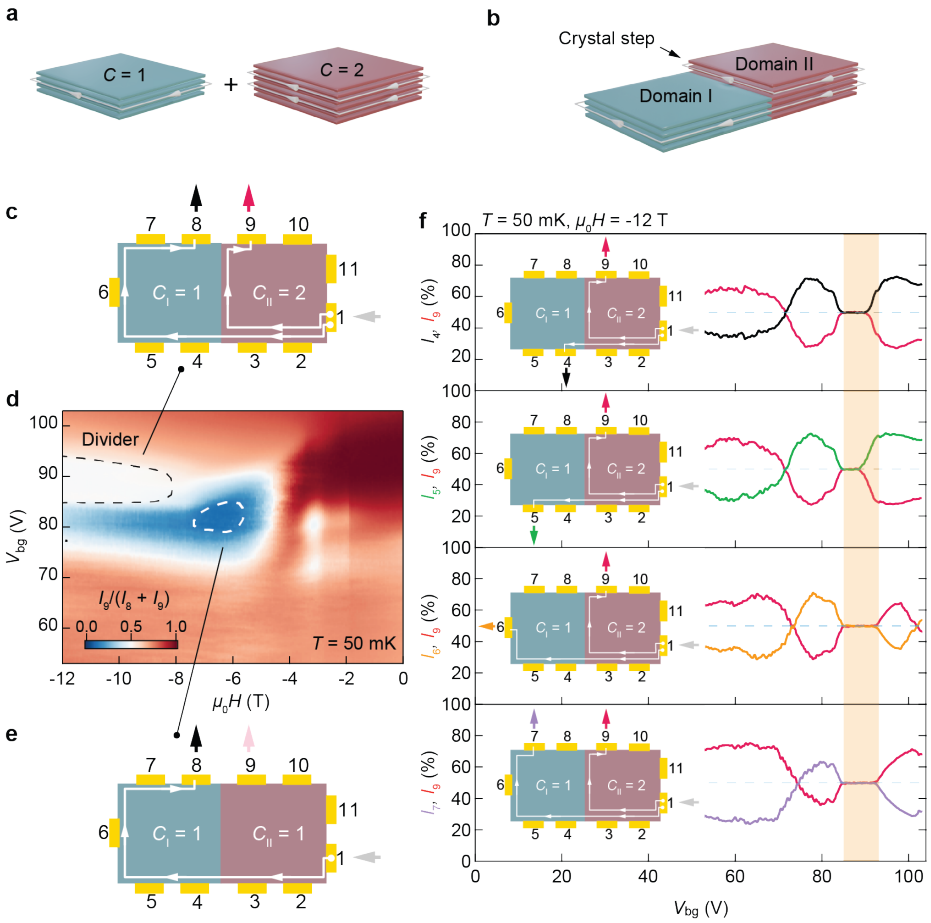

Figure 2.4: A topological current divider based on Chern insulator layer domain junction.**a-b**, illustration of Chern number domain. **a**, at different gate voltage, the device with different layer can have different Chern number $C = 1$ and $C = 2$. In **b**, the two domains are physically connected seamlessly and domain boundary is a atomically sharp crystal step. **c-e**, Chern number of each junction at different parameters. **d**, divider coefficient $\frac{I_8}{I_8+I_9}$ as a function of $\mu_0 H$ and gate voltage V_{bg}. The divider works in high field when the thicker domain is $C = 2$ and the other is $C = 1$ in **c**. **e**, in lower field, although the device consists of two physical layer domain, the Chern number of each domain is the samee. **f**, Chern domain functionality as a function of gate voltage at fixed $\mu_0 H$ and different geometry.

8 via a single edge state on the perimeter of the flake. In the low-field limit $|\mu_0 H| < 4$T and close to charge neutrality (85 V $< V_{bg} <$ 95 V), most of the current flows from contact 1 to the nearest contact 9 via bulk conduction, because the chiral edge states do not exist in the AFM phase.

We can also show that the topological equivalence of contacts that are connected by single chiral edge state. In Fig. Fig. 2.4 f, we show that in the appropriate gate range (85 V $< V_{bg} <$ 95 V), the current splitting obtained using any of contacts 4, 5, 6 or 7 to Domain I is identical to that using contact 8 as in Fig. 2a, b, i.e., the current injected at contact 1 in Domain II is always divided 1:1 at the Chern junction (see also Supplementary Fig. 5). Note that small changes in the gate range for current divider operation in Fig. 3a might be related to small Fermi level variations across the device, which has a large lateral size of $\sim 100\mu$m

The ideas of using magnetic or layer domains to constructre TCD is not restricted to $MnBi_2Te_4$ single material system. In fact, more traditional magnetically doped topological insulators are also capable to do so [94].

2.2.2 Topological field effect transistor

Having demonstrated a Chern insulator junction, we proceed to demonstrate a topological field effect transistor. An ideal Chern insulator supports bulk-conductive conduction and valence band electron, and edge-conductive Chern gap state. So everywhere in the phase diagram, the Chern insulator is conductive in the bulk or edge. How can we switch off the conductivity completely? An apparent way is to harness the tunability to invert the topological band gap to be trivial. Here we demonstrate an effective alternative way, where we can harness the disorder inside the valence band. The device to detect such a disorder phase is shown in Fig. 2.5a that has a global backgate and locally defined top gates. Data was taken at a temperature around $T = 2$ K and a magnetic field ≈ 4 T was applied so that $MnBi_2Te_4$ is in its canted AFM state. Fig. 2.5b show two terminal resistance as a function of global backgate. When the device is heavily doped, $V_{bg} > 35$V, $V_{bg} < 15$V, the sample is highly conductive. While when the Fermi level is tuned to be within bandgap, the Chern

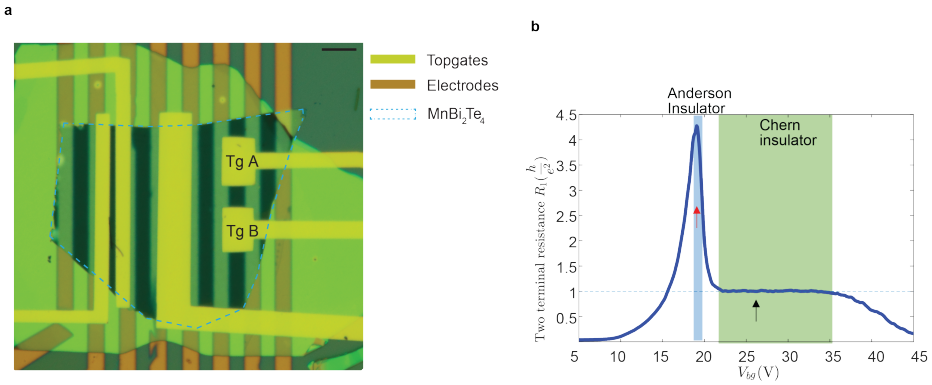

Figure 2.5: Topological field effect transistor. **a**, optical image of the $MnBi_2Te_4$ device. The device has a global back gate and with several splitted top gate to perform electrostatic control on each part. **b** Two-terminal resistance as a function of global back gate voltage V_{bg} in cAFM state. When the resistance is high, the bulk and edge are both insulating. When the resistance is quantized, the only edge channel contributes to the conductivity.

insulator phase emerges as the well-quantized plateau $R = \frac{h}{e^2}$ around $23\text{V} < V_{bg} < 35\text{V}$. Remarkably, a highly resistive peak emerges around the valence band edge $V_{bg} \simeq 18\text{V}$. Mechanism can be speculated as more and more works appear to discuss the disorders in this special system. Potential candidates are Anderson insulator or the zeroth landau level because a finite magnetic field is needed. We speculate this state is due to disorder and thus noted as an Anderson insulator. The resistive peak has weakly insulating behavior, and only exists in canted-AFM state, suggesting that magnetic disorder may contribute to the formation of such state. A closer check of previous data reported in similar $MnBi_2Te_4$ devices also shows phase separation between this resistive state and zeroth Landau level in high magnetic field and ferromagnetic state.

Now we turn to $MnBi_2Te_4$ device, a Chern transistor, that has controllable number of edge states by using the field effect mentioned above that switch on and off all transport from bulk and edge. Device is controled by a global backgate to set the bulk state and two split gate Tg A and Tg B, as shown in 2.5, a.

The transport characterization is shown in Fig. 2.6. Data was taken at a nominal

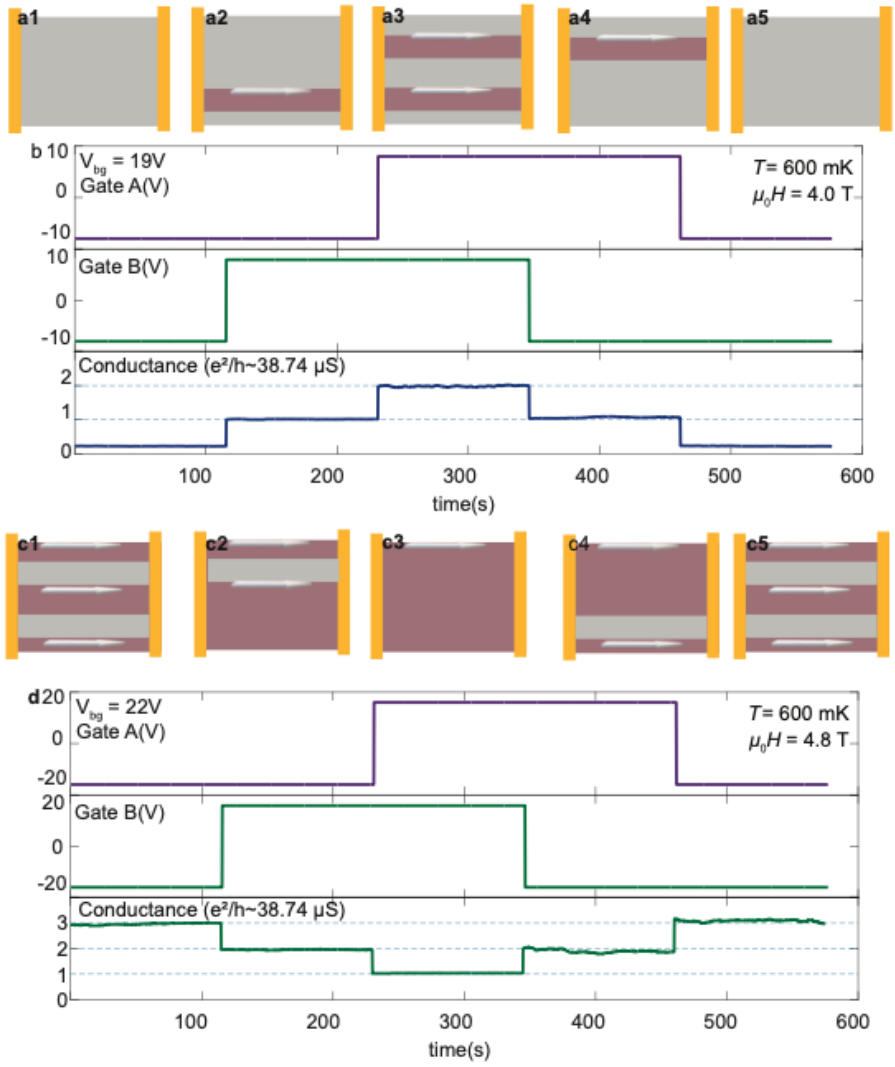

Figure 2.6: Operation of a Chern transistor. **a1-a5**, controlling edge transport with local gates in the insulating phase. A global backgate was used to control the device to be in a global insulating state in **a1**. Then two local top gates are turned on to gate the parts to be in the Chern insulator phase in sequence. Each local top gates create an addition edge states, signaled by quantized contactance $0, 1, 2\frac{e^2}{h}$ per on-state local top gates as shown in **b**. **c1-c5**

temperature of 600 mK. Fig. 2.6 shows that the device is turned off with the global backgate and local topgates. As shown in Fig. 2.6 b, the two terminal conductance $G \ll e^2/h$ signals an insulating phase with no bulk and edge transport. Then, the topgates are turned on one by one, by ramping the voltage to $V_{\text{tg}} = 10V$. When one (two) top gate is turned on, the conductance increases to $G = 1(2)e^2/h$. The quantization and the fact that the edge transport happens only when top gates are turned on indicate that the conduction happens in the edge of topgates region.

The device can be also operated in a purely edge conductivity scheme as shown in Fig. 2.6 c-d. In Fig. 2.6 c1, the device is gated into Chern insulator regime with the backgate, while the split gate turns the domains into insulating regime. The conductivity $G = 3h/e^2$ suggests the emergence of one edge state on the boundary of the sample and two edge states on the boundary of the split gated domain. Then, the split gates turn the domain into Chern insulator regime by ramping down the voltages. The conductivity decreases from $3h/e^2$ to $2h/e^2$ and h/e^2.

The measurement demonstrates a Chern insulator transistor that the conductivity can be completely switched off. It's ability to convert continues gate voltage range to a discrete quantized conductivity make it very promising for rectification purpose for high performance analog to digital converter. Furthuermore, the discovery of the edge state between a Chern insulator and a possible magnetic disorder induced Anderson insulator can be fundamentally interesting if this can be verified by real space imaging technique.

Further focus on this $MnBi_2Te_4$ system and related compound should address the reproducibility issue, especially Chern insulator state in zero field that exhibit quantum anomalous Hall effect[96, 110]. The material issue, esspeically the absence of quantized anomalous Hall effect at zero magnetic field, have significantly complicated the interpretation and understanding of the system. Recently, material physicists have made progress in solving the issue and started to observate quantized anomalous Hall effect in both 5SL and 7SL $MnBi_2Te_4$ device[109]. Other magnetic topological system with intrinsic magnetism is also promising[93]. If an appropriate van der Waals material system with robust quantum anomlaous Hall effect can be found, it will be promising to use moiré engineering to introduce miniband such as interfacing with twisted hexagonal boron nitride or transition metal

dichalcogenide. As we will see from next chapter, introducing moiré has the potential to create strong correlation to the system.

Summary 2: Chern insulator with intrinsic magnetism and devices

- Chern insulator can be found in magnetic topological insulator with intrinsic magnetism.
- Combined measurements of optics that identifies magnetic state and transport measuremnt that probes topology of the band can be helpful to understand Chern insulator systems.
- Functional devices can be made using robust Chern insulators such as current divider and topological field effect transistor.

Chapter 3

SYMMETRY-ENRICHED CHERN INSULATORS IN TWISTED GRAPHENE SUPERLATTICES

Condensed matter physicists were once thought to be a group of people who grew crystals and measured their thermodynamics by applying magnetic fields and temperature. The invention of the field-effect transistor, where a gate voltage can be used to modulate the electron gas trapped in semiconductors, has revolutionized this picture.

These electron gases, once confined in two dimensions and subjected to a high magnetic field, can exhibit the quantum Hall effect [10]. The high magnetic field creates cyclotron orbits that give rise to a characteristic length $l_{\mathrm{B}} = \sqrt{\frac{\hbar c}{eB}}$, where B is the strength of the external magnetic field. The filling number of these cyclotron orbits defines the magnetic filling number. The cyclotron orbits, or Landau levels, have almost quenched kinetic energy. Many interaction-related phase transitions can happen, such as internal symmetry or translational symmetry breaking phases.

As we saw in the previous chapter, the requirements for topological aspects in Landau levels can be replaced by a Chern number [24]. This chapter will reveal that moiré engineering of two-dimensional materials can give rise to strong interaction effects by creating flat bands, similar to those brought in by a magnetic field. We will focus on some strongly correlated Chern insulators with broken internal or translational symmetry, very similar to the quantum Hall ferromagnetism discovered decades ago [67, 111], in twisted graphene systems, particularly twisted bilayer graphene (TBLG) and twisted double bilayer graphene (TDBG).

3.1 Symmetry breaking phases in magnetic field

We first take a look at a more traditional quantum Hall system, the quantum Hall effect in monolayer graphene [66, 65]. The standard quantum Hall sequence of graphene at a low enough magnetic field is given at $\nu = \pm 2, \pm 6, \pm 10, ...$ instead of the prominent gapped

states at $\nu = \pm 4, \pm 8, \pm 12, ...$ Because of the presence of spin and valley, each Dirac band of graphene is four times degenerate, called spin-valley degeneracy. This corresponds to $|\delta\nu| = 4$. The Dirac band also gives rise to a Berry phase of π winding number for the Dirac cone. This corresponds to $|\nu|_{min} = 2$.

When the magnetic field is high enough, the spin-valley degeneracy is lifted. The same measurement of the quantum Hall sequence now gives rise to all integer quantum Hall plateaus at $\nu = \pm 1, \pm 2, \pm 3, ...$ This is due to the Zeeman energy coupling the spin to the material and interactions at the lattice scale. The symmetry-broken quantum Hall states, or quantum Hall magnets, have complicated patterns when taking internal degrees of freedom into account, such as canted antiferromagnetic states and skyrmion states [67, 112, 113].

3.2 Moiré effect and flat band in graphene

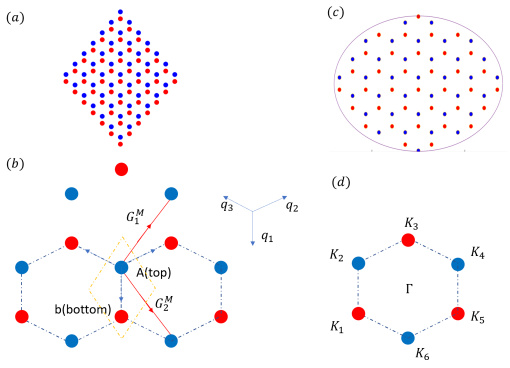

Figure 3.1: Illustration of MacDonald-Bistritzer model in reciprocal space. (a,c)The K_M space lattice configuration generated by translation boundary condition or circle condition. (b) The Hamiltonian and hoping in K_M space. (c)FBZ of the moiré BZ.

When two sheets of atomic lattices are stacked together, a long-wavelength moiré pattern will emerge [77, 75]. This moiré pattern is very similar to the atomic potential: the different stacking order spatially modulates the state and introduces a new energy scale. This moiré potential can sometimes strongly hybridize the original electron wave function and form new Bloch states at moiré periodicity. Experimentally, the energy scale can be as small as $\approx$ 10 meV and the carrier density required to fill one moiré miniband can be a few $\approx \times 10^{12}$ cm^{-2}. This suggests that multiple electrons or holes can be charged using electrostatic gates into the moiré miniband up to a few integer fillings per moiré unit cell. On the contrary, in atomic bands, the filling number can only be tuned very pertur-

batively in a similar electrostatic gating scheme, and changing electrons per lattice usually requires chemical doping.

We now introduce the (generalized) MacDonald-Bistritzer model [114] to capture the low energy physics of twisted graphene systems.

The essence of single-particle band structure calculation is that the interlayer hopping becomes a tight-binding one due to its exponential decay nature in moiré momentum space, denoted by K_M, with an associated reciprocal vector $G_M^i, i = 1, 2$. The moiré K_M space is constructed by a normal band folding technique. The top layer and bottom layer Hamiltonian serves as an on-site potential on folded K_M space, while the inter-site hopping is defined by the Fourier transformed inter-layer tunneling, which is truncated into a tight-binding one.

Fig3.1 shows how we can generate the K_M space by different methods. (i) By using $K^{A,B} = G_0^{A,B} + mG_1 + nG_2$ and truncating the space by imposing $|m| < M, |n| < N$. The resulting lattice captures the translational invariance in K space, thus keeping the maximum Wannier localization in real space. (ii) By imposing $N\Omega_{BZ} < \pi R^2$ where Ω_{BZ} is the area of a plateau, we can get a high symmetry K-space truncation. This method will be more accurate when adding a magnetic field because it naturally recovers the Landau level's rotational invariance.

After building the lattice, we may assign corresponding Hamiltonian $H_{top/bottom}$ to each lattice. Our choice is shown in Fig3.1(b).

3.2.1 K-space TB model

Specifically, we use the following $k \cdot p$ model for bilayer and Dirac model for monolayer. Multilayer can be treated in a similar manner[115].

The monolayer model is:

$$H_{\text{Dirac}}(\mathbf{k}) = \begin{pmatrix} 0 & v_f(k_x + ik_y) \\ v_f(k_x - ik_y) & 0 \end{pmatrix} \tag{3.1}$$

where we choose $v_f = 566\text{meV}$.

The bilayer model is:

$$H_{\text{bilayer}}(\mathbf{k}) = \begin{pmatrix} \Delta & v_f(k_x+ik_y) & \frac{\sqrt{3}}{2}a_0\gamma_4(-k_x+ik_y) & \gamma_1 \\ v_f(k_x-ik_y) & 0 & \frac{\sqrt{3}}{2}a_0\gamma_3(-k_x-ik_y) & \frac{\sqrt{3}}{2}a_0\gamma_4(-k_x+ik_y) \\ \frac{\sqrt{3}}{2}a_0\gamma_4(-k_x-ik_y) & \frac{\sqrt{3}}{2}a_0\gamma_3(-k_x+ik_y) & 0 & v_f(k_x+ik_y) \\ \gamma_1 & \frac{\sqrt{3}}{2}a_0\gamma_4(-k_x-ik_y) & v_f(k_x-ik_y) & \Delta \end{pmatrix} \tag{3.2}$$

where we choose realistic parameters as $(\gamma_1, \gamma_3, \gamma_4, \Delta) = (361, 283, 138, 15)$meV.

The momentum, as the input of these Hamiltonians, will be rotated by $\pm\theta/2$ depending on whether it is the top layer or bottom layer. Then these Hamiltonians will be put into a block-diagonal form. The inter-block elements will be zeros and filled with hopping matrices.

We use the following hopping matrices, which can be found in a broad class of literature:s:

$$T_n = \begin{pmatrix} \omega' & \omega e^{in\frac{2}{3}\pi} \\ \omega e^{-in\frac{2}{3}\pi} & \omega' \end{pmatrix}, n = 0, 1, 2 \tag{3.3}$$

Here we choose $\omega = 120$meV(note that $\gamma_1 = 3\omega$) and $\omega' = (0.6 \sim 0.9)\omega$ according to the system we treat. The difference between ω and ω' is a phenomenological choice to include the lattice relaxation. Physically $\omega = t_{AA}$ and $\omega = t_{AB}$ can be obtained differently from *ab initio* calculation. Then hopping matrix T_n corresponds to bonds that carry momentum q_{n+1} as shown in Fig3.1. The hopping matrix will be kronecker product to form appropriate form of matrix.

We construct a Hamiltonian:

$$H_0 = \begin{pmatrix} H_t(R_{\theta/2}k) & T_0 \otimes I & 0 & 0 & \cdots \\ (T_0 \otimes I)^\dagger & H_b(R_{-\theta/2}(k-q_1)) & T_1 \otimes I & 0 & \cdots \\ 0 & (T_0 \otimes I)^\dagger & H_b(R_{-\theta/2}(k-q_2)) & T_2 \otimes I & \cdots \\ 0 & 0 & (T_0 \otimes I)^\dagger & H_b(R_{-\theta/2}(k-q_3)) & \cdots \\ \vdots & \vdots & \vdots & \vdots & \ddots \end{pmatrix} \tag{3.4}$$

By diagonalizing the Hamiltonian above, we arrive at the single-particle energy band. The spin degree of freedom is degenerate. The valley degree of freedom is connected by

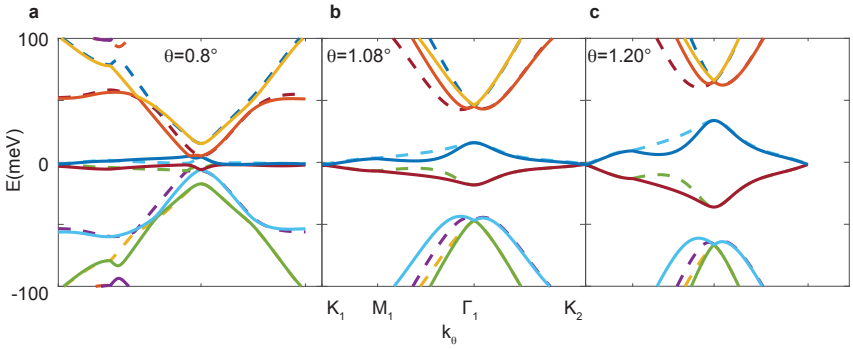

Figure 3.2: Band structure of twisted bilayer graphene with different twist angle using MacDonald-Bistritzer model. **a-c**, band stucture for twist angle $\theta = 0.8°$(**a**), $1.08°$ (**b**), or $1.20°$(**c**).

time-reversal symmetry, so it is also degenerate despite a difference in the definition of lattice momentum. We have the following relations if we evaluate the momentum from one K-point:

$$\begin{aligned} E_{\sigma,\pm}(\mathbf{k}) &= E_{\sigma,\mp}(2k_\Gamma - \mathbf{k}) \\ u_{\sigma,\pm}(\mathbf{k}) &= u^*_{\sigma,\mp}(2k_\Gamma - \mathbf{k}) \end{aligned} \tag{3.5}$$

Where k_Γ is the momentum of Γ evaluated in this coordinate. In practice, we can simply calculate one valley and get another with the formula provided above.

The validity of this valley decoupling relies on the approximation that moiré scale physics is decoupled from atomic scale physics, i.e., in the small angle limit.

The numerical calculation can be easily done in a modern personal computer with Tflops calculation ability.

Fig. 3.2 shows band structure calculation based on MacDonald-Bistritzer model using a phenomenological lattice relaxation parameter $\alpha = 0.8$, for various twist angle for TBLG. The bandwidth for the band near charge neutrality ($E \approx 0$) can be as small as $15meV$ that is comparable to Coulomb interaction between doped carrier. Although the band has nontrivial topology, an extra symmetry $C_2\mathcal{T}$ protects a gapless point for TBLG near charge neutrality. An additional alignment to the substrate hexagonal boron nitride can efficiently break this symmetry and help the system favor time-reversal symmetry-breaking phases in

the absence of a magnetic field. In the following, we will use a moderate magnetic field to break time-reversal symmetry. Another notable thing is that for TBLG, the strong interlayer hybridization $t \approx 110$ meV is larger than electrostatic gate tunability by a magnitude in experimentally feasible setups. Thus, the vertical displacement field D/ϵ_0 will do very little to the band structure. However, in any twisted multilayer, the stacking in the untwisted layer ensures gate tunability of the composition. For example, Bernal-stacked bilayer graphene can acquire a gap when applying a magnetic field. Thus, D/ϵ_0 is a tuning knob for twisted multilayer systems.

Next, we can examine if the generalized MacDonald model can capture single-particle physics by comparing the calculated density of states and any thermodynamic measurements [81]. We will focus on TDBG for this purpose as TDBG benefits from extra electric field tunability that helps us to compare single-particle calculations.

Fig. 3.3 displays such a comparison between theory and experiment. Fig. 3.3**a** displays the device geometry, where we adopt dual gate device structure consisting of a hBN dielectric and a graphite gate electrode. Next, Fig. 3.3**b** shows band stucture calculation for various electric field. Although there is no gap for charge neutrality when $U = 0$(correspond to $D/\epsilon_0 = 0$), an experimental feasible U can open a single particle band gap near charge neutrality as well as remote band gap for full filling of a band. Such gate tunability is further illustrated in Fig. 3.3**c** where the density of states are calculated for different filling number and vertical potential. Although the theoretical calculated ν and U cannot be easily translated into experimental value of n and D/ϵ_0, we expect that they are monotonomicly related to each other. Fig. 3.3**d** shows high temperature longitudinal resistance measurement ρ of a TDBG device with twist angle $\theta = 1.30°$. The experimental result, especially the emergence of resistive state at high D/ϵ_0, $\nu = \pm 4$, as well as cross-like structure of laterally known as van Hove singularity near $-4 < \nu < 0$, demonstrates that the generalized MacDonald-Bistritzer model can capture the single particle physics.

When the device is further cooled down, extra insulating states emerge at $\nu = 1, 2, 3$ at finite electric fields. Such features cannot be captured by single-particle calculations, so these states have a correlated nature. These states are thus called correlated states.

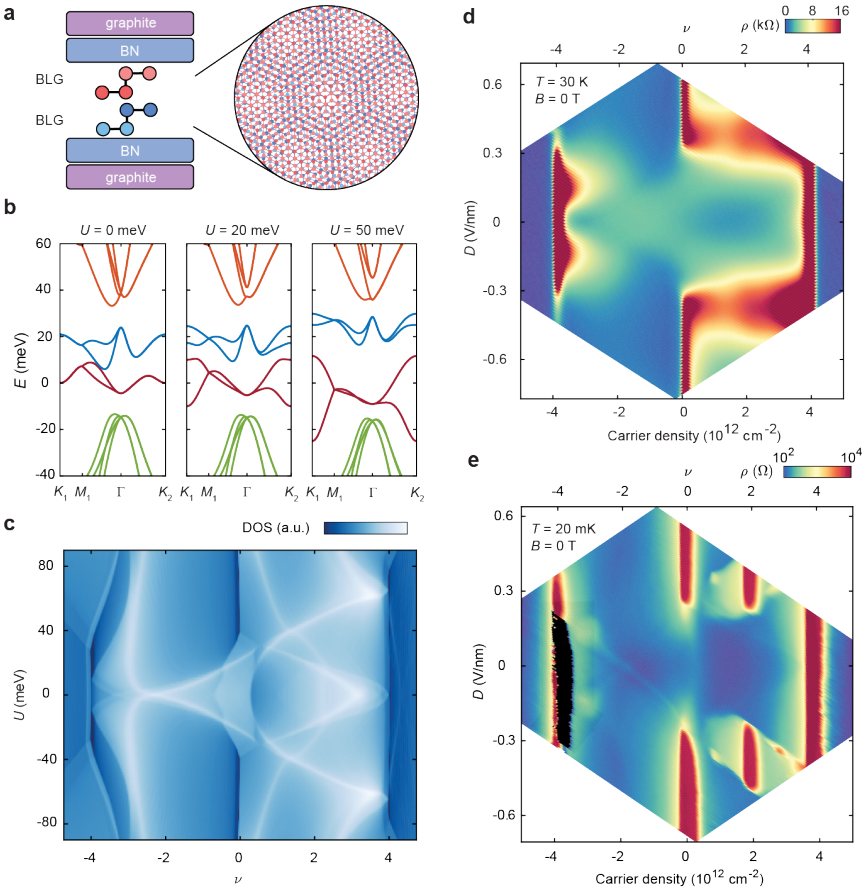

Figure 3.3: Validation of continuum model that captures single particle physics in TDBG. **a**, Schematic of a tDBG device encapsulated in hexagonal boron nitride (hBN) with graphite gates. **b** Calculated band structure of tDBG with $\theta = 1.3°$ at various values of interlayer potential (U). Colouring indicates different moirésubbands. **c** Calculated density of states (DOS) as a function of ν and U, plotted on a log colour scale. **d** Resistivity of a tDBG device (colour scale) with $\theta = 1.3°$ at $T = 30$ K. The corresponding band filling factor ν is shown on the top x axis. **e** Resistivity at $T = 20$ mK. The black region corresponds to artificially negative resistance in the contacts used for this measurement.

3.3 Strongly correlated Chern insulators at integer fillings

Notably, the band of twisted graphene can sometimes be topological. In twisted bilayer graphene near the magic angle, the band acquires a nontrivial spin-valley Chern number. However, the bands touch each other, which is protected by a C_2T symmetry, where C_2 is the mirror symmetry and T the time-reversal symmetry. Simultaneous breaking of this symmetry has not been observed. However, a moderate magnetic field can break T symmetry. The spin-valley subband will acquire a finite Chern number. These Chern bands at finite magnetic fields have some interesting properties and host strongly correlated phases, which will be the focus of this section.

As described before, monolayer graphene has spin-valley degeneracy and a Berry phase around the Dirac point, which gives anomalous Landau levels. At high magnetic fields, the interaction effect can break this symmetry and give rise to quantum Hall magnetism. Surprisingly, for a Chern band at a finite magnetic field in twisted bilayer graphene, the requirement of a high magnetic field is loosened to a weak magnetic field, which is required to break C_2T symmetry. The interaction comes from the narrow moiré band.

Info 3.1: Streda formula

A unique feature of the Chern insulator state is the chiral edge state that has localized density along the edge of the sample, described by chiral Fermi liquid or Luttinger liquid theory. Quantum Hall states or Chern insulator states seem quite trivial if you live in the bulk and remain in the ground state: they are gapped, i.e., a finite energy is required to excite any charge or neutral excitations associated with the electron spectrum. However, the topological bulk state indeed has an observable effect which deeply connects to bulk-edge correspondence. Measurements can be done on the bulk, localized area to access the Chern number of the Chern insulator states.

Consider a zero-temperature, magnetically saturated (but with finite magnetic moments) incompressible liquid with conserved particle number. The minimal grand potential is $dG = M \cdot n \wedge dB + \mu \wedge dn$, where M is a one-form magnetization and n is the one-form corresponding to the normal vector. $M \cdot n$ yields a zero form of a scalar. μ is the chemical potential. B is the magnetic field applied along n. If there is no first-order phase transition, dG is a well-defined

closed one-form due to thermodynamic considerations, and thus $d \wedge dG = 0$, so we have:

$$\left(\frac{\partial M}{\partial \mu}\right)_B = \left(\frac{\partial N}{\partial B}\right)_\mu \tag{3.6}$$

Now we consider applying an electric field $\mathcal{E}$ and the system being in quasi-equilibrium. We have $\mathcal{E} = \nabla(\mu/e)$. The bulk of the system is gapped, so that only edge conductivity contributes to the magnetization, satisfying $\mathcal{J} = c\nabla \times M$. It is easy to check that $\mathcal{J}$ is nothing but the net Hall current. We have, thus,

$$\mathcal{J} = ec\mathcal{E} \wedge \frac{\partial N}{\partial B}_\mu \tag{3.7}$$

From the current form's definition, $\mathcal{J} = \sigma \cdot \mathcal{E} + \mathcal{E} \wedge \mathcal{K}$, we have the Hall conductivity, which is the anti-symmetric part of the conductivity tensor, $\mathcal{K}$:

$$\sigma_{xy} = -ec\frac{\partial N}{\partial B}_\mu \tag{3.8}$$

Streda has discovered two ways of deriving this: first with the Kubo formula and linear response theory, then with thermodynamic considerations [116, 117]. Here, I provide the simplest form of it.

The physical intuition of this Streda formula is straightforward: the chiral edge state contributes to a non-zero bulk magnetization that counteracts the applied field. The number of particles occupying the bulk states decreases, and thus additional particles have to be added to maintain the chemical potential.

Looking back to the derivation, we have three assumptions:

- The system is fully gapped.
- The system is magnetically compensated.
- There is no first order phase transtions (like magnetic hysteresis) involving.
- Static (quasi-equalibrium) limit has been taken. So the system must be in its linear response regime.

We can try to loosen some of the constraints. For a gapless system, it's straightforward to verify that the Streda formula has the form $\sigma_{xy} = \sigma_1 - ec\frac{\partial N}{\partial B}\mu$, where σ_1 is a density-dependent classical term which can be derived from Boltzmann transport theory or the Kubo formula [116]. When the system is gapped, σ_1 will vanish. In an extreme limit where the

magnetic field is very high, Galilean invariance will guarantee the form $\sigma xy = -ec\frac{N}{B}$, which relates to the linear Hall effect as $\sigma_{xx} \to 0$. For a magnetic system where the anomalous Hall effect can be present, we have to consider how magnetization relates to the magnetic field in detail. It is also quite interesting to discuss nonlinear and nonequilibrium effects [118, 119, 120, 121, 122].

We observed a rich Landau fan diagram and various Chern insulator phases as shown in Fig. 3.4. Because of the moiré effect discussed before, TBLG has very strong correlations that spontaneously break spin and valley degeneracy, which gives rise to gapped phases between the band gaps of $\nu = \pm 4$ and the charge neutral point. Notably, in this specific device, $\nu = -2, -3$ and $\nu = 0, 1, 2, 3, 4$ are gapped, signaled by large longitudinal resistance at a magnetic field $\mu_0 H = 0$. The $\nu = -1$ state is believed to exhibit the Pomeranchuk effect[123, 124], which becomes weakly insulating at intermediate temperatures but conductive at low temperatures.

A series of Chern insulators is formed from the integer filling number and has an integer Chern number. A cascade of strongly correlated Chern insulators (CCI), which are the lattice analogs of quantum Hall ferromagnetism, can be observed. As we see in quantum Hall ferromagnetism, the interaction lifts up spin and valley degeneracy. Here, the degeneracy is lifted by moiré. The small magnetic field breaks C_2T symmetry. We observed that the dominant Chern numbers for $\nu = \pm 1, \pm 2, \pm 3$ are $C = \pm 3, \pm 2, \pm 1$.

3.4 Translational symmetry breaking Chern insulators at fractional fillings

We now proceed to discuss another family of Chern insulators in the presence of strong interaction. The interaction effect can not only break spin-valley flavor symmetry via Hund's-like coupling or orbital magnetism, it can also break translational symmetry. For example, it can break the spatial symmetry defined by the moiré potential landscape, forming charge density waves at fractional fillings. When this happens in a Chern band, the fate of the Chern band is band folding, which will form extra bands that carry non-zero Chern numbers, i.e., $t \in \mathbf{Z}$ but $s \in \mathbf{Q}/\mathbf{Z}$, referred to as topological charge density waves.

Figure 3.5 a,c show the two groups of TCDW states observed at hole doping side, with the main features highlighted in the schematics in Fig. 3.5 b,d respectively. In addition

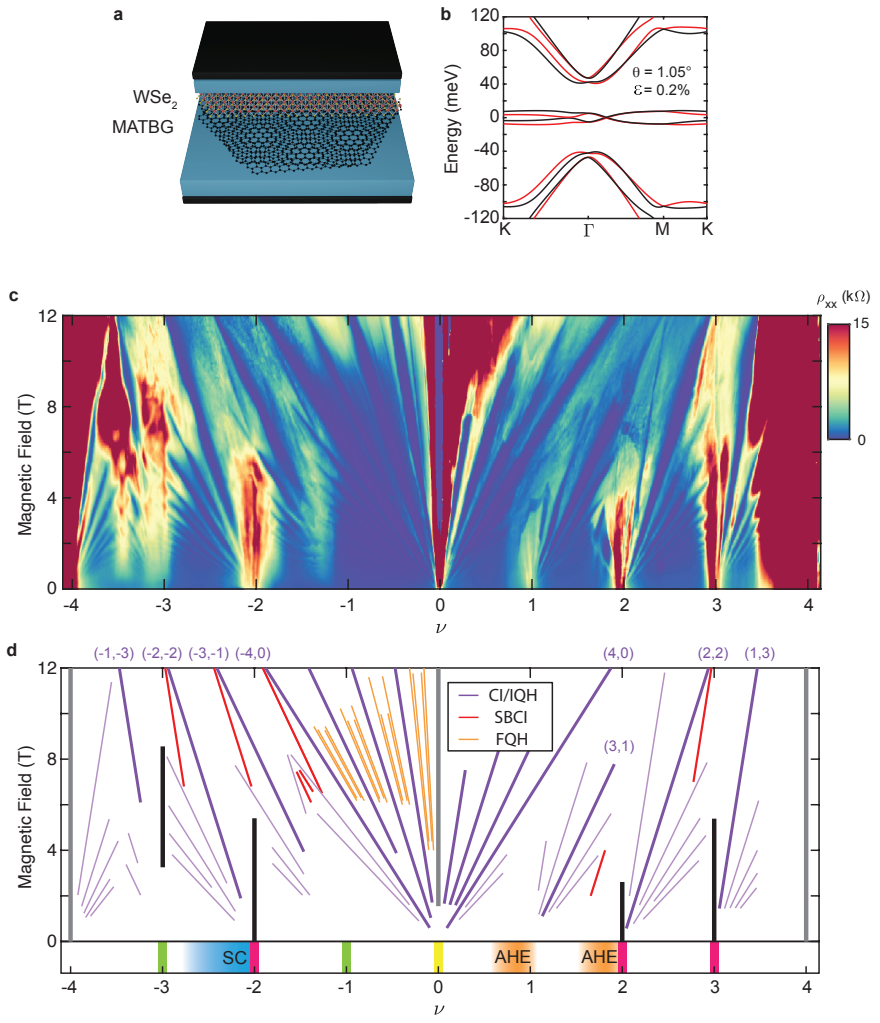

Figure 3.4: Landau fan digram of an ultraclean magic-angle twisted bilayer graphene. **a**, device structure. A magnic-angle twisted bilayer graphene is proximitized to a monolayer transition metal dichalcogenide WSe_2. **b**, calculated band structure that accounts for the strain effect and an angle closed to that is experimentally found. **c**, Landau fan diagram of resistivity ρ_{xx} measured up to 12T at $T = 300$ mK. **d**, The phase diagram of the $\theta = 1.03°$ MATBG/WSe_2 sample. At finite magnetic field, we denote Chern insulators and integer quantum Hall states with purple color, topological charge density waves (TCDWs) with red color, fractional quantum Hall states with yellow color, and the possible topologically trivial incommensurate Kekulé spiral (IKS) states with black color. At zero magnetic field, we denote the superconductivity phase space with blue color, and anomalous Hall effects with orange color.

to the conventional hierarchy of CCIs, the primary cascade of TCDW states follows the same sequence of Chern number $t = -1, -2, -3$ as the main CCIs, but with moiré filling index now at half integers $s = -5/2, -3/2, -1/2$ respectively. Figure 3.5e shows linecut of longitudinal resistivity ρ_{xx} and Hall conductivity σ_{yx}, calculated from tensor relation $\sigma_{yx} = \rho_{yx}/(\rho_{yx}^2+\rho_{xx}^2)$, at $\mu_0 H = 8.5$ T. At the base temperature, $(-2, -3/2)$ and $(-3, -1/2)$ TCDW states show fully suppressed ρ_{xx} and σ_{yx} close to quantization, while the $(-1, -5/2)$ TCDW remains dissipative. The three TCDW states together form a new cascade, with an equal interval of $\Delta t = -1$ and $\Delta s = 1$ in between, exactly as in the main sequence of CCIs but shifted by $s_0 = 1/2$. The TCDW cascade thus can be understood as the same type of charge density wave that doubles the unit cell area, occurring in different spin- valley-polarized magnetic subbands, specifically when filling the second, third and fourth copy of the $C = -1$ magnetic subbands below charge neutrality . Interestingly, such picture would predict an additional incompressible state at $(0, -7/2)$, which is simply a charge density wave with zero total Chern number, when filling the first copy of the C = -1 magnetic subband. Our observation of a gapped state at $\nu = -7/2$ at high magnetic field, from both high ρ_{xx} and sign reversal in ρ_{xy}, is consistent with this interpretation.

We find the three TCDW states share the same lower threshold magnetic field, at a simple rational flux ratio $\Phi/\Phi_0 = 1/4$. A second group of TCDW states, with topological invariants $(-3, -2/3)$ and $(-4, -1/3)$, are also found to be strongly tied with a simple rational flux ratio $\Phi/\Phi_0 = 1/3$. These two TCDW states are flanked by the $(-2, -1)$ CCI state and the $(-5, 0)$ IQH state, which spans a magnetic subband with Chern number $C = -3$ emanating from $\Phi/\Phi_0 = 1/3$ towards zero field (green shaded region). Here, the two TCDW states emerge sharply below the crossing point at $\Phi/\Phi_0 = 1/3$, which can be intuitively understood as partitioning the $C = -3$ band into three parts, each with $C = -1$ equally, forming a second cascade.

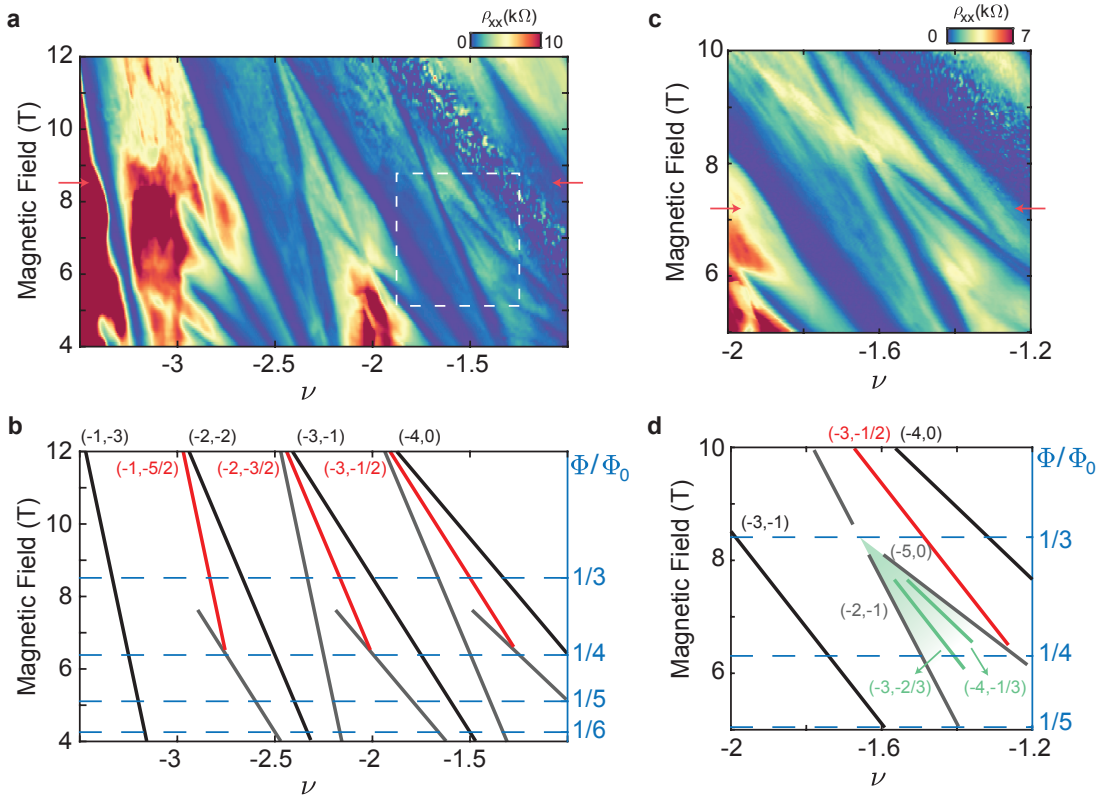

Figure 3.5: Cascades of topological charge density wave states.**a**, A zoom in measurement of the resistivity ρ_{xx}, focusing on the TCDWs with half integer band filling index s. **b**, Phase diagram of the first TCDW cascade (red lines), extracted from measurements in panel **a**. The main sequence of the CCI are also marked (black lines). The left y axis shows the corresponding magnetic flux ratio Φ/Φ_0. **c**, A zoom in measurement of the resistivity $\rho_x x$, focusing on the TCDWs with band filling index $s = -1/3$ and $-2/3$. The phase space is marked by the white dashed box in panel **a**. **d**, Phase diagram of the second TCDW cascade (green lines), extracted from measurements in panel **c**. The left y axis shows the corresponding magnetic flux ratio Φ/Φ_0.

Summary 3: Symmetry breaking Chern insulators in twisted graphene

1. A twist between two 2D materials can introduce quenched kinetic energy and large interaction energy scale, giving rise to many strongly correlated phenomenon.
2. In twisted bilayer graphene, a small magnetic field can give rise to strongly correlated Chern insulator with broken spin-valley flavour symmetry.
3. In clean samples, the translational symmetry will further be broken, which leads to the formation of integer Chern insulator at fractional fillings.

Chapter 4

FRACTIONAL CHERN INSULATORS IN TWISTED $MoTe_2$ SUPERLATTICE

The fractional Chern insulator (FCI) state is the zero magnetic field analog of the fractional quantum Hall state [34, 10, 35, 125]. They arise both because of strong correlation and the nontrivial topology of the band structure or Landau levels. The difference, however, lies in the fact that FCI is described by a lattice model in a system with spontaneous time-reversal symmetry breaking without Landau level formation [57, 58, 59, 60, 61, 62]. Previous studies have proposed that such an FCI can be realized in bandwidth-tuned Haldane models with short-range interactions [126], checkerboard lattices [57, 59, 61, 60], kagome lattices [58] and beyond [62].

Moiré superlattices of two-dimensional materials are emerging platforms due to their highly tunable flat electronic bands, topology, lattice geometry, and correlation effects. For instance, FCI states at magnetic fields as low as 5T have been observed in magic angle twisted bilayer graphene [127] or the Hofstadter band of bilayer graphene aligned with hBN in high magnetic fields [128]. Abundant correlated insulating states at fractionally filled moiré minibands have been realized in twisted transition metal dichalcogenides (TMDs). Quantum anomalous Hall (QAH) effect has also been realized in both graphene [106] and TMD moiré systems [107].

However, the experimental realization of FCI at zero magnetic field remains very challenging due to the stringent requirements of ferromagnetism, strong correlation, and topological bands in a single system. One possible route is to design a honeycomb lattice with strongly correlated topological bands, i.e., the Kane-Mele model with interaction. The exchange interaction can help to gap out the spin, leading to the realization of the Haldane model. Finally, electron correlation at short range can lead to the formation of an FCI. We will report how we use this route based on rhombohedral stacking (R-stacked) twisted

$MoTe_2$ to realize FCI at zero magnetic field that exhibits fractional quantum anomalous Hall effect (FQAHE).

4.1 Moiré transition metal dichalcogenide

A rhombohedral-stacked twisted TMD moiré bilayer can host topological flat bands with opposite Chern numbers in the two spin-valley sectors [129]. In real space, the moiré orbital consists of MX and XM sites, as shown in Fig. 4.1**a**. At a suitable twist angle, e.g., around 3.7° in the $tMoTe_2$ case, the two orbitals have nearly degenerate energy.

A useful picture to understand the origin of spin-valley Chern numbers is the skyrmion of layer pseudo-spins [129, 130]. Let's start with the R-stacked bilayer case without moiré potential. Because of the strong spin-orbital coupling of the constituent layers, the internal spin and valley degrees of freedom are locked. In the following, we will interchangeably use the spin or valley index, but they really mean the same thing in this system. Because of the lifted spin degree of freedom, the bilayer can be treated as a layer pseudospin two-band model at each valley.

$$\mathcal{H}_{K\uparrow}(\theta = 0) = \begin{pmatrix} -\frac{\hbar^2 k^2}{2m^*} + \Delta_b^0 & \Delta_T^0 \\ \Delta_T^{0\dagger} & -\frac{\hbar^2 k^2}{2m^*} + \Delta_t^0 \end{pmatrix} \tag{4.1}$$

where k is the momentum measured from the K point, m^* is the effective mass, ^{0} denotes the zero twist angle limit, and t and b denote the top and bottom layers. The potential term for each layer, $\Delta_{b,t}$, can be expressed as:

$$\Delta_{b,t}^0 = 2V \sum_{i=1,3,5} \cos\left(\mathbf{G_i} \cdot \mathbf{r}_0 + \pm\psi\right) \tag{4.2}$$

This potential term for each layer is constrained by the symmetry group of the lattice, where $\mathbf{r}_0$ is the interlayer distance, and $\mathbf{G_i}$ is the reciprocal lattice vector basis. The phenomenological terms V and $+\psi$ for the top layer, $-\psi$ for the bottom layer, capture the shape of the potential.

The interlayer tunneling term Δ_T has the same form as the twisted graphene case derived from the two-center approximation. Now using transition metal atoms $d_{x^2-y^2} + id_{xy}$ basis,

we have,

$$\Delta_T(\mathbf{r}) = \omega + \omega' \times e^{i\mathbf{G_2}\cdot\mathbf{r}} + \omega' \times e^{i\mathbf{G_3}\cdot\mathbf{r}} \tag{4.3}$$

where ω is the interlayer tunneling amplitude. ω' phonologically capture the strain effect that breaks C_{3z} symmetry perturbatively.

If we assume that the local stacking is adiabatically connected from the twisted case and intrinsic R-stacked bilayer, the effect of the moiré can be viewed as a magnetic field on the layer pseudospin. Choosing the coordinate system to have two layers rotating $\pm\theta/2$ respectively, we have:

$$\mathcal{H}_{K\uparrow}(\theta) = \begin{pmatrix} -\frac{\hbar^2(k-\kappa_+)^2}{2m^*} + \Delta_b & \Delta_T \\ \Delta_T^\dagger & -\frac{\hbar^2(k-\kappa_-))^2}{2m^*} + \Delta_t \end{pmatrix} = h_0(k) + \vec{h}_{\text{eff}} \cdot \vec{\sigma} \tag{4.4}$$

where $h_0(k) = \begin{pmatrix} -\frac{\hbar^2(k-\kappa_+)^2}{2m^*} & 0 \\ 0 & -\frac{\hbar^2(k-\kappa_-))^2}{2m^*} \end{pmatrix}$ and $\vec{\sigma} = (\sigma_x, \sigma_y, \sigma_z)$ being Pauli matrix in the layer pesudospin subspace. The Fourier transformed Hamiltonian in the moiré reciprocal space has the similar form as we derived above for twisted bilayer graphene, despite extra coupling due to effective inversion symmetry breaking in the moiré scale.

It can be seen from this form of the Hamiltonian that the on-site effect of the moiré is a constant energy and a Zeeman-like effect to layer pseudospin. When transit from different local stacking, the moiré potential serves as an effective magnetic field h_{eff}, i.e., Skyrmion lattice as shwon in Fig.4.1 **b** that gives rise to layer pseudospin texture.

When the momentum dependent Zeeman-like term is quenched, i.e., $\frac{\hbar^2|\kappa|^2}{m^*}/|\vec{h}_{\text{eff}}| \ll 1$, we have an explicit winding number expression, the Brouwer degree :

$$\deg \vec{h}_{\text{eff}} = \frac{1}{4\pi}\int \mathcal{B}_{\text{eff}} = \frac{1}{4\pi}\int \frac{\vec{h}_{\text{eff}} \cdot \partial_x \vec{h}_{\text{eff}} \times \partial_y \vec{h}_{\text{eff}}}{|h|^3} dxdy \tag{4.5}$$

This is the microscopic origin of Chern number when the system is away from topological phase transition where the gap size is comparable to the momentum dependent Zeeman-like term. In other word, the $\deg \vec{h}_{\text{eff}}$ is not necessarily identical to Chern number but it provides a starting point when $\frac{\hbar^2|\kappa|^2}{m^*}/|\vec{h}_{\text{eff}}| \ll 1$. It is naturally to argue this will be possibly the case for moiré system because the small energy scale of $|\kappa|^2$ and large effective mass.

We now turn to deal with electric field, which is usually the control knob that a dual gated device geometry provides. In charge neutrality, the electric field creates imbalance

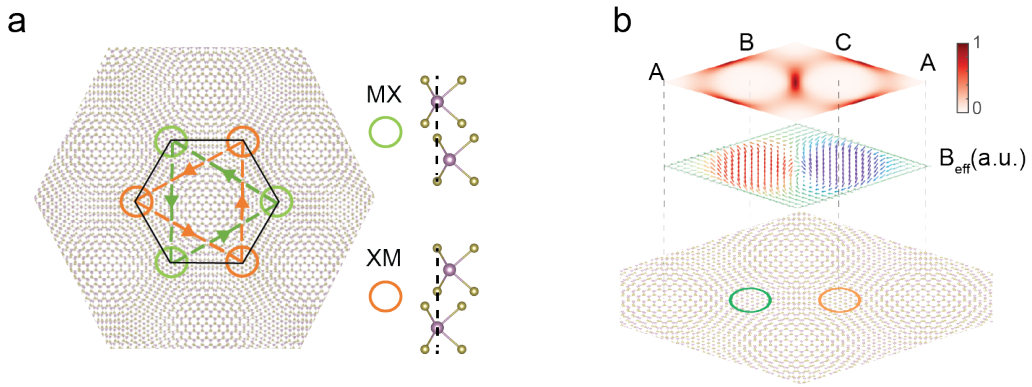

Figure 4.1: Real space lattice and skyrmion lattice of twisted $MoTe_2$. **a**, R-stacked homobilayer hosting two degenerate energy minima at high symmetry MX and XM points, forming a honeycomb moiré superlattice. Complex hopping between next-nearest-neighbour sites realizes the Haldane model.**b** Skyrmion lattice or effective magnetic field in the real space. Top panel: amplitude of the effective magnetic field h_{eff}. Middle panel: vector field of the layer pseudo spin texture.

population of carriers that localizes in top and bottom layer. Thus, the electric field is simply a Zeeman term (as the role of magnetic field) in the skyrmion lattice. So we have:

$$\mathcal{H}_{K\uparrow}(\theta, D) = h_0 + \vec{h}_{\text{eff}} \cdot \vec{\sigma} + D\sigma_3 \tag{4.6}$$

where D is monotonic to the strength of electric field decided by dual gated experiment.

4.2 Emergent ferromagnetism

Figure 4.2a shows the photoluminescence (PL) intensity plot versus n and photon energy. All data in this section are taken at a temperature of about 1.6 K, unless otherwise specified. For doping-dependent measurements, we focus on the hole-doping side as the electron side is found to be non-ferromagnetic and topologically trivial. First, we maintain the electric field to be zero. The first glance of the PL data is that the twisted bilayer $MoTe_2$ is strong as hundreds of counter per μW per second. This is due to the unusual direct bandgap nature

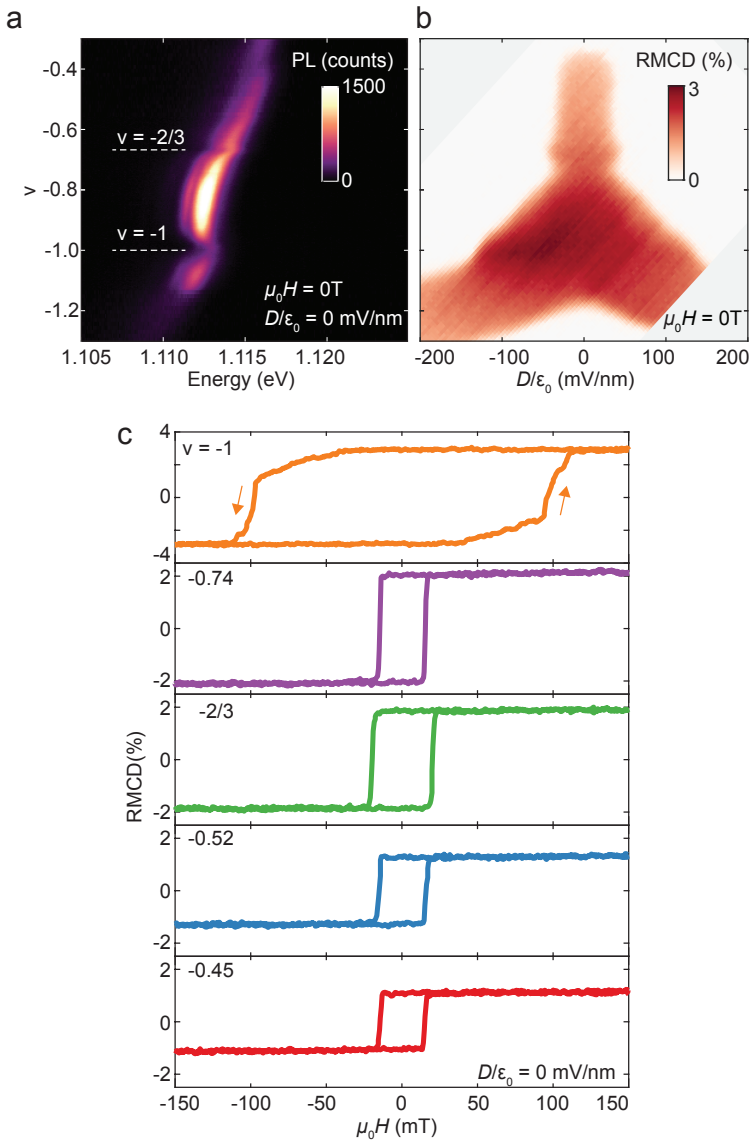

Figure 4.2: Electrically tunable correlated ferromagnetic states in twisted bilayer $MoTe_2$. **a**, PL intensity plot as a function of hole doping and photon energy. Filling factors v corresponding to the formation of correlated insulating states are indicated. **b**, RMCD signal versus v and perpendicular electric field D at zero magnetic field $\mu_0 H = 0$. The phase space with non-vanishing signal corresponds to the ferromagnetic state. **c**, RMCD signal versus $\mu_0 H$ swept back and forth at selected fillings.

of this twisted $MoTe_2$. At $\nu = -1$ and $\nu = -2/3$, the PL intensity drops while the peak blueshifts. A weak feature at $\nu = -3/5$ is also observed under a magnetic field of about 1 T. This PL resonance arises from the trion (that is, charged exciton). The observed reduction in PL intensity is a result of reduced trion population, as the formation of correlated insulating states depletes the holes available for trion formation, as we will discuss in detail later.

We use reflective magnetic circular dichroism (RMCD) measurements to investigate the magnetic response. Figure 4.2b shows the zero-magnetic-field RMCD signal intensity plot as a function of v and D. A non-vanishing RMCD signal highlights the phase space of the ferromagnetic states. Interestingly, the data show that the critical electric field Dc for suppressing the ferromagnetic state is enhanced at the fractionally filled insulating state $\nu = -2/3$. Figure 4.2c shows the hysteresis of the RMCD signal versus applied magnetic field, $\mu_0 H$, at selected ν, where μ_0 denotes the vacuum magnetic permeability. Sharp spin-flip transitions at the coercive field, $\mu_0 H_C$, are observed.

The dependence of $\mu_0 H_C$ on the correlated insulating states is further highlighted by doping-dependent measurements of the

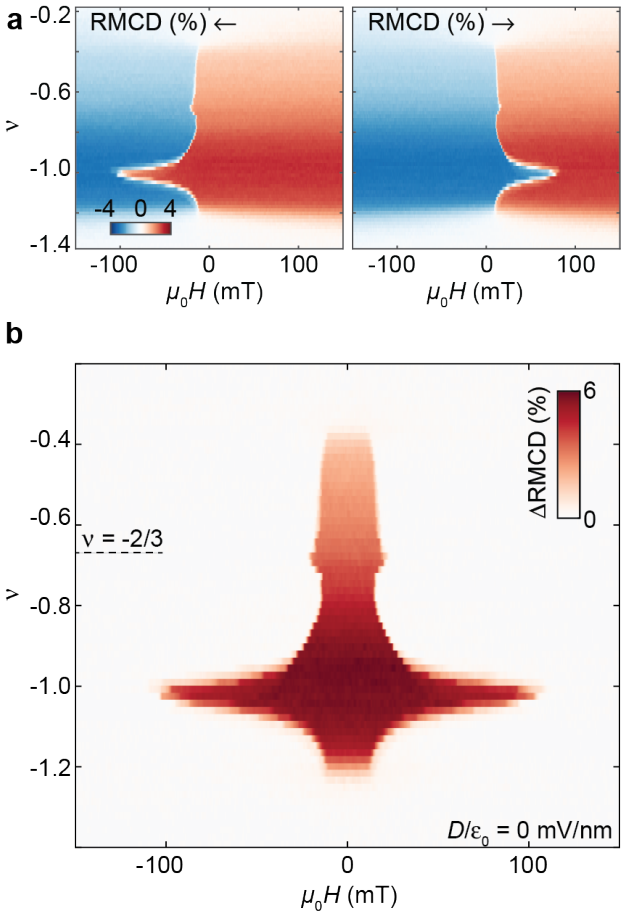

Figure 4.3: Fractionally filled correlated ferromagnetic insulating states. **a**, RMCD signal intensity plot versus filling factor ν and magnetic field swept down (left) and up (right). **b**, Difference of RMCD sweeps in a, ΔRMCD, versus ν and $\mu_0 H$. Clear enhancement of $\mu_0 H_C$ at $\nu = -1$ and $\nu = -2/3$ is observed.

RMCD hysteresis loop. Figure 4.3a shows the RMCD intensity plots versus ν and $\mu_0 H_C$ swept down (left) and up (right). The difference between the sweeps is indicated in 4.3b. The data show that $\mu_0 H_C$ is enhanced near the correlated insulating states. As hole doping increases from charge neutrality, $\mu_0 H_C$ first increases from about 10 mT to about 20 mT near the $\nu = -2/3$ insulating state, then reduces slightly, and subsequently increases markedly up to about 100 mT near $\nu = -1$ before finally reducing until the ferromagnetic state vanishes. Figure 4.4 is a high-resolution plot of the RMCD hysteresis around the fractional filling features. In addition to the robust $\nu = -2/3$ state, a weak and spatially dependent feature exists near $\nu = -3/4$ filling in $\mu_0 H_C$. As doping is decreasing, the overall trend of zero field RMCD is decreasing.

As an additional probe of the strength of the ferromagnetic states, we perform temperature-dependent RMCD measurements versus filling. First, we take a look at two specific filling $\nu = -1$ and $\nu = -2/3$, as shown in Fig.4.5. The magnetic hysteresis is weaken as approaching T_C and finally hysteresis disappears above T_C. For $\nu = -1$, the domain-like jump near magnetic reversal at about 100 mT is also weaken. Interestingly, despite at the same beam spot, the $\nu = -2/3$ state has different discrete jump, i.e., the mangetic Barhausen effect shows doping dependence. This suggests that This magnetic Barkhausen effect can come from domains due to moiré level disorder. T_C also has a strong filling dependence, peaking at $\nu = -2/3$ and $\nu = -1$ where correlated insulating states form, with a T_C of about 4.5 K and about 14 K, respectively. This T_C is relatively high considering the large moiré unit cell of period of

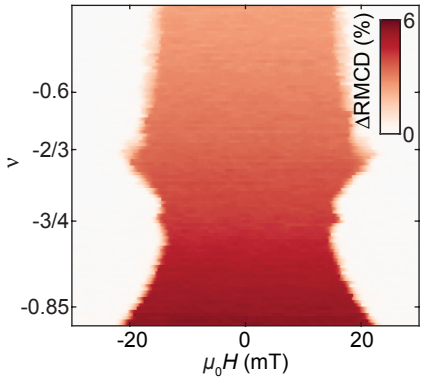

Figure 4.4: High-resolution plot of ΔRMCD, versus ν and $\mu_0 H$. In addition to the $-2/3$ feature, another feature near $-3/4$ filling is observed.

about 5.4 nm and the correspondingly low spin density compared with conventional two-dimensional magnets.

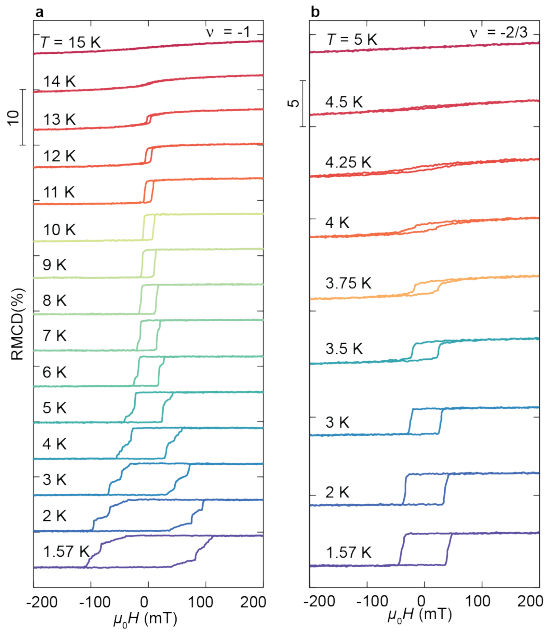

Figure 4.5: Temperature-dependent RMCD at $\nu = -2/3$ and $\nu = -1$.**a**, $\nu = -1$. The Curie temperature T_C is about $14K$.**b**, $\nu = -2/3$. The Curie temperature T_C is about $4.5K$.

We now exam temperature dependent RMCD near $\nu = -2.3$.The fractionally filled state $\nu = -2/3$ has enhanced T_C compared to nearly by state with arbitrary filling. This can be shown by extracting coercive field $\mu_0 H_C$ and Curie temperature T_C versus ν are shown in Fig.4.6. The T_C of $\nu = -2/3$ reaches 4 K but the state with $0.7 < \nu < 0.75$ is lower than 4 K. Notably, an incipient $v = -3/4$ state appears in ν dependent coercivity but not in T_C. As we will show later, this $\nu = -2/3$ is a zero-field FCI state. The enhancement of magnetic order in FCI state can be theoretically interesting. Recent theory suggests that the FCI state enhances magnetic order (increases magnon gap) by increasing anisotropy.

Because the sublattice orbitals of the honeycomb lattice are localized in opposite layers of the twisted bilayer, the application of a perpendicular electric field breaks the layer degeneracy. This enables tuning of the superlattice from a honeycomb to a triangular lattice dominated by kinetic antiferromagnetic exchange interactions, as shown in Fig.4.7**a** insert. As electric field $|D/\epsilon_0|$ increases from 0 to 250 mV/nm, the RMCD decreases and vanishes after critical electric field $|D_C/\epsilon_0| \approx -120$ mV/nm. The systematic investigation suggests that this transition is likely second order or weakly first order[84], while very recent local magnetization measurement suggests a first order transition[131]. It's likely that sample inhomogeneity can make it difficult to conclude the order of this electric field driven phase transition. We

examine the magnetic phase diagram of the system as a function of filling, electric field and temperature. Figure 4.7**b** shows the ν- and D-dependent RMCD at 3.5 K. Although the magnetic states away from $v = -2/3$ soften substantially compared with their behaviour at 1.6 K, the $v = -2/3$ state remains a hard magnet with $\mu_0 H_C$. This is consistent with the measurement shown in in Fig.4.6. This further supports the view that the correlated insulating state at $v = -2/3$ thermodynamically stabilizes ferromagnetism.

Fig.4.7**c** shows the temperature- and D-dependent RMCD signal of the $v = -2/3$ state at zero magnetic field. The D-field range of the ferromagnetic state decreases as temperature increases, vanishing above a T_C of about 4.5 K.

Recently, many imaging techniques show that these magnetic phase transition in two dimension can accompany the formation of novel magnetic texture or intersting new quasiparticles. If we treat RMCD as an approximate order parameter, the phase diagram reconstructed from fig.4.7**c** is illustrated in 4.7**d**. This typical dome-like phase diagram suggeststst that detecting universality in this moiré magnetic by optics can be interesting. Both temperature and electric field destroy the ferromagnetic states, highlighting the tunability of twisted $MoTe_2$ bilayer.

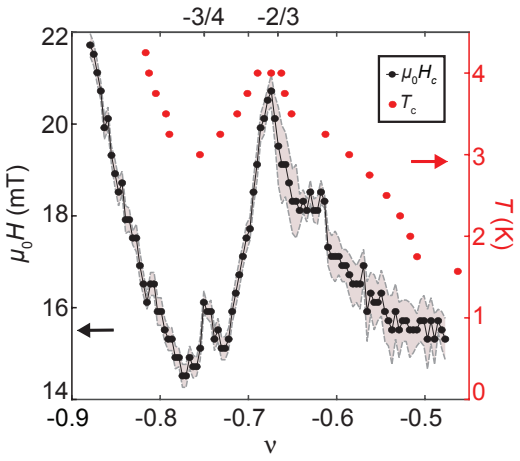

Figure 4.6: $\mu_0 H_C$ (left axis) and T_C (right axis) versus ν. Enhancement of both $\mu_0 H_C$ and T_C is apparent near –2/3 filling. The value $\mu_0 H_C$ was extracted by change point detection. The shaded area denotes the extracted transition width. The extracted TC has an uncertainty of 0.25 K, determined by the temperature step size of the measurement.

4.3 Optical detection of fractional Chern insulators

We now proceed to investigate topological properties of $tMoTe_2$ by optical spectroscopy.

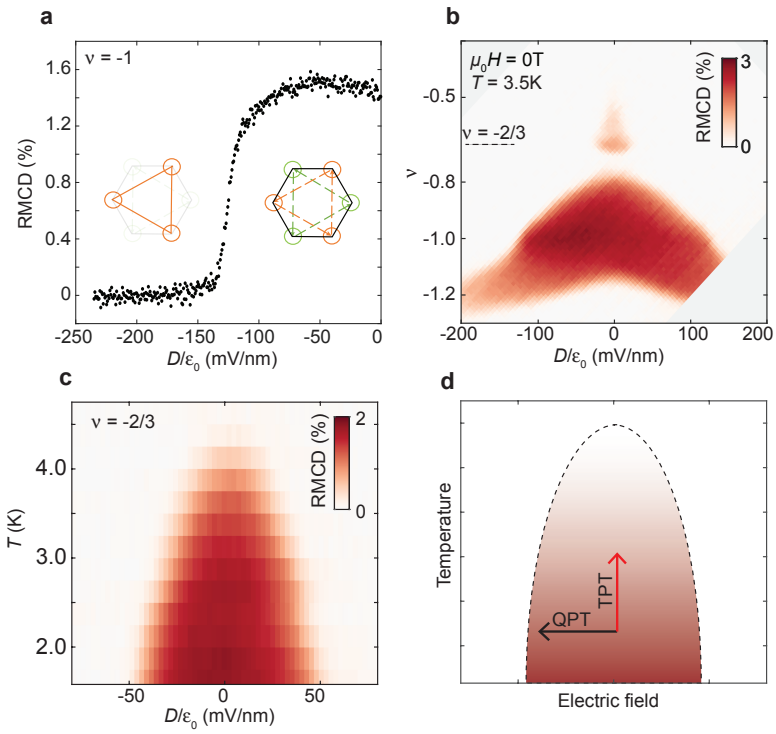

Figure 4.7: **a**, Zero-magnetic field RMCD signal at $\nu = -1$ versus electric field, demonstrating an electric-field-driven magnetic phase transition concurrent with the change in superlattice geometry from honeycomb to triangular (insets). **b**, RMCD signal intensity plot versus ν and D at $T = 3.5$ K. **c**, RMCD signal versus temperature and D at $\nu = -2/3$, highlighting the ferromagnetic phase diagram.**d**, illustration of the temperature driven phase transition and quantum phase transition. The quantum phase transition is also a topological phase transition from a Chern insulator to a trivial magnetic insulator or non-ferromagnetic insulator, which will be investigated soon.

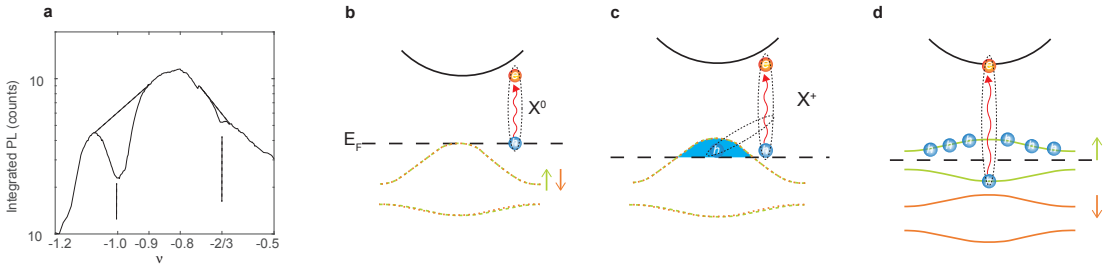

Figure 4.8: Trion sensing of correlated states in twisted $MoTe_2$. and illustration of exciton and trion formation. **a**, Integrated PL as a function of ν. Trion emission is suppressed and deviated from the parabolic trend when this is a correlated state forming. **b**, Optically injected exciton formation in undoped sample. **c**, Upon finite hole doping, excitons bind to free carriers, forming positively charged trions. **d**, At integer or fractional fillings where correlated insulating states form, doped holes are consumed and the system is gapped, thus reducing trion population.

As we show before, the PL spectrum shows a suppression at integer or fractional filling. This can be seen clearly in Fig. 4.8 where we integrate the PL emission about 1 meV around the peak. We found that integration around certain emission peak enhances the signal to noise ratio. This is probably due to dark counts of infrared detector over a broad wavelength.

The neutral exciton, X^0, forms at 1.132 eV upon optical excitation when near charge neutrality, as shown in Fig.4.8b. As hole doping increases, the neutral exciton binds to the free carriers to form charged trions (X^+, Fig.4.8b). The trion has lower emission energy and dominates the photoluminescence spectra. The trion peak is redshifted with respect to X^0 due to this binding energy. However, when the doped hole density reaches an integer ($\nu = -1$, Fig.4.8c) or fractional ($\nu = -2/3$, $\nu = -3/5$) filling of the moiré unit cell, correlated insulating states form, consuming doped holes and gapping the Fermi surface. In this scenario, the trion population is drastically reduced, and thus the PL intensity decreases. Note that the correlation induced gap is small, so the PL is still dominated by

trion. The intensity of trion then can sense the formation of a gapped state.

We then plot integrated PL intensity as a function of magnetic field and carrier density in Fig. 4.9 (that is, the optically detected Landau fan diagram). We observe that the $\nu = -1$ and $\nu = -2/3$ states show linear dispersions that persist down to zero magnetic field. In addition, there is a weak dispersive feature at $\nu = -3/5$. This feature becomes appreciable as $\mu_0 H$ increases above 1 T at this twist angle, but persists down to zero magnetic field at a spot with a twist angle of about 3.57°(For detail, see the full publication [85] and its supplementary figures). These observations differ from the topologically trivial correlated insulating states at the electron-doping side (Fig. 4.10), which are non-dispersive. This result aligns with our expectations, as these electron-doped states are not ferromagnetic—a necessary condition for the formation of both integer and fractional QAH states.

To quantatatively extra the Chern number, first, using the doping density given by hBN capacitance ($C_g = \epsilon_{\mathrm{hBN}}/d$, $\epsilon_{\mathrm{hBN}} = 3.0$) and assuming the filling to be linear in carrier density, the Landau fan diagram from the PL measurement can be reproduced. The hBN thickness is measured using an atomic force microscope with an uncertainty of about 200 pm, which is negligible compared with the 20–40 nm hBN. The most significant uncertainty comes from the dielectric constant of hBN (widely accepted as 3–3.3). Second, single-gated reflectance measurements are performed to obtain the capacitance ratio of the top and bottom gates, which matches the thickness ratio obtained by atomic force microscopy measurements. To quantitatively compare the opti-

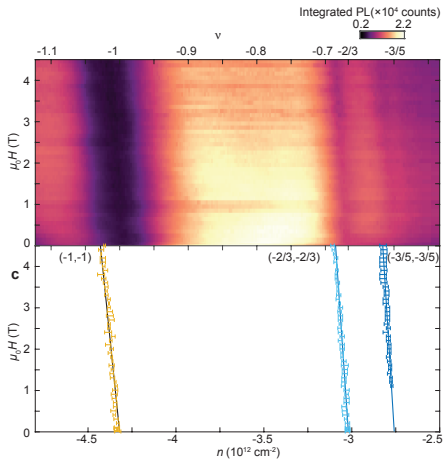

Figure 4.9: Evidence of integer and fractional QAH states. Top panel, Wannier diagram corresponding to a $C = -1$ FCI at $\nu = -1$ (black line), a $C = -2/3$ FCI state at $\nu = -2/3$ and a $C = -3/5$ FCI state at $\nu = -3/5$ (blue lines), with C equal to the Hall conductance in the units of e^2/h. States are marked by (C, ν). Overlaid data and error bars are the extracted carrier densities of the three insulating states.

cal fan diagram with the Streda formula dispersion, we extract the centroid of the integrated PL minimum as a function of carrier density for each value of the applied magnetic field. The centroid is obtained by calculating the geometric centre for the local minimum of the PL intensity. The error bar indicates a 5% deviation of the centroid PL intensity. Using the slope extracted from the Landau fan diagram, the capacitance of the gates can be obtained and compared with the hBN capacitance. This method cross-checks the validity of the hBN capacitance value.

Figure.4.9 bottom panel is the Wannier diagram with solid lines indicating dispersion curves determined by the Streda formula, overlaid with the carrier densities extracted from integrated PL in 4.9 top panel, which correspond to the integer and fractionally filled states. We find that Streda dispersions with $C = -1$ (black line), $C = -2/3$ and $C = -3/5$ (blue lines) match well with the $n - \mu_0 H$ dependence of the three states at $v = -1$, $v = -2/3$ and $v = -3/5$, respectively. Linear fitting of the extracted densities in Fig. 4.9 bottom panel yields the extracted Chern numbers of the three states as $C = -0.95(7)$, $C = -0.63(4)$ and $C = 0.59(4)$, consistent with the expected Streda formula dispersion.

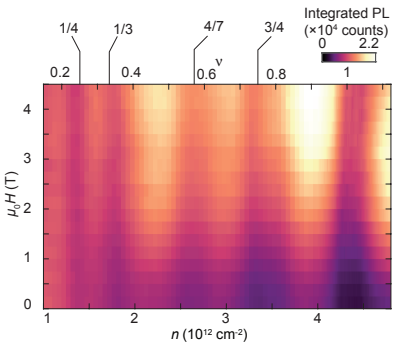

Figure 4.10: Fan diagram for the electron doping side. No dispersion is observed for any of the correlated insulating states, implying that the lowest moiré conduction band is topologically trivial.

The observed $C = -1$ state supports the assignment of the $\nu = -1$ ferromagnetic insulating state as a QAH state (or a topological Mott insulator[108, 132]). This observation is consistent with recent predictions from the Haldane–Hubbard model[133, 134, 135] with a Chern number of –1. Most notably, the ferromagnetic insulating states with $C = -2/3$ and $C = -3/5$ at fractional fillings of the flat Chern band are identified as fractional Chern insulator states that survive to zero magnetic field, that is, zero field FCI states. These two states are the zero-field analogue of the fractional quan-

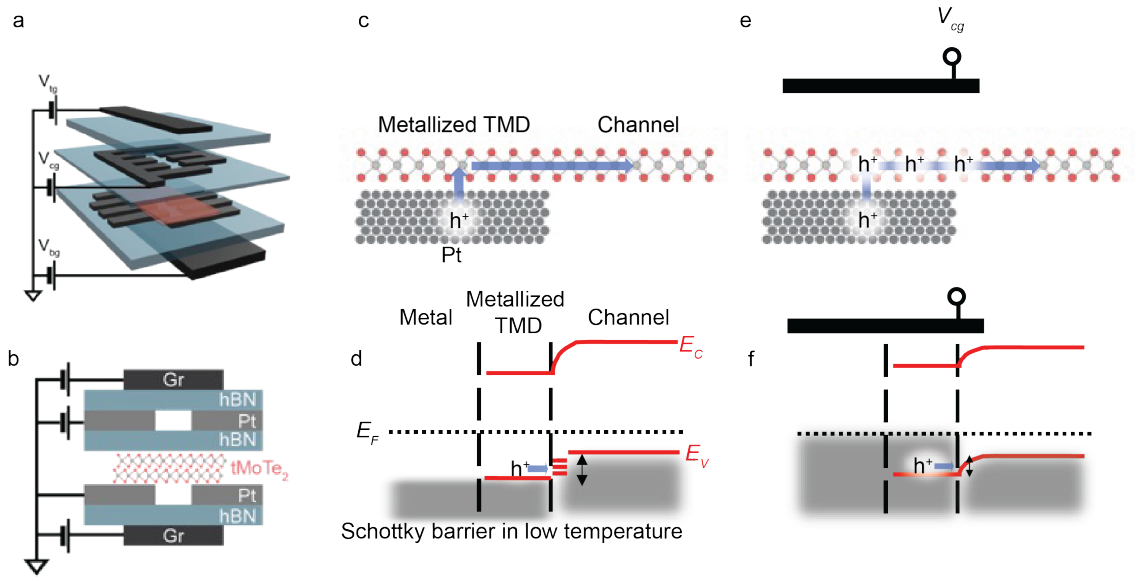

Figure 4.11: Triple gates design to improve metal TMD contact. **a**, illustration of the device structure. In addition to standard dual gate design, we introduce another local gate that only dopes the contact regime. **b**, section of the device shown in **a**. **c**, illustration of metal-TMD interface. **d**, possible Fermi surface alignment in metal-TMD interface. Because of the precense of defects possibly due to fabrication, the interface has discrete 0D channel that creates Schottky barrier in low temperature. **e**, illustration of metal-TMD interface with an additional contact gate. **f**, a proposed understanding that the contact gate smears the discrete 0D channel by heavily doped the defective channels.

tum Hall state sequence of odd denominators, hosting fractional charge excitations[136] and Abelian topological orders without Landau-level formation.

4.4 Observation of fractional quantum anomalous Hall effect

In last section, $tMoTe_2$ has been identified as a FCI using optical sensing technique. Although the Streda formula approach, detection of magnetism via RMCD and the expected behavior with electric field, magnetic field and temperature are strong signautre of FCI, the fractional quantum anomalous Hall effect, by definition, is supposed to present in transport

measurement.

4.4.1 Contact scheme

In this section, we will report device architecture as shown in Fig.4.11 a-b, called triple gate design. Compared to standard double gate design widely used in other TMD transport works, an additional contact gate is added to improve the contact resistance. Historically, the main difficulty in twisted two-dimensional semiconductor transport studies has been achieving low contact resistance at zero perpendicular electric field[137, 138]. Additional contact gate can lower the contact resistance by heavily hole-doping the contact region to a carrier density of about 10^{13} cm^{-2}.

The fabrication is based on dry transfer, but modified to include several AFM-based bubble squeegue[139]. hBN, 2H-MoTe2 and graphite crystals were mechanically exfoliated onto p-doped Si/SiO_2 substrates to obtain nm-thick flakes. An optical microscope was used to find hBN for top, bottom and contact gate dielectrics and thin graphite for gate electrodes. The cleanliness of the flakes was confirmed by AFM or contrast-enhanced optical microscopy. The bottom gate heterostructure was fabricated by a standard polycarbonate-based dry transfer process. First, an hBN flake was chosen to serve as a bottom gate dielectric and picked up, followed by a graphite bottom gate electrode, before putting down the structure on a silicon substrate. Standard e-beam lithography was used to define Hall bar contacts, and Pt (8 nm) electrodes were deposited by e-beam evaporation. The bottom gate structure was cleaned using contact-mode AFM, and then moved into a glovebox with O_2 and H_2O levels less than 0.1 ppm. In the glovebox, $MoTe_2$ was exfoliated to find a monolayer flake that was cut using an AFM tip. A twisted $MoTe_2$ stack was formed by picking up an hBN flake, picking up part of the $MoTe_2$ monolayer, rotating the stage by a desired angle and then picking up the remaining part of the $MoTe_2$ monolayer. The twisted $MoTe_2$ structure was put down onto the prepared bottom gate. The stamp polymer was washed off with molecular sieve-cleaned anhydrous chloroform and dichloromethane in a glovebox environment. After finishing the encapsulation and wash-off process, the twisted $MoTe_2$ device was removed from the glovebox and cleaned using contact-mode AFM. Local contact

gates, used to improve contact resistance, were added using standard e-beam lithography and evaporation of Pt (8 nm). An additional step of lithography and evaporation of Cr/Au (5/70 nm) was performed to connect the electrodes and conductive pads to enable wire bonding to the sample. After lithography, another round of AFM cleaning was performed on the entire structure before the subsequent transfer. The structure was finished by adding a graphite/hBN top gate. Polymer from this transfer was washed off with chloroform in ambient conditions.

We first briefly introduce high work function metal contact scheme (such as platinum Pt), as shown in Fig.4.11 c-d. Fig.4.11 c shows that when intrinsic TMD is in contact with Pt, the charge transfer process between high work function metal and TMD will heavily dope TMD, referred as Metallized TMD. This metallic interface will then be connencted to the channel. Idealy, the channel will have ohmic contact with the metallized TMD as long as channel is moderately doped. However, the real world case is far from ideal. Although a bare Pt works in ambient temperature with moderate gating, a very high top gate is needed to turn on the contact. Backgate can only be used to tune the channel. This creates an inevitable asymmetry in device design. We first want to understand that why ohmic contact is formed only when the metallized TMD and channel are heavily doped. We proposed that fabrication can bring strain or disorder near the Pt, or simply chemical instability (e.g., Pt difussion) has lead to contamination between the metallized TMD and channel. This leads to confined 0-D channel as shown in Fig.4.11 d. We note that the experimental validation of this proposal requires microscopic access of the electronic properties spatially close to Pt. Introducing the contact gate is a way to improve contact. First, the contact gate made by metal is not sharp. The stray electric field from contact gate may create a gradient of doping level. Second, the heavily doped metallized TMD and channel interface has quenched the 0-D chennel and make the originally insulating defects conductive enough, as shown in Fig.4.11 e-f. Again, such picture requires microscopic evidence and here is just one of the theory. Such picture is also in accordance with experiences using $RuCl_3$ charge transfer contact which sometimes also needs a contact gate[140], and $TaSe_2$ van der Waals metal contact[141].

4.4.2 Transport phase diagram of twisted $MoTe_2$

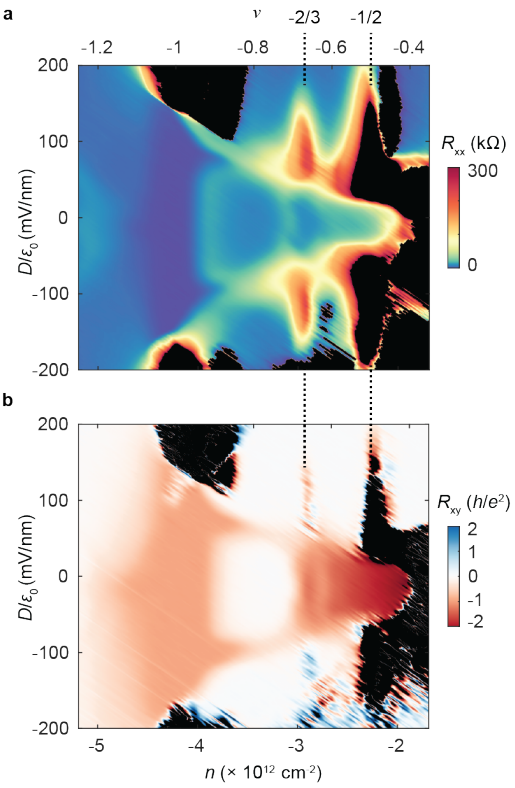

Figure 4.12: Phase diagram of quantized anomalous Hall states in $tMoTe_2$. Longitudinal (R_{xx}) resistance (**a**) and Hall (R_{xy}) resistance (**b**) as a function of electric field (D/ϵ_0) and carrier density (n) at 100 mK. The filling factor (ν) is shown on the top axis. R_{xx} and R_{xy} are obtained using the contact scheme as shown in Fig. 4.11. R_{xx} and R_{xy} are symmetrized and anti-symmetrized at a small magnetic field $|\mu_0 H| = 200$ mT, respectively.

We now start to explore the transport phase diagram of $tMoTe_2$. Figure 4.12 shows the maps of R_{xx} and R_{xy} for a device with twist angle about 3.7° (D(3.7°)) versus doping n and perpendicular electric field D/ϵ_0 at temperature $T = 100$ mK (See appendix for temperature calibration). R_{xx} is symmetrized and R_{xy} is anti-symmetrized with respect to a small applied out-of-plane magnetic field ($\mu_0 H$) of ±200 mT. The field serves to stabilize the polarization of the ferromagnetic states when sweeping gates. Insulating behaviour, with $R > 1$ MΩ, is shown in black. Several intriguing gate-tunable features can be seen in these maps that call for theoretical investigation. Here we focus on the regions centred around $\nu = -1$, –2/3 and –1/2 and D/ϵ_0, in which R_{xx} is small and $|R_{xy}|$ is very large, indicating the emergence of topologically nontrivial states.

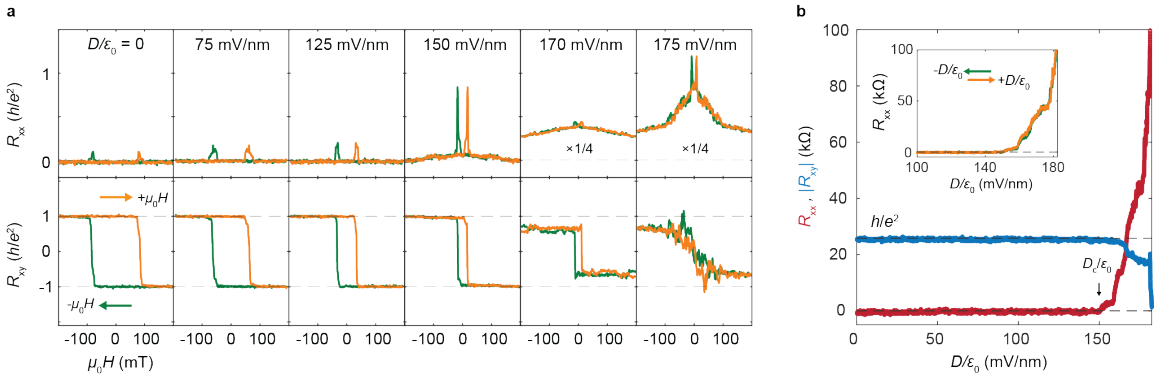

Figure 4.13: Electrically tunable integer FCI at $\nu = -1$. **a**, Magnetic-field-dependent R_{xx} and R_{xy} at selected electric fields D/ϵ_0 at $T = 100$ mK. Quantized R_{xy} and vanishing R_{xx} at zero magnetic field, as can be observed for D/ϵ_0, demonstrate the QAH effect. **b**, $|R_{xy}|$ (blue) and R_{xx} (red) as a function of D/ϵ_0. R_{xx} and R_{xy} are symmetrized and anti-symmetrized at $|\mu_0 H| = 200$ mT, respectively. Inset, R_{xx} versus electric field D/ϵ_0 swept up and down near the phase transition.

4.4.3 Integer Chern insulator and QAH

Figure 4.13a shows the $\mu_0 H$ dependence of R_{xx} and R_{xy} at $\nu = -1$ for selected values of D/ϵ_0 at $T = 100$ mK. At D/ϵ_0, R_{xy} exhibits a hysteresis loop with quantized values $\pm h/e^2(0.9998 \pm 0.0136 \times h/e^2)$ at $\mu_0 H = 0$ and coercive field $\mu_0 H_C \approx 84$ mT. Correspondingly, R_{xx} nearly vanishes at $\mu_0 H_C \approx 0$ mT and shows peaks of height around $0.3h/e^2$ when R_{xy} jumps between the quantized values. This is the hallmark of the QAH effect. The QAH state remains robust as the electric field increases and diminishes as D/ϵ_0 rises above a critical value of D_C/ϵ_0. The exact value of D_C/ϵ_0 depends on the twist angle.

To demonstrate this electric field effect, Fig. 4.13b shows anti-symmetrized R_{xy} and symmetrized R_{xx} versus D/ϵ_0 at $|\mu_0 H| = 200$ mT. At $D/\epsilon_0 \approx 150$ mV $\cdot$ nm^{-1}, R_{xy} begins to fall and R_{xx} starts to rise. By $D/\epsilon_0 \approx 180$ mV $\cdot$ nm^{-1}, Rxy has fallen to nearly zero and Rxx exceeds 100 kΩ. This behaviour implies an electric-field-induced phase transition

from a QAH to a trivial insulating state. In our measurement, this phase transition seems to be continuous, judging by the absence of hysteresis in R_{xx} when the electric field is cycled through the critical value. But this can be limited by the domain or disorder effect. Similar phenomena were observed in another device, where combined reflective magnetic circular dichroism and transport measurements show that this topologically trivial insulating state remains ferromagnetic. This finding is corroborated by the Hartree–Fock calculations performed as a function of electric field in recent theoretical works[136].

4.4.4 Fractional Chern insulator and FQAH

We now turn to the FCI states. Figure 4.14a shows the $\mu_0 H$ dependence of R_{xx} and R_{xy} at $\nu = -2/3$, with $T = 500$ mK and $D/\epsilon_0 = 0$. R_{xy} exhibits a hysteresis loop, with coercive field $|\mu_0 H_C| \approx 20$ mT, between levels at $\pm 3h/2e^2$ within 1% accuracy. Meanwhile, R_{xx} remains below 1 kΩ except for small bumps when R_{xy} switches between the two quantized values. These results confirm that the system at $\nu = -2/3$ is in an FCI state with Chern number $C = -2/3$. Figure 3b shows similar behaviour at $\nu = -3/5$, in which R_{xy} exhibits a hysteresis loop between levels at $\pm 5h/3e^2$ within 3% accuracy and R_{xx} again is small, confirming the observation of FQAHE with $C = -3/5$. Similar to the $C = -1$ Chern insulator state, the FCIs are electrically tunable. For simplicity, we focus on the –2/3 FCI state. Figure 4.14c shows the extracted anti-symmetrized R_{xy} and symmetrized R_{xx} at $|\mu_0 H| \approx 50$ mT as a continuous function of D/ϵ_0 at $T = 100$ mK. R_{xy} starts to decrease above $|D_C/\epsilon_0| \approx 20$ mV $\cdot$ nm^{-1} and eventually disappears into noise as $|D_C/\epsilon_0|$ rises above 80 mV$\cdot$nm^{-1}. Correspondingly, R_{xx} starts to rise from zero at about 50 mV$\cdot$nm^{-1}, reaches a peak in the range of 100–200kΩ roughly where R_{xy} disappears, and then drops to 20–30kΩ as D/ϵ_0 further increases to about 150 mV $\cdot$ nm^{-1}. This behaviour indicates an electric-field-induced phase transition from an FCI to a topologically trivial resistive state, and eventually to a metallic state. This phase transition can also be observed in Fig. **??**. Very recent microwave impedance microscopy reveals that this phase transition is FCI, to an intermediate metallic state, to a bulk insulating correlated insulator, finally to a metal at high D/ϵ_0[142]. Further theoretical and experimental efforts are needed to understand the

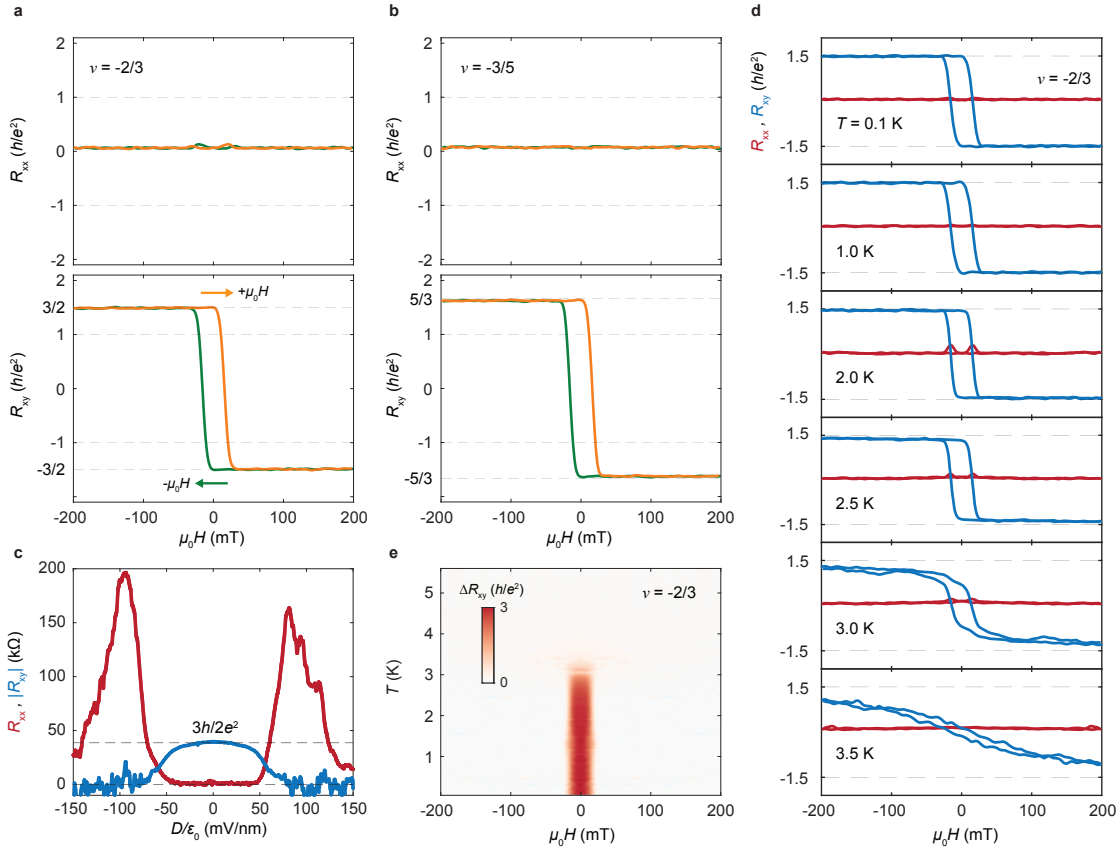

Figure 4.14: FQAH effect. **a**,**b**, R_{xx} and R_{xy} versus magnetic field $\mu_0 H$ at $\nu = -2/3$ (a) and $\nu = -3/5$ (b), with $T = 500$ mK and $D/\epsilon_0 = 0$. The data in panels c–e are taken at the $\nu = -2/3$ FCI state. **c**, Anti-symmetrized $|R_{xy}|$ (blue) and symmetrized R_{xx} (red) at $|\mu_0 H| \approx 50$ mT as a function of D/ϵ_0 at $T = 100$ mK. **d**, Magnetic field dependence of R_{xx} and R_{xy} at selected temperatures with an electric field of $D/\epsilon_0 = 0$. R_{xy} remains nearly quantized at 1 K. **e**, ΔR_{xy}, the hysteretic component of R_{xy}, as a function of temperature and magnetic field.

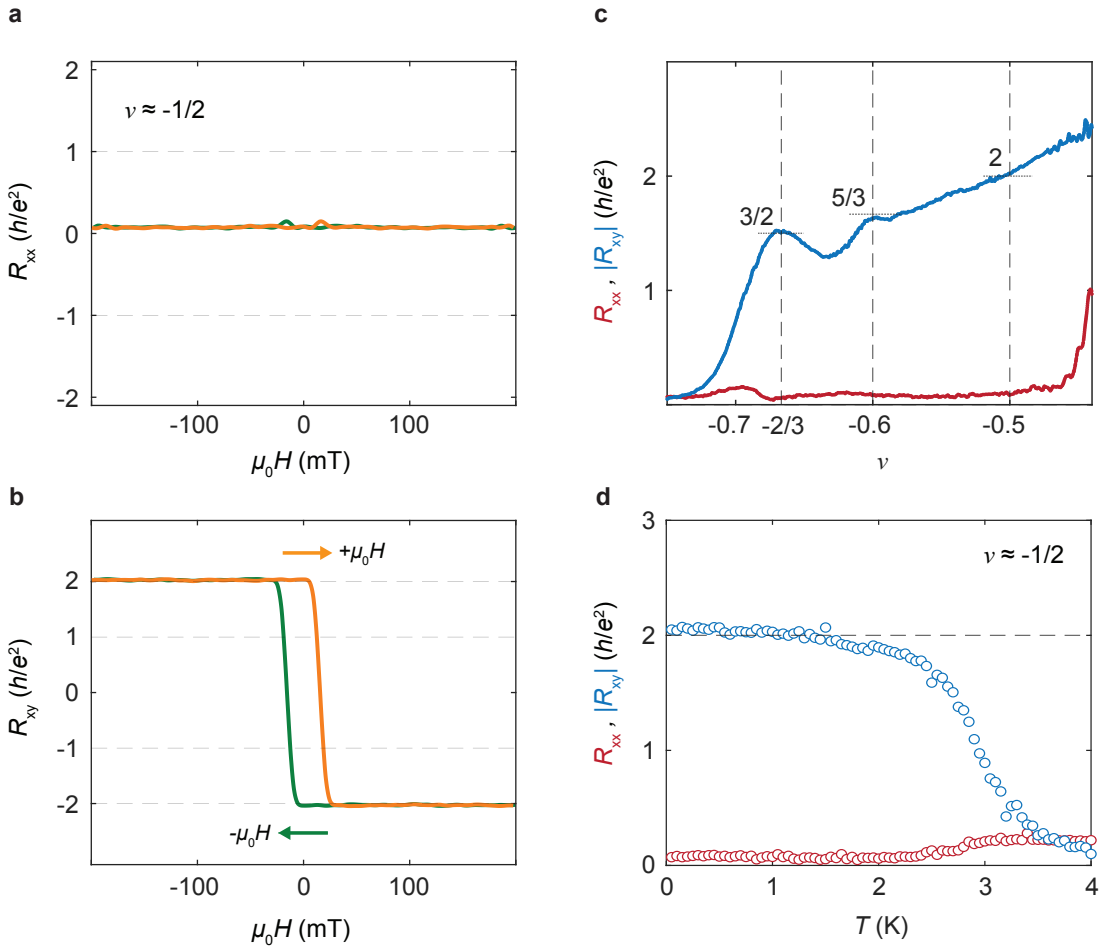

Figure 4.15: Anomalous Hall effect at half-filling. All data are taken at $D/\epsilon_0 = 0$. **a**,**b**, R_{xx} (**a**) and R_{xy} (**b**) versus magnetic field sweeps at $\nu \approx -1/2$ and $T = 500$ mK. R_{xy}, Symmetrized R_{xx} (red) and anti-symmetrized R_{xy} (blue) at ± 50 mT versus filling factor ν at $T = 100$ mK. $T = 500$ mK, Temperature dependence of symmetrized R_{xx} and anti-symmetrized R_{xy} at ± 50 mT for ν near $-1/2$. A phase transition is evident between 2 K and 4 K.

properties of these electronic phases at large D.

We then investigate their temperature dependence. Figure 4.14d shows the $\mu_0 H$ dependence of R_{xx} and R_{xy} for the –2/3 state at selected temperatures. Figure 4.14e is a plot of ΔRxy versus magnetic field and temperature. As T is increased above 1 K, R_{xy} starts to deviate from the quantized value at zero magnetic field, although it remains quantized under a small applied magnetic field (> 20 mT) up to about 2 K. Above this temperature, quantization is lost, until the hysteresis eventually vanishes for $T > 4$ K.

4.4.5 Anomalous Hall effect near half-filling

We now examine the behaviour near half-filling. Figure 4.15 a,b shows the $\mu_0 H$ dependence of R_{xx} and R_{xy} at $D/\epsilon_0 = 0$, at $T = 500$ mK and near $\nu \approx -1/2$. R_{xy} exhibits hysteresis with coercive field $\mu_0 H_C \approx 16$ mT and is about $\pm 2h/e^2$ at $\mu_0 H = 0$. Meanwhile, R_{xx} is approximately 2kΩ. The ν dependence of R_{xx} and R_{xy} at 100 mK, symmetrized and anti-symmetrized at $|\mu_0 H| = 50$ mT, is shown in Fig. 4.15c. We see that the quantized values close to $3h/2e^2$ and $5h/3e^2$ obtained at $\nu = -2/3$ and –3/5 are located at the top of the humps in R_{xy} versus ν. Near half-filling, R_{xy} becomes almost linear in ν and passes through a value close to $2h/e^2$ at $\nu = -1/2$. Across the entire range, R_{xx} remains at just a few kΩ. The linear dependence of R_{xy} versus ν suggests that the state is compressible, explaining why no gapped feature at $v = -1/2$ was seen in optical (trion-sensing) measurements as previously discussed. This behaviour of R_{xx} and R_{xy} bears a clear resemblance to that observed near half-filling of the lowest Landau level in a two-dimensional electron gas at high magnetic field, which has been found to be a composite Fermi liquid (CFL) state[48, 143, 144, 145, 146]. Recent numerical calculations have predicted that a zero-field CFL state is the ground state at $\nu = -1/2$ in twisted $MoTe_2$ (Ref. [147, 148]).

4.4.6 Thermal activation gap

Finally, we want to estimate the energy gap of the FCI. For the Chern insulator phase, it has an obvious thermally activated behavior that lies in the comfort zone of our measurement. Fig.4.16a shows a color map of R_{xx} versus T and $D/\epsilon_0 = 0$. We can fit Arrhenius equation

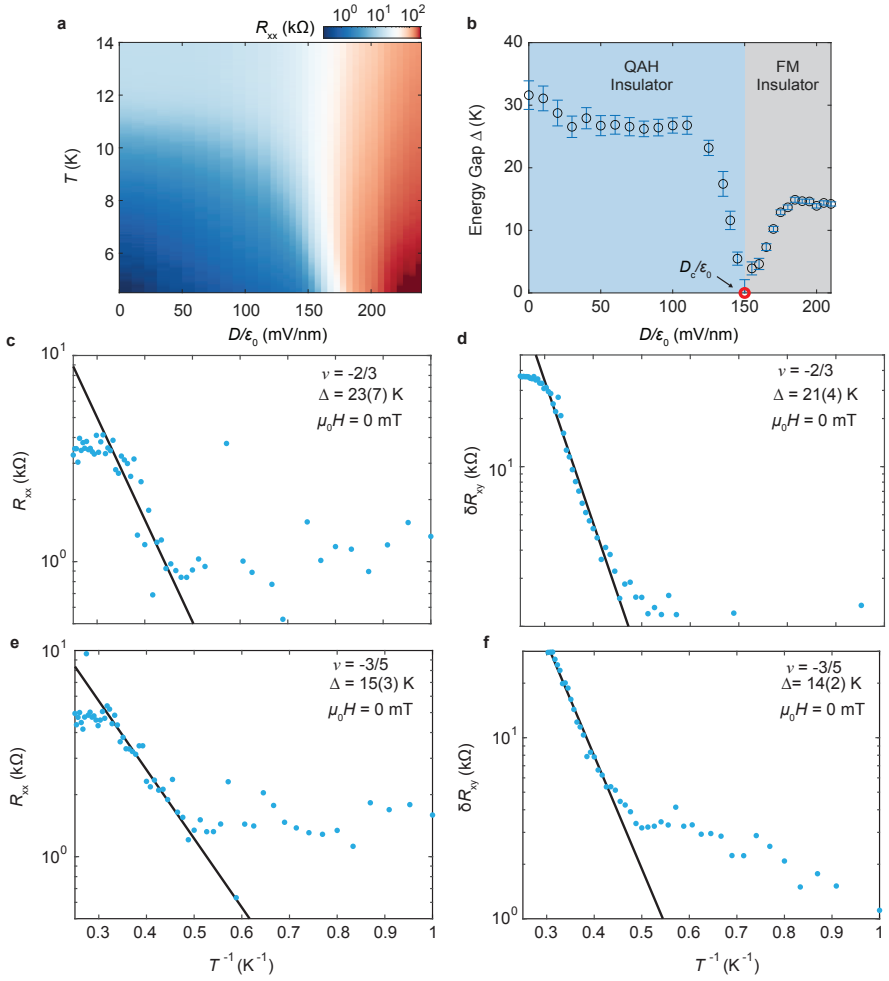

Figure 4.16: Thermal activation gap for integer and fractional Chern insulator. **a**, $R_x x$ as a function of D/ϵ_0 and T for $\nu = -1$. **b**, thermally activated gap for $\nu = -1$ as a function of D/ϵ_0. **c-d**, Arrhenius plot of R_{xx} and δR_{xy} for $\nu = -2/3$ and **e-f** for $\nu = -3/5$.

and obtain the activation gap Δ as a function of D/ϵ_0, using a topological gap $R_{xx} \sim \frac{\sigma_{xx}}{\sigma_{xy}^2} = R_0 e^{-\frac{\Delta}{2k_B T}}$. Fig.4.16b shows the activation gap across the topological phase transition. We can see that the gap is peaked at $D/\epsilon_0 \approx 0$ and slightly decreases as a small D/ϵ_0 is applied. The gap is greatly suppressed when it is closes to $D_C/\epsilon_0 \approx 150$ mV·nm^{-1} and nearly vanishes. After D_C/ϵ_0, a trivial gap appears so we change to the fitting $R_{xx} \sim \sigma_{xx}^{-1} = R_0 e^{\frac{\Delta}{2k_B T}}$.

For the FCI state, the Arrhenius equation from R_{xx} and $\delta R_{xy} \sim \frac{\sigma_{xx}^2}{\sigma_{xy}^4} \sim R_1 e^{-\frac{\Delta}{k_B T}}$ is fitted in Fig.4.16c-d, respectively. The energy gap of the –2/3 FCI state is estimated to be 23(7) K. A similar analysis for the thermally activated ($\delta R_{xy} \equiv 3h/2e^2$–$Rxy$) is consistent with this value. Using the same procedure, we find a smaller gap of $\Delta = 15(3)K$ for the –3/5 FQAH state as shown in Fig.4.16e-f. This is consistent with the conclusions of the optical measurements as shown before and exact diagonalization calculations[136].

In summary, we first discovered time reversal symmetric breaking of integer- and fractionally filled twisted $MoTe_2$ moiré superlattice around $\nu = -1$. Then, we reveal that these integer and fractional states are topological, being $C = -1$, $C = -2/3$ and $C = -3/5$ for $\nu = -1$, $\nu = -2/3$ and $\nu = -3/5$ states. They are zero-field FCI states. Finally, we observed fractional quantum anomalous Hall effect at $\nu = -2/3$ and $\nu = -3/5$ states with quantized Hall resistance at $3/2h/e^2$ and $5/3h/e^2$. Additionally, we observed an anomalous Hall effect with large Hall resistance $2h/e^2$ associated with $\nu \approx -1/2$. These experimental findings remarks the path to and discovery of the fractional quantum anomalous Hall effect.

BIBLIOGRAPHY

[1] Lev Davidovich Landau. "On the theory of phase transitions. I." In: *Zh. Eksp. Teor. Fiz.* 11 (1937), p. 19.

[2] V. L. Ginzburg and L. D. Landau. "On the Theory of superconductivity". In: *Zh. Eksp. Teor. Fiz.* 20 (1950). Ed. by D. ter Haar, pp. 1064–1082.

[3] Yoichiro Nambu. "Axial vector current conservation in weak interactions". In: *Physical Review Letters* 4.7 (1960), p. 380.

[4] Jeffrey Goldstone. "Field theories with superconductor solutions". In: *Il Nuovo Cimento (1955-1965)* 19 (1961), pp. 154–164.

[5] Michael E Fisher. "The renormalization group in the theory of critical behavior". In: *Reviews of Modern Physics* 46.4 (1974), p. 597.

[6] Kenneth G Wilson. "The renormalization group: Critical phenomena and the Kondo problem". In: *Reviews of Modern Physics* 47.4 (1975), p. 773.

[7] Pierre C Hohenberg and Alexei P Krekhov. "An introduction to the Ginzburg–Landau theory of phase transitions and nonequilibrium patterns". In: *Physics Reports* 572 (2015), pp. 1–42.

[8] Pierre Toledano and Jean-claude Toledano. *Landau Theory Of Phase Transitions, The: Application To Structural, Incommensurate, Magnetic And Liquid Crystal Systems*. Vol. 3. World Scientific Publishing Company, 1987.

[9] Lev Landau. *The theory of superfluidity of helium II*. CRC Press, 2018, pp. 185–204.

[10] K v Klitzing, Gerhard Dorda, and Michael Pepper. "New method for high-accuracy determination of the fine-structure constant based on quantized Hall resistance". In: *Physical Review Letters* 45.6 (1980), p. 494.

[11] David J Thouless et al. "Quantized Hall conductance in a two-dimensional periodic potential". In: *Physical Review Letters* 49.6 (1982), p. 405.

[12] Joseph E Avron, Ruedi Seiler, and Barry Simon. "Homotopy and quantization in condensed matter physics". In: *Physical Review Letters* 51.1 (1983), p. 51.

[13] JP Provost and G Vallee. "Riemannian structure on manifolds of quantum states". In: *Communications in Mathematical Physics* 76 (1980), pp. 289–301.

[14] Michael Victor Berry. "Quantal phase factors accompanying adiabatic changes". In: *Proceedings of the Royal Society of London. A. Mathematical and Physical Sciences* 392.1802 (1984), pp. 45–57.

[15] Walter Kohn. "Theory of the insulating state". In: *Physical review* 133.1A (1964), A171.

[16] Di Xiao, Ming-Che Chang, and Qian Niu. "Berry phase effects on electronic properties". In: *Reviews of Modern Physics* 82.3 (2010), p. 1959.

[17] Raffaele Resta. "The insulating state of matter: a geometrical theory". In: *The European Physical Journal B* 79 (2011), pp. 121–137.

[18] Raffaele Resta and Sandro Sorella. "Electron localization in the insulating state". In: *Physical Review Letters* 82.2 (1999), p. 370.

[19] Aleksi Julku et al. "Geometric origin of superfluidity in the Lieb-lattice flat band". In: *Physical Review Letters* 117.4 (2016), p. 045303.

[20] Jonah Herzog-Arbeitman et al. "Superfluid weight bounds from symmetry and quantum geometry in flat bands". In: *Physical Review Letters* 128.8 (2022), p. 087002.

[21] Michael Kolodrubetz et al. "Geometry and non-adiabatic response in quantum and classical systems". In: *Physics Reports* 697 (2017), pp. 1–87.

[22] Steven H Simon and Mark S Rudner. "Contrasting lattice geometry dependent versus independent quantities: Ramifications for Berry curvature, energy gaps, and dynamics". In: *Physical Review B* 102.16 (2020), p. 165148.

[23] David Beckman et al. "Measurability of Wilson loop operators". In: *Physical Review D* 65.6 (2002), p. 065022.

[24] F Duncan M Haldane. "Model for a quantum Hall effect without Landau levels: Condensed-matter realization of the" parity anomaly"". In: *Physical Review Letters* 61.18 (1988), p. 2015.

[25] Roman Jackiw. "Fractional charge and zero modes for planar systems in a magnetic field". In: *Physical Review D* 29.10 (1984), p. 2375.

[26] Holger Bech Nielsen and Masao Ninomiya. "Absence of neutrinos on a lattice:(I). Proof by homotopy theory". In: *Nuclear Physics B* 185.1 (1981), pp. 20–40.

[27] Holger Bech Nielsen and Masao Ninomiya. "Absence of neutrinos on a lattice:(II). Intuitive topological proof". In: *Nuclear Physics B* 193.1 (1981), pp. 173–194.

[28] Liang Fu, Charles L Kane, and Eugene J Mele. "Topological insulators in three dimensions". In: *Physical Review Letters* 98.10 (2007), p. 106803.

[29] M Zahid Hasan and Joel E Moore. "Three-dimensional topological insulators". In: *Annu. Rev. Condens. Matter Phys.* 2.1 (2011), pp. 55–78.

[30] B Andrei Bernevig, Taylor L Hughes, and Shou-Cheng Zhang. "Quantum spin Hall effect and topological phase transition in HgTe quantum wells". In: *Science* 314.5806 (2006), pp. 1757–1761.

[31] Chao-Xing Liu et al. "Model Hamiltonian for topological insulators". In: *Physical Review B* 82.4 (2010), p. 045122.

[32] Chao-Xing Liu, Shou-Cheng Zhang, and Xiao-Liang Qi. "The quantum anomalous Hall effect: theory and experiment". In: *Annual Review of Condensed Matter Physics* 7 (2016), pp. 301–321.

[33] Cui-Zu Chang, Chao-Xing Liu, and Allan H MacDonald. "Colloquium: Quantum anomalous hall effect". In: *Reviews of Modern Physics* 95.1 (2023), p. 011002.

[34] Daniel C Tsui, Horst L Stormer, and Arthur C Gossard. "Two-dimensional magnetotransport in the extreme quantum limit". In: *Physical Review Letters* 48.22 (1982), p. 1559.

[35] Robert B Laughlin. "Quantized Hall conductivity in two dimensions". In: *Physical Review B* 23.10 (1981), p. 5632.

[36] Robert B Laughlin. "Anomalous quantum Hall effect: an incompressible quantum fluid with fractionally charged excitations". In: *Physical Review Letters* 50.18 (1983), p. 1395.

[37] Frank Wilczek. "Quantum mechanics of fractional-spin particles". In: *Physical Review Letters* 49.14 (1982), p. 957.

[38] JM Leinaas and J Myrheim. "On the theory of identical particles". In: *Il nuovo cimento* 37 (1977), p. 132.

[39] Chen-Ning Yang and Robert L Mills. "Conservation of isotopic spin and isotopic gauge invariance". In: *Physical review* 96.1 (1954), p. 191.

[40] N Byers and CN Yang. "Theoretical considerations concerning quantized magnetic flux in superconducting cylinders". In: *Physical Review Letters* 7.2 (1961), p. 46.

[41] Bertrand I Halperin. "Statistics of quasiparticles and the hierarchy of fractional quantized Hall states". In: *Physical Review Letters* 52.18 (1984), p. 1583.

[42] F Duncan M Haldane. "Fractional quantization of the Hall effect: A hierarchy of incompressible quantum fluid states". In: *Physical Review Letters* 51.7 (1983), p. 605.

[43] S C_ Zhang, Th H Hansson, and S Kivelson. "Effective-field-theory model for the fractional quantum Hall effect". In: *Physical Review Letters* 62.1 (1989), p. 82.

[44] Shou Cheng Zhang. "The Chern–Simons–Landau–Ginzburg theory of the fractional quantum Hall effect". In: *International Journal of Modern Physics B* 6.01 (1992), pp. 25–58.

[45] Xiao-Gang Wen. "Topological orders and edge excitations in fractional quantum Hall states". In: *Advances in Physics* 44.5 (1995), pp. 405–473.

[46] Xiao-Gang Wen. "Theory of the edge states in fractional quantum Hall effects". In: *International journal of modern physics B* 6.10 (1992), pp. 1711–1762.

[47] Xiao-Gang Wen. "Colloquium: Zoo of quantum-topological phases of matter". In: *Rev. Mod. Phys.* 89 (4 Dec. 2017), p. 041004.

[48] Robert Willett et al. “Observation of an even-denominator quantum number in the fractional quantum Hall effect”. In: *Physical Review Letters* 59.15 (1987), p. 1776.

[49] J Falson et al. “Even-denominator fractional quantum Hall physics in ZnO”. In: *Nature Physics* 11.4 (2015), pp. 347–351.

[50] Dong-Keun Ki et al. “Observation of even denominator fractional quantum Hall effect in suspended bilayer graphene”. In: *Nano letters* 14.4 (2014), pp. 2135–2139.

[51] Alexander A Zibrov et al. “Tunable interacting composite fermion phases in a half-filled bilayer-graphene Landau level”. In: *Nature* 549.7672 (2017), pp. 360–364.

[52] JIA Li et al. “Even-denominator fractional quantum Hall states in bilayer graphene”. In: *Science* 358.6363 (2017), pp. 648–652.

[53] James Nakamura et al. “Direct observation of anyonic braiding statistics”. In: *Nature Physics* 16.9 (2020), pp. 931–936.

[54] Hugo Bartolomei et al. “Fractional statistics in anyon collisions”. In: *Science* 368.6487 (2020), pp. 173–177.

[55] Google Quantum AI and Collaborators. “Non-Abelian braiding of graph vertices in a superconducting processor”. In: *Nature* 618.7964 (2023), pp. 264–269.

[56] Mohsin Iqbal et al. “Non-Abelian topological order and anyons on a trapped-ion processor”. In: *Nature* 626.7999 (2024), pp. 505–511.

[57] Kai Sun et al. “Nearly flatbands with nontrivial topology”. In: *Physical Review Letters* 106.23 (2011), p. 236803.

[58] Evelyn Tang, Jia-Wei Mei, and Xiao-Gang Wen. “High-temperature fractional quantum Hall states”. In: *Physical Review Letters* 106.23 (2011), p. 236802.

[59] Titus Neupert et al. “Fractional quantum Hall states at zero magnetic field”. In: *Physical Review Letters* 106.23 (2011), p. 236804.

[60] DN Sheng et al. “Fractional quantum Hall effect in the absence of Landau levels”. In: *Nature Communications* 2.1 (2011), p. 389.

[61] Nicolas Regnault and B Andrei Bernevig. “Fractional chern insulator”. In: *Physical Review X* 1.2 (2011), p. 021014.

[62] Di Xiao et al. “Interface engineering of quantum Hall effects in digital transition metal oxide heterostructures”. In: *Nature Communications* 2.1 (2011), p. 596.

[63] Yong-Shi Wu. “General theory for quantum statistics in two dimensions”. In: *Physical Review Letters* 52.24 (1984), p. 2103.

[64] Kostya S Novoselov et al. “Electric field effect in atomically thin carbon films”. In: *Science* 306.5696 (2004), pp. 666–669.

[65] Kostya S Novoselov et al. “Two-dimensional gas of massless Dirac fermions in graphene”. In: *nature* 438.7065 (2005), pp. 197–200.

[66] Yuanbo Zhang et al. “Experimental observation of the quantum Hall effect and Berry’s phase in graphene”. In: *nature* 438.7065 (2005), pp. 201–204.

[67] Andrea F Young et al. “Spin and valley quantum Hall ferromagnetism in graphene”. In: *Nature Physics* 8.7 (2012), pp. 550–556.

[68] Yu Saito, Tsutomu Nojima, and Yoshihiro Iwasa. “Highly crystalline 2D superconductors”. In: *Nature Reviews Materials* 2.1 (2016), pp. 1–18.

[69] Bevin Huang et al. “Layer-dependent ferromagnetism in a van der Waals crystal down to the monolayer limit”. In: *Nature* 546.7657 (2017), pp. 270–273.

[70] Cheng Gong et al. “Discovery of intrinsic ferromagnetism in two-dimensional van der Waals crystals”. In: *Nature* 546.7657 (2017), pp. 265–269.

[71] Zaiyao Fei et al. “Edge conduction in monolayer WTe2”. In: *Nature Physics* 13.7 (2017), pp. 677–682.

[72] Xiaofeng Qian et al. “Quantum spin Hall effect in two-dimensional transition metal dichalcogenides”. In: *Science* 346.6215 (2014), pp. 1344–1347.

[73] and others. “Boron nitride substrates for high-quality graphene electronics”. In: *Nature Nanotechnology* 5.10 (2010), pp. 722–726.

[74] I Meric et al. “One-dimensional electrical contact to a two-dimensional material”. In: *Science* 342.6158 (2013), pp. 614–617.

[75] Matthew Yankowitz et al. “Emergence of superlattice Dirac points in graphene on hexagonal boron nitride”. In: *Nature physics* 8.5 (2012), pp. 382–386.

[76] and others. “Massive Dirac fermions and Hofstadter butterfly in a van der Waals heterostructure”. In: *Science* 340.6139 (2013), pp. 1427–1430.

[77] P Maher, Y Gao, et al. “Hofstadter’s butterfly and the fractal quantum Hall effect in moiré superlattices”. In: *Nature* 497.7451 (2013), pp. 598–602.

[78] Dmitry Ovchinnikov et al. “Intertwined topological and magnetic orders in atomically thin Chern insulator $MnBi_2Te_4$”. In: *Nano letters* 21.6 (2021), pp. 2544–2550.

[79] Jiaqi Cai et al. “Electric control of a canted-antiferromagnetic Chern insulator”. In: *Nature Communications* 13.1 (2022), pp. 1–7.

[80] Dmitry Ovchinnikov et al. “Topological current divider in a Chern insulator junction”. In: *Nature Communications* 13.1 (2022), pp. 1–6.

[81] Minhao He et al. “Symmetry breaking in twisted double bilayer graphene”. In: *Nature Physics* 17.1 (2021), pp. 26–30.

[82] Minhao He et al. “Symmetry-broken Chern insulators in twisted double bilayer graphene”. In: *Nano Letters* 23.23 (2023), pp. 11066–11072.

[83] Minhao He et al. “Dynamically tunable moiré exciton Rydberg states in a monolayer semiconductor on twisted bilayer graphene”. In: *Nature Materials* (2024), pp. 1–6.

[84] Eric Anderson et al. “Programming correlated magnetic states with gate-controlled moiré geometry”. In: *Science* 381.6655 (2023), pp. 325–339.

[85] Jiaqi Cai et al. “Signatures of fractional quantum anomalous Hall states in twisted MoTe2”. In: *Nature* 622 (2023), pp. 63–68.

[86] Heonjoon Park et al. “Observation of Fractionally Quantized Anomalous Hall Effect”. In: *Nature* 622 (2023), pp. 74–79.

[87] Cui-Zu Chang, Chao-Xing Liu, and Allan H. MacDonald. "Colloquium: Quantum anomalous Hall effect". In: *Rev. Mod. Phys.* 95 (1 Jan. 2023), p. 011002.

[88] Rui Yu et al. "Quantized anomalous Hall effect in magnetic topological insulators". In: *Science* 329.5987 (2010), pp. 61–64.

[89] Cui-Zu Chang et al. "Experimental observation of the quantum anomalous Hall effect in a magnetic topological insulator". In: *Science* 340.6129 (2013), pp. 167–170.

[90] Yabin Fan et al. "Magnetization switching through giant spin–orbit torque in a magnetically doped topological insulator heterostructure". In: *Nature materials* 13.7 (2014), pp. 699–704.

[91] Jue Jiang et al. "Concurrence of quantum anomalous Hall and topological Hall effects in magnetic topological insulator sandwich heterostructures". In: *Nature Materials* 19.7 (2020), pp. 732–737.

[92] Di Xiao et al. "Realization of the axion insulator state in quantum anomalous Hall sandwich heterostructures". In: *Physical Review Letters* 120.5 (2018), p. 056801.

[93] Jiaheng Li et al. "Intrinsic magnetic topological insulators in van der Waals layered $MnBi_2Te_4$-family materials". In: *Science Advances* 5.6 (2019), eaaw5685.

[94] Dongqin Zhang et al. "Topological axion states in the magnetic insulator $MnBi_2Te_4$ with the quantized magnetoelectric effect". In: *Physical Review Letters* 122.20 (2019), p. 206401.

[95] MM Otrokov et al. "Unique thickness-dependent properties of the van der Waals interlayer antiferromagnet $MnBi_2Te_4$ films". In: *Physical Review Letters* 122.10 (2019), p. 107202.

[96] Yujun Deng et al. "Quantum anomalous Hall effect in intrinsic magnetic topological insulator $MnBi_2Te_4$". In: *Science* 367.6480 (2020), pp. 895–900.

[97] Yan Gong et al. "Experimental realization of an intrinsic magnetic topological insulator". In: *Chinese Physics Letters* 36.7 (2019), p. 076801.

[98] Mikhail M Otrokov et al. "Prediction and observation of an antiferromagnetic topological insulator". In: *Nature* 576.7787 (2019), pp. 416–422.

[99] Zhenhua Qiao et al. “Quantum anomalous Hall effect in graphene proximity coupled to an antiferromagnetic insulator”. In: *Physical Review Letters* 112.11 (2014), p. 116404.

[100] Wei Han et al. “Graphene spintronics”. In: *Nature Nanotechnology* 9.10 (2014), pp. 794–807.

[101] Zhiyong Wang et al. “Proximity-induced ferromagnetism in graphene revealed by the anomalous Hall effect”. In: *Physical Review Letters* 114.1 (2015), p. 016603.

[102] Chun-Chih Tseng et al. “Gate-tunable proximity effects in graphene on layered magnetic insulators”. In: *Nano Letters* 22.21 (2022), pp. 8495–8501.

[103] Yaning Wang et al. “Quantum Hall phase in graphene engineered by interfacial charge coupling”. In: *Nature Nanotechnology* 17.12 (2022), pp. 1272–1279.

[104] Ling Lu, John D Joannopoulos, and Marin Soljačić. “Topological photonics”. In: *Nature Photonics* 8.11 (2014), pp. 821–829.

[105] Marc Serra-Garcia et al. “Observation of a phononic quadrupole topological insulator”. In: *Nature* 555.7696 (2018), pp. 342–345.

[106] M Serlin et al. “Intrinsic quantized anomalous Hall effect in a moiré heterostructure”. In: *Science* 367.6480 (2020), pp. 900–903.

[107] Tingxin Li et al. “Quantum anomalous Hall effect from intertwined moiré bands”. In: *Nature* 600.7890 (2021), pp. 641–646.

[108] Peizhi Mai et al. “1/4 is the new 1/2 when topology is intertwined with Mottness”. In: *Nature Communications* 14.1 (2023), p. 5999.

[109] Yongqian Wang et al. “Towards the Quantized Anomalous Hall effect in AlO_x-capped $MnBi_2Te_4$”. In: *arXiv preprint arXiv:2405.08677* (2024).

[110] Yaoxin Li et al. “Fabrication-induced even-odd discrepancy of magnetotransport in few-layer $MnBi_2Te_4$”. In: *Nature Communications* 15.1 (2024), p. 3399.

[111] J Eom et al. “Quantum Hall ferromagnetism in a two-dimensional electron system”. In: *Science* 289.5488 (2000), pp. 2320–2323.

[112] Andrew T Pierce et al. “Thermodynamics of free and bound magnons in graphene”. In: *Nature Physics* 18.1 (2022), pp. 37–41.

[113] Di S Wei et al. “Electrical generation and detection of spin waves in a quantum Hall ferromagnet”. In: *Science* 362.6411 (2018), pp. 229–233.

[114] Rafi Bistritzer and Allan H MacDonald. “Moiré bands in twisted double-layer graphene”. In: *Proceedings of the National Academy of Sciences* 108.30 (2011), pp. 12233–12237.

[115] Hongki Min and Allan H MacDonald. “Chiral decomposition in the electronic structure of graphene multilayers”. In: *Physical Review B* 77.15 (2008), p. 155416.

[116] P Streda. “Theory of quantised Hall conductivity in two dimensions”. In: *Journal of Physics C: Solid State Physics* 15.22 (1982), p. L717.

[117] P Streda and L Smrcka. “Thermodynamic derivation of the Hall current and the thermopower in quantising magnetic field”. In: *Journal of Physics C: Solid State Physics* 16.24 (1983), p. L895.

[118] ZZ Du et al. “Quantum theory of the nonlinear Hall effect”. In: *Nature Communications* 12.1 (2021), p. 5038.

[119] Inti Sodemann and Liang Fu. “Quantum nonlinear Hall effect induced by Berry curvature dipole in time-reversal invariant materials”. In: *Physical Review Letters* 115.21 (2015), p. 216806.

[120] Kin Fai Mak et al. “The valley Hall effect in MoS2 transistors”. In: *Science* 344.6191 (2014), pp. 1489–1492.

[121] Itzhack Dana and Kazuhiro Kubo. “Floquet systems with Hall effect: Topological properties and phase transitions”. In: *Physical Review B* 100.4 (2019), p. 045107.

[122] Ramesh G Mani et al. “Zero-resistance states induced by electromagnetic-wave excitation in GaAs/AlGaAs heterostructures”. In: *Nature* 420.6916 (2002), pp. 646–650.

[123] Yu Saito et al. “Isospin Pomeranchuk effect in twisted bilayer graphene”. In: *Nature* 592.7853 (2021), pp. 220–224.

[124] Asaf Rozen et al. “Entropic evidence for a Pomeranchuk effect in magic-angle graphene”. In: *Nature* 592.7853 (2021), pp. 214–219.

[125] A Kol and N Read. “Fractional quantum Hall effect in a periodic potential”. In: *Physical Review B* 48.12 (1993), p. 8890.

[126] Yang-Le Wu, B Andrei Bernevig, and Nicolas Regnault. “Zoology of fractional Chern insulators”. In: *Physical Review B* 85.7 (2012), p. 075116.

[127] Yonglong Xie et al. “Fractional Chern insulators in magic-angle twisted bilayer graphene”. In: *Nature* 600.7889 (2021), pp. 439–443.

[128] Eric M Spanton et al. “Observation of fractional Chern insulators in a van der Waals heterostructure”. In: *Science* 360.6384 (2018), pp. 62–66.

[129] Fengcheng Wu et al. “Topological insulators in twisted transition metal dichalcogenide homobilayers”. In: *Physical Review Letters* 122.8 (2019), p. 086402.

[130] Hongyi Yu, Mingxing Chen, and Wang Yao. “Giant magnetic field from moiré induced Berry phase in homobilayer semiconductors”. In: *National Science Review* 7.1 (2020), pp. 12–20.

[131] Evgeny Redekop et al. “Direct magnetic imaging of fractional Chern insulators in twisted MoTe _2 with a superconducting sensor”. In: *arXiv preprint arXiv:2405.10269* (2024).

[132] Peizhi Mai, Benjamin E Feldman, and Philip W Phillips. “Topological Mott insulator at quarter filling in the interacting Haldane model”. In: *Physical Review Research* 5.1 (2023), p. 013162.

[133] Heqiu Li et al. “Spontaneous fractional Chern insulators in transition metal dichalcogenide moiré superlattices”. In: *Physical Review Research* 3.3 (2021), p. L032070.

[134] Trithep Devakul et al. “Magic in twisted transition metal dichalcogenide bilayers”. In: *Nature Communications* 12.1 (2021), p. 6730.

[135] Xiao-Wei Zhang et al. “Polarization-driven band topology evolution in twisted MoTe2 and WSe2”. In: *Nature Communications* 15.1 (2024), p. 4223.

[136] Chong Wang et al. “Fractional Chern insulator in twisted bilayer MoTe 2”. In: *Physical Review Letters* 132.3 (2024), p. 036501.

[137] Lei Wang et al. “Correlated electronic phases in twisted bilayer transition metal dichalcogenides”. In: *Nature materials* 19.8 (2020), pp. 861–866.

[138] Hema CP Movva et al. “Tunable Γ-K valley populations in hole-doped trilayer WSe 2”. In: *Physical Review Letters* 120.10 (2018), p. 107703.

[139] Matthew R Rosenberger et al. “Nano-“squeegee” for the creation of clean 2D material interfaces”. In: *ACS applied materials & interfaces* 10.12 (2018), pp. 10379–10387.

[140] Jordan Pack et al. “Charge-transfer contact to a high-mobility monolayer semiconductor”. In: *arXiv preprint arXiv:2310.19782* (2023).

[141] Fan Xu et al. “Observation of integer and fractional quantum anomalous Hall effects in twisted bilayer MoTe 2”. In: *Physical Review X* 13.3 (2023), p. 031037.

[142] Zhurun Ji et al. “Local probe of bulk and edge states in a fractional Chern insulator”. In: *arXiv preprint arXiv:2404.07157* (2024).

[143] Jainendra K Jain. “Composite-fermion approach for the fractional quantum Hall effect”. In: *Physical Review Letters* 63.2 (1989), p. 199.

[144] Bertrand I Halperin, Patrick A Lee, and Nicholas Read. “Theory of the half-filled Landau level”. In: *Physical Review B* 47.12 (1993), p. 7312.

[145] RL Willett et al. “Experimental demonstration of a Fermi surface at one-half filling of the lowest Landau level”. In: *Physical Review Letters* 71.23 (1993), p. 3846.

[146] VJ Goldman, Bo Su, and JK Jain. “Detection of composite fermions by magnetic focusing”. In: *Physical Review Letters* 72.13 (1994), p. 2065.

[147] Junkai Dong et al. “Composite Fermi liquid at zero magnetic field in twisted MoTe 2”. In: *Physical Review Letters* 131.13 (2023), p. 136502.

[148] Hart Goldman et al. “Zero-field composite Fermi liquid in twisted semiconductor bilayers”. In: *Physical Review Letters* 131.13 (2023), p. 136501.

[149] Rachpon Kalra et al. “Vibration-induced electrical noise in a cryogen-free dilution refrigerator: Characterization, mitigation, and impact on qubit coherence”. In: *Review of Scientific Instruments* 87.7 (2016).

[150] L Neuhaus et al. “Pyrpl (python red pitaya lockbox)-an open-source software package for fpga-controlled quantum optics experiments”. In: *European Quantum Electronics Conference*. Optica Publishing Group. 2017, EAP8.

[151] AJ Bestwick et al. “Precise quantization of the anomalous Hall effect near zero magnetic field”. In: *Physical Review Letters* 114.18 (2015), p. 187201.

[152] Nodar Samkharadze, Ashwani Kumar, and Gábor A Csáthy. “A new type of carbon resistance thermometer with excellent thermal contact at millikelvin temperatures”. In: *Journal of Low Temperature Physics* 160 (2010), pp. 246–253.

[153] Christian P Scheller et al. “Silver-epoxy microwave filters and thermalizers for millikelvin experiments”. In: *Applied physics letters* 104.21 (2014).

[154] Pengjie Wang et al. “Piezo-driven sample rotation system with ultra-low electron temperature”. In: *Review of Scientific Instruments* 90.2 (2019).

[155] Matthew Pelliccione et al. “Design of a scanning gate microscope for mesoscopic electron systems in a cryogen-free dilution refrigerator”. In: *Review of Scientific Instruments* 84.3 (2013).

[156] Seong Woo Oh et al. “Cryogen-free scanning gate microscope for the characterization of $Si/Si_{0.7}Ge_{0.3}$ quantum devices at milli-Kelvin temperatures”. In: *AIP Advances* 11.12 (2021).

[157] Artem O Denisov et al. “Microwave-frequency scanning gate microscopy of a Si/SiGe double quantum dot”. In: *Nano Letters* 22.12 (2022), pp. 4807–4813.

Appendix A

EXPERIMENTAL METHODS

A.1 Sample fabrication

A.1.1 Mechanical exfoliation

We have performed Plasma cleaning in standard SiO_2 substrate to start with. Plasma cleaning will remove any water on the substrate which will make it easier to exfoliate on. This is especially important for the transition metal dichalcogenides and $MnBi_2Te_4$ because when the substrate is plasma cleaned before exfoliation, the yield of finding monolayers is enhanced.

Preparation of the tape is shown in Fig. A.1. First, a large crystal was fixed with a tape and another tape is picking up copies of the crystals. The copies form a regular array. We use the a tweezer to press the tape into the substrate. The amount of force used is subjective but usually gentle.

The success of mechanical exfoliation largely depends on crystal sizes, age of the tape, Oxygen plasma parameters, and how long the tape stays on the wafer. Many factors, however, also changes the yield slightly.

A.1.2 Anhydrous solvent

This section describes a standard operating procedure for preparing anhydrous solvent and properly using them in glovebox. This is very important for success for air sensitive mateirals.

Dichloromethane(DCM)/Isopropyl Alcohol(IPA): 1) Bake 1-3 days 1/2 liter clean blue capped bottle inside the oven at 160C. Plastic parts, e.g. ring and cap should not be baked. Good practice is also to keep plastic in vacuum (for example in big antechamber overnight) to get rid of possible water on top. 2) Load them from the oven inside the glovebox without any waiting, use thermal gloves not to burn yourself. Keep in antechamber while pumping

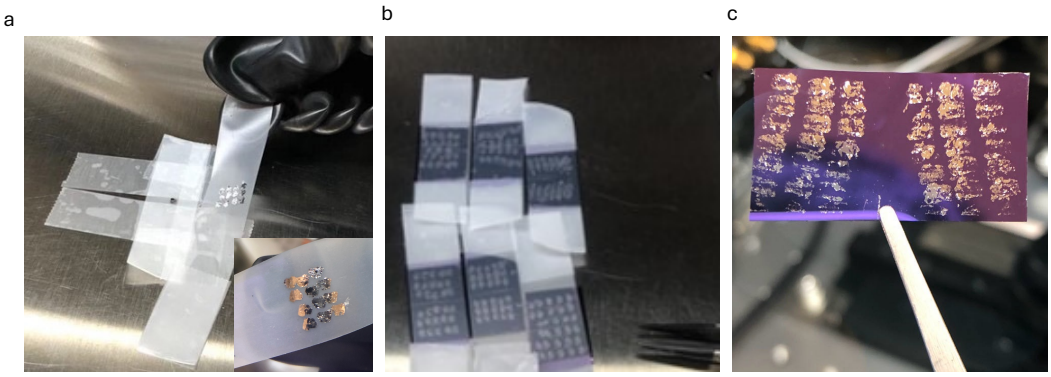

Figure A.1: Modified mechanical exfoliation of van der Waals materials. **a**, mechanical exfoliation using Scotch tape. **b**, demonstration of reproducing exfoliation. **c**, high yield from the described method.

for 10-15 min not to burn yourself while you load them inside 3) Put them on the hot plate at 180C for 1 day. 4) Remove from the hot plate, let them cool down. Notice, glass will get thermal shock and might crack if you cool it rapidly. If you fill with DCM or IPA while bottles are hot, solvents might start boiling. 5) Put 100 mL prepared sieves in each of the bottles. 6) Turn off circulation reactor and analyzer inside the glovebox. Take a clean dedicated syringe, take some corresponding anhydrous solvents from the bottles punching with the syringe needle through the rubber protection. Add 400 mL so that you have roughly 500mL total volume inside the bottle. 7) Wrap the bottle neck with Teflon tape. Put plastic ring, put blue cap. For extra protection, also wrap around with black electrical isolation tape after blue cap is put on top. 8) DCM can be safely used after 24 hours. IPA requires 48 hours or more to get good. From my experience, devices start to be really good after a week of exposure of solvents to molecular sieves. 9) Test with CrI_3 and other magnets. In general, several minute exposure is enough (we do lift off with this amount of time).

For liftoff with those: 1) Anneal 100mL white cap beaker for 1 day at 160C (more time is better). Add to this several glass pipettes, they will be required for actual lift off. 2) Load immediately inside the glovebox 3) Bake for 1 day at 180-200C 4) Cool down 5) Turn off circulation reactor and analyzer inside Glovebox. Add DCM using dedicated filter syringe to your beaker. Without filtering, small particles from molecular sieves will adsorb on device surface. 6) Put your device inside DCM. While it is sitting there (5 min) filter some IPA into small plastic petri dish. Plastic should be pumped overnight inside the antechamber to be good to go. 7) Use glass pipette #1 to flow DCM on top of your device surface until it looks visually clean 8) Carefully start taking out your chip from DCM. At the same time continuously flow IPA from pipette #2 on the surface not to let it dry. Put wet sample into small petri dish with IPA. Quickly (try to do it in less than 1 minute) inspect it under the uscope to see lift off quality. If it looks ok (if it doesn't look ok, see below) quickly take it out from IPA and dry. 9) If liftoff didn't work, e.g. you see some shunted electrodes, put it back to DCM, take DCM beaker out, sonicate for 10-30 seconds (depends on how fragile the device is), come back, repeat step 8. It is important to keep device in DCM, not in IPA, IPA is more harmful for MBT as soon as it has more water.

PMMA preparation: 1) Bake 100mL white or black capped beaker for 1 day inside the oven at 160C. Do not bake plastic parts, pump them inside the antechamber overnight. In parallel, bake resist bottle (available in chem store) and glass pipette in similar conditions. 2) Load them from the oven inside the glovebox without any waiting, use thermal gloves not to burn yourself. Keep in antechamber while pumping for 10-15 min not to burn yourself while you load them inside 3) Put them on the hot plate at 180C for 1 day. 4) Remove from the hot plate, let them cool down. Notice, glass will get thermal shock and might crack if you cool it rapidly. 5) Anneal at 80C for several hours white magnet for stirring (available in chem store) or appropriate size (should freely rotate inside your bottle, shouldn't be too small) 6) While they are cooling glassware, start loading extra hot plate (yellow one) with possibility to use magnetic stirring and scales inside the MEM-C glovebox through the right large antechamber 7) PMMA and anhydrous solvent (anisole) should be already there. For best results, both PMMA powder (350k) and anisole should be both new 8) Zero the annealed beaker on the scales. Add 3g of pmma powder. Add 47g of anisole using dedicated syringe. Punch the rubber protection on the bottle with syringe needle. 9) Add magnet for stirring, add Teflon tape on the beaker neck, put the cap 10) Put mixture at yellow hot plate at T = 65C and reasonable stirring speed. Pay attention to the mixture so it doesn't start boiling. Let it stir at this temperature for 1-2 hours. Check that all pmma powder has been dissolved after that time. 11) Add 10-20 mL of this solution to the resist bottle. Seal the cap with Teflon tape, move to CEI glovebox as quick as possible. 12) Do dose test for 4000 RPM spin coating.

MIBK/IPA 1/3 vol mixture: 1) Bake 100mL white or black capped beaker for 1 day inside the oven at 160C. Do not bake plastic parts, pump them inside the antechamber overnight. Bake 100mL blue capped bottle in similar conditions. 2) Load them from the oven inside the glovebox without any waiting, use thermal gloves not to burn yourself. Keep in antechamber while pumping for 10-15 min not to burn yourself while you load them inside 3) Put them on the hot plate at 180C for 1 day. 4) Remove from the hot plate, let them cool down. Notice, glass will get thermal shock and might crack if you cool it rapidly. 5) Bring some MIBK inside the glovebox (50mL). I didn't find it in anhydrous form of it. Put it into annealed 100mL blue capped bottle, add a little bit of molecular sieves, wait 1 day. 6)

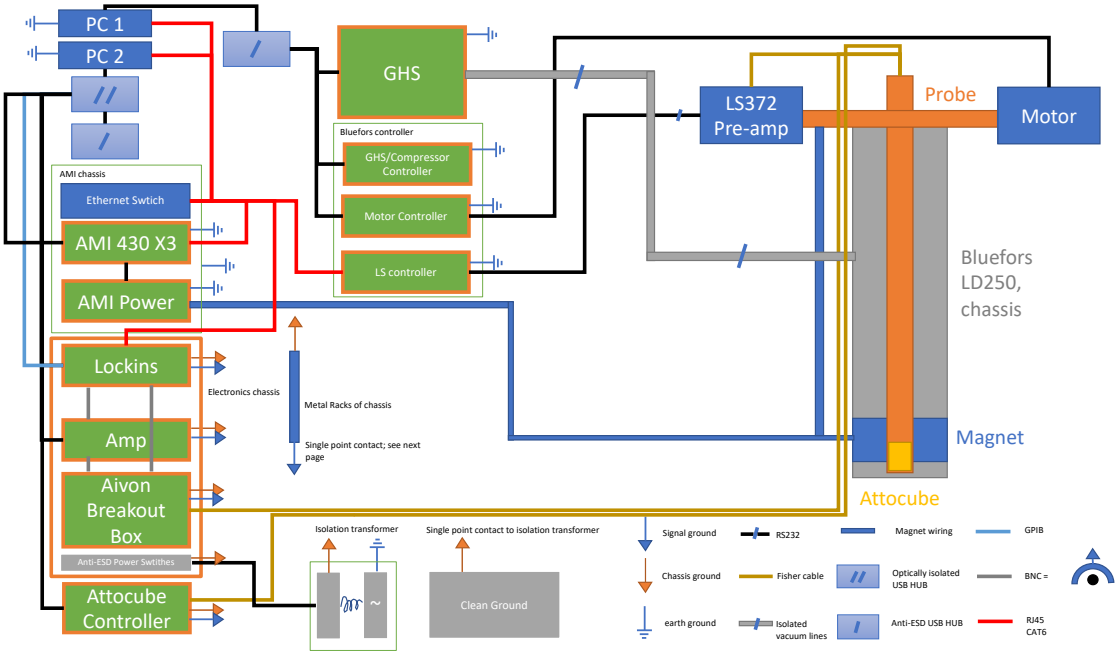

Figure A.2: Illustration of the grounding design of a dilution refrigerator I

Filter with dedicated filter syringe 10 mL of MIBK into the white capped beaker (prepared in advance, see 1)-4)), filter 30mL of IPA (see section about DCM/IPA preparation) using dedicated filter syringe.

A.2 Low-temperature electronic transport

A.2.1 Grounding loop

We provide the following grounding loop diagram for two dilution refrigerators (DRs) that I set up. The key is to keep signal ground and chasis ground (single bonded to each other) clear, and bond to earth ground in a **single point**, which is shown in Fig.A.3.

A special note is that commercial transformer isolator such as Trip Lite one has bonded Neutral to Earth (N2E) from both end. This needs to be modified and a true electrical isolation must be obtained from both ends. To test and develop the grounding design in field, I homemade an internet-connected oscilloscope with Red Pitaya. I track how noise couples to each other. The noise after solving the grounding loop is comparable to that in

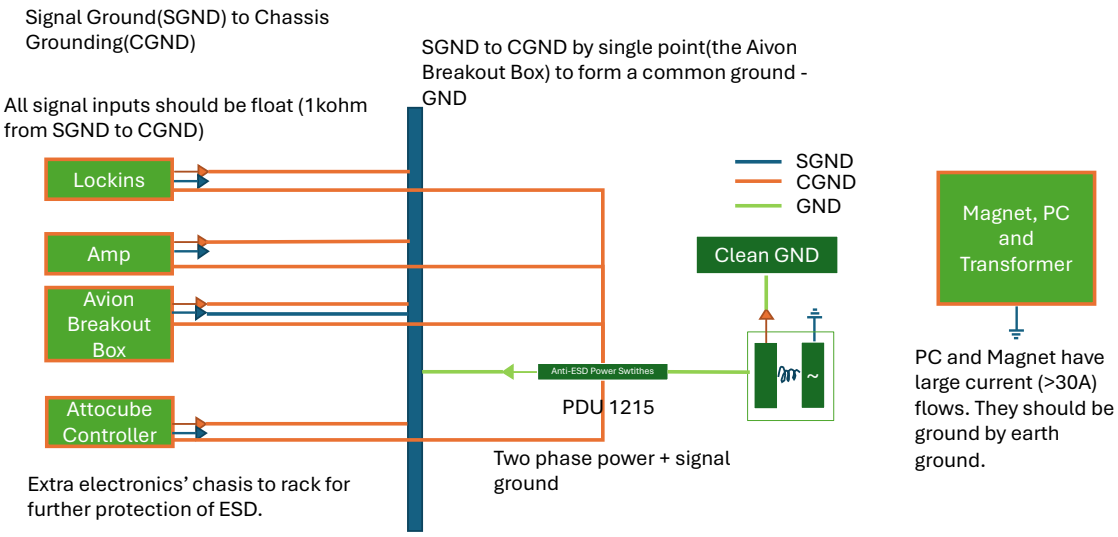

Figure A.3: Illustration of the grounding design of a dilution refrigerator II

Ref. [149].

The effect of adding a grounding loop and removing all grounding loop can be seen using an oscilloscope. We used an open source FPGA based data acquisition tool, Red Pitaya [150]. After removing all grounding loop, two terminals can be shorted inside the fridge and a DL1211 amplifier is used to amplify the nois in a broad band. Fig.A.4 shows a characteristic noise spectrum for the system after removing all grounding loop. A $10 - 20nV/\sqrt{Hz}$ noise density at interested frequency except line frequency can be achieved reliably. The broadband integrated current noise is less than 0.2 nA. The noise is mainly generated from the long wires that connect the dilution fridge and electronics that capacitvely couples to each other, but not from the low temperature end. Further reducing the line needs designing of amplifier that closer to the sample.

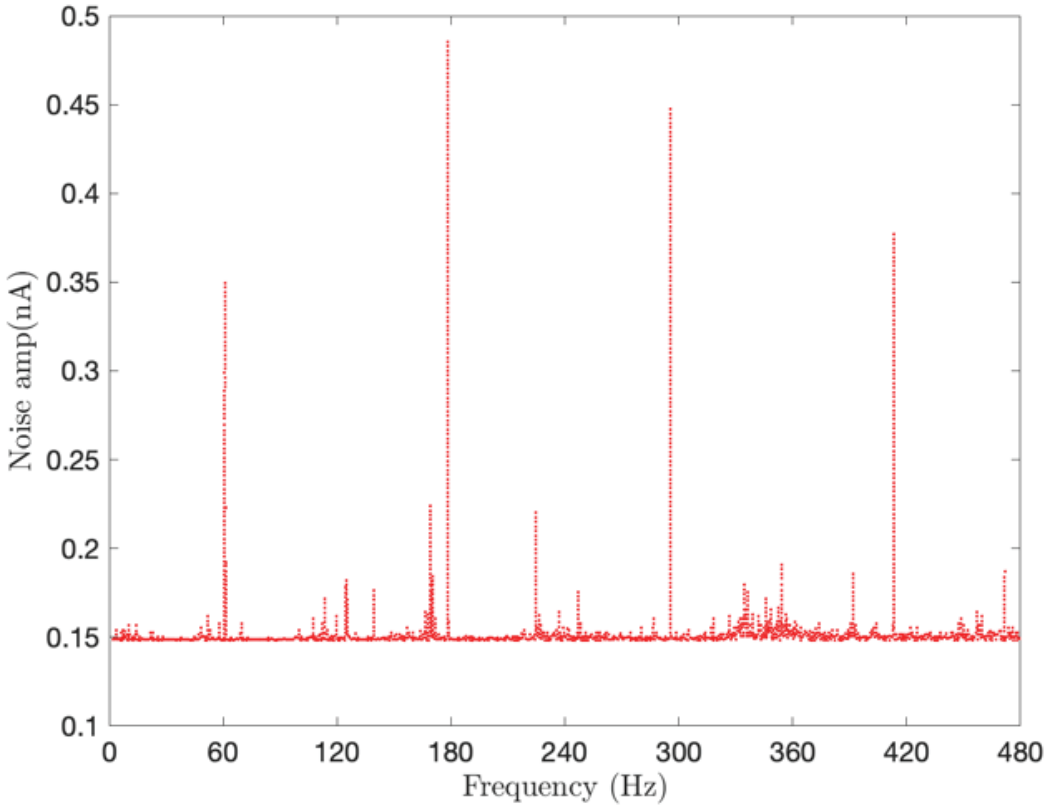

Figure A.4: Spectrum of typical noise level of the system. A heavily filtered small dc bias that creates is used for better electronic trigger.

A.3 Transport measurement and temperautre sensor

Transport measurements were conducted in a dilution refrigerator (Bluefors) with low-temperature electronic filters and an out-of-plane 13T superconductor magnet coil. Four-terminal longitudinal resistance R_{xx} and Hall resistance R_{yx} were measured using standard lock-in technique with an a.c excitation of 0.5–10nA at 1.777-13.777 Hz. The a.c. excitation was provided by the SR830 in series with a 100MΩ resistor, flowed through the device, and was pre-amplified by DL1211 at $1V/10^{-6}$ A sensitivity. Signals were pre-amplified by differential-ended mode of SR560 with a 1000 times amplification. All preamplifiers were read out by SR830. A similar amplifier chain provided approximately ±3% uncertainty in the previous study[151]. We estimated our uncertainty was of the same order. Magneto-transport data involved positive and negative magnetic fields was anti-symmetrized/symmetrized by a standard method to avoid geometric mixing of R_{xx} and R_{xy}. As this mixing did not affect the topological transport signal, we presented raw data for fixed magnetic field study.

Figure A.5: Image of the carbon composition sensor as the resistance temperature sensor.

Multiple sensors on the top-loading probe and on the thermal plates are used for improving thermal relaxing and more reliable temperature measurement. A Cernox sensor fabricated by Lakeshore with thermalization plate and filters made by Bluefors is calibrated and used as the primary resistance temperature sensor for calibrating other. We made extra carbon composition resistor sensor fabricated as described in Ref.[152] (OF470JE, commerically available known as Little Demon of the Ohmite Manufacturing Co). The resistor is about 50Ω in room temperature. First the package was removed and the two terminal resistance increased to 300Ω. Two Induim ball with appropriate sensor was glued as the soldering contact with some amount of silver epoxy and then melt to form contact. Then Kapton foil and Stycast are used to isolated it, as shown in Fig. A.5 The sensor is then attached to a PPMS

probe that was daily used, for thermal cycling from 300K to 2K at least twenty times in a period of a month. Standard calibration was done by using the RuO_x sensor as the reference and measuring the resistance as function of RuO_x sensor resistance.

With multiple sensors installed in our probe, we can perform reliable temperature dependent measurement continuously from 300 mK to $4K$ when the thermal lag is not significant. For example, the current on a resistive heater mounted near the sample was gradually ramped up, with the temperature read out using a Cernox sensor close to the sample. This carbon composition sensor mounted on the chip carrier shows that the temperature difference between the sensor and the sample stage temperature does not exceed 50 mK.

Sample electronic temperature is measured by temperature dependent features of the device itself. For example, a monolayer graphene sample can show fractional quantum Hall effect in a moderate magnetic around 8 T and low temperature. We found that $\nu = -11/7$ yields the best thermal activation below 1 K and use this to verify if the filter design can get rid of high frequency spurious effect due to relative poor contact of two dimensional materials.

A.3.1 Filter

For the fridge that can host bulk wiring, a mature solution for DC transport filtering is the combination of thermo-coax cables, silver epoxy filters and RC filters, see Ref.[153, 154]. The top-loading fridge where the experimental space is very limited. I have used a combination of LC filters, RC and copper powder filter instead. The LC filters consist three stages with 80MHz (LFCN-80+, Mini circuits), 1.45GHz (LFCN-1450+) and 5GHz (LFCN-5000+) for each channel, repeated > 3 times. Then, a combination of 500 Ω, 2.2 nF RC filter, meander filter immersed in copper power, and another 1200 Ω, 1 nF RC filter is used, as shown in Fig.A.6. Sometimes a homemade meander filter immersed in silver epoxy is used, but proved to be redundant. The filter stages are thermalized using a gold-plated copper cage. In future, an upgrade can be made if flexible distributed filters at higher temperature stage, such as circuits fabricated in polymide, can be reliably obtained commercially. This will be

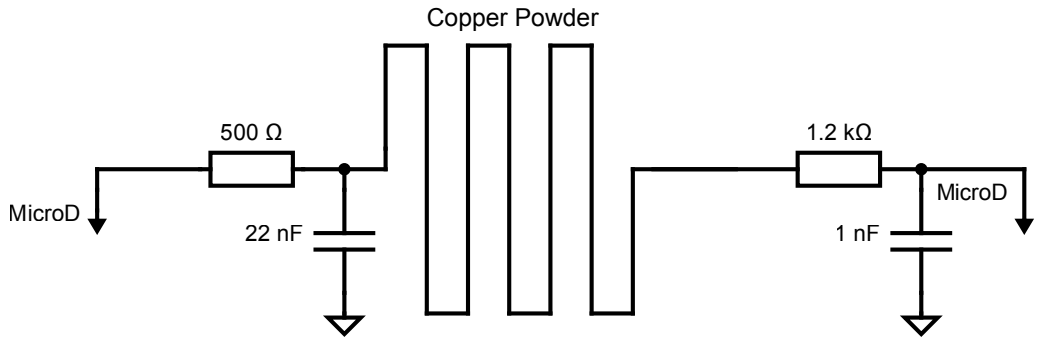

Figure A.6: Illustration of the filter design

an option to replace the need of thermo-coax cables, when limited by experimental space.

A.3.2 Nanopositioner and mechanical isolator

We have low ohmic wiring specially for nanopositioner, in particular stick-slip type stages, as shown in FigA.7. Extra radio frequency(RF) and breakout for low temperature amplifier are also provided for other users.

We have tested a solution for optical spectroscopy in dilution temperature and low sample electronic temperature. The system is now capable of photocurrent and reflection spectroscopy. The challenges have been thermalizing the piezo stage for positioning the sample, integrating filters, mechanical noise cancellation and a limited experimental space for top-loading system. Sample thermalization is improved by a homemade thermalization stage on top of the piezo stack as shown in Fig.A.8 (a)-(c). A rod that can host a brass screw is directly connected to a thermalization stage made with gold plated copper and thermalized by copper braid. On the chip carrier, this brass screw will be touching the grounding pad of the chip carrier. We note that the PCB (FR4) and ceramic can hardly be thermalized. This is not an issue for base temperature measurement after a long waiting time. For temperature dependent measurement, the design need to be largely revised.

Mechanical isolation stage [155, 156, 157] is a revised version for top-loading system

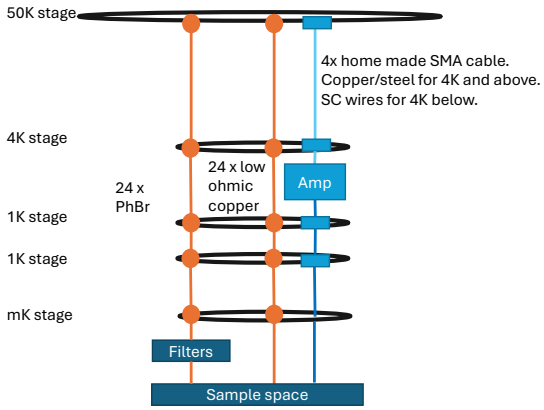

Figure A.7: Illustration of the experimental wiring for a dilution refrigerator

designed by Prof. Arthur Barnard. We tested this stage for mounting functionality and fully compatible with top-loading system.

A.4 Optical spectroscopy

A.4.1 Photoluminence

All measurements were performed in a closed-loop magneto-optical exchange gas cryostat (attoDRY 2100) with an attocube xyz piezo stage, a 9-T out-of-plane superconducting magnet and a base temperature of 1.6 K. For PL measurements, a 632.8-nm helium–neon laser was focused on the sample by a high-numerical-aperture non-magnetic objective to minimize the magnetic-field-induced drift. Differential reflectance measurements were performed under the same conditions using a tungsten–halogen lamp. The reflected signal was dispersed with a diffraction grating (Princeton Instruments, 600 grooves per mm at 1-μm blaze) and detected by an liquid nitrogen-cooled infrared charge-coupled device (Princeton Instruments PyLoN-IR 1.7). For PL measurements, a long-pass filter was inserted before the entrance to the spectrometer to remove reflected laser excitation. The PL showed polarization dependence, measured by inserted an analyzer (a quarter wave plate and linear polarizer), linked to the ferromagnetism of the system.

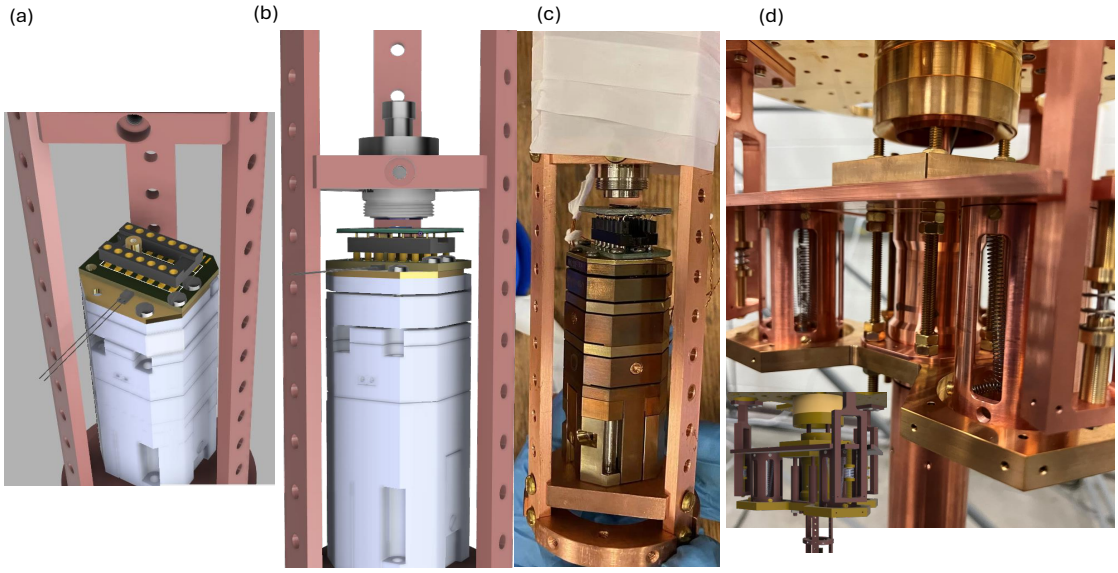

Figure A.8: Illustration of a mechanical isolation stage and sample thermolization design. (a), an illustration of the DIP socket chip carrier design. A rod that can host a brass screw is directly connected to a thermalization stage made with gold plated copper and thermalized by copper braid. A temperature sensor is attached to the thermalization state. (b), design with optical objective and chip carrier. (c), image of the designed sample stage, attocube nanopositioner and scanner stacks made by CuBe alloy for better thermalization. (d), degisn and image of a mechanical isolation stage for mechanical noise cancellation.

A.4.2 Reflected magnetic circular dichorism

RMCD was performed by filtering a broadband supercontinuum source (NKT SuperK EXTREME EXW-12) by dual-passing through a monochromator, achieving a narrow excitation bandwidth in resonance with the trion feature. The out-of-plane magnetization of the sample induces an MCD signal. RMCD measurements were performed in an attoDRY cryostat with attocube xyz piezo stage, the base temperature of 1.6K and 9 T superconducting magnet. The magnetic field was applied perpendicular to the sample plane. Linearly polarized 632.8 nm He–Ne laser with 200 nW power was focused through an aspheric lens or objective to form $\tilde{2}$ µm beam spot on the sample surface. The out-of-plane magnetization of the sample induced magnetic circular dichroism (MCD) ΔR, the amplitude difference between the reflected right- and left-circularly polarized light. To obtain the RMCD $\Delta R/R$ signal, two lock-in amplifiers SR830 were used to analyze the output signals from a photomultiplier tube with the chopping frequency $p = 1.377$ kHz and photoelastic modulator frequency $f = 50$ kHz. The ratio between p-component signal I_1 and f-component signal I_2 is proportional to the RMCD signal: $\Delta R/R = I_2/(J_1(\pi/2)I_1)$ where J_1 is the first-order Bessel function.

VITA

Jiaqi grew up in Wuhan, Hubei, China and developed interests in maths and theoretical computer science during his high school. He received B. S. in Applied Physics from Huazhong University of Science and Technology in the same city in 2019, where he was a theorist in condensed matter and quantum optics.

He moved to University of Washington, Seattle to pursue a Ph.D. in Physics, where he shifted his interest to condensed matter experiments and very luckily began working with Prof. Xiaodong Xu. In Xu lab, Jiaqi learned how to solve experimental challenges.